

People's Democratic Republic Of Algeria
Ministry of Higher Education and
Scientific Research
University of Kasdi Merbah, Ouargla
Faculty of Applied Sciences
Department of Process Engineering



**Thesis submitted in fulfillment of the requirements for the degree of Doctorate
(LMD) in Process Engineering**

Speciality: Énergétique et Procédés

Submitted by:

KHENBLOUCHE Abdelkader

**PREPARATION, CHARACTERIZATION AND
APPLICATION OF COMPOSITES BASED ON
GRAPHENE AND FIBERS.**

Publicly submitted on : **07/07/2019**

In front of the jury :

Pr. SEKHRI Lakhdar	Professor	University of Ouargla	President
Dr. BELADEL Brahim	M.C.A	University of Djelfa	Examiner
Pr. BOUGUETTAIA Hamza	Professor	University of Ouargla	Examiner
Pr. BECHKI Djamel	Professor	University of Ouargla	Supervisor

Academic year: 2018/2019

Abstract

Among all natural fibers, cellulose has attracted much attention owing to its fascinating properties and sustainability. On the other hand, graphene is gathering quickly growing interest as the rising star of nanotechnology with its exceptional characteristics. Therefore, cellulose/conductive polymers/graphene composites offer a unique combination of environmental benefits and enhanced performance for energy storage applications, including supercapacitors, which are the most promising energy storage devices.

In the present thesis, conductive polyaniline-coated cellulose fibers hybridized with rGO in different ratios were fabricated by adopting a series of simple operations including; the extraction of both cellulose microfibrils (CMF) (with a yield = 52.1% and a crystallinity = 77.8%) from *Retama Raetam* plant, and cellulose nanowhiskers (CNW) (with a crystallinity = 82.04%) from cotton, the synthesis of rGO by a sonication-assisted oxidation of graphite, then the in situ polymerization of aniline monomer in the presence of CMF or CNW, followed by the hybridization of the as-prepared composites with different ratios of rGO. The as-prepared composites were then characterized and applied as supercapacitor electrodes and their supercapacitive performance was investigated using different electrochemical methods. Thus, appreciable specific capacitance values up to 465.32 F g^{-1} were achieved.

Keywords : Cellulose microfibrils, nanowhiskers, graphene, polyaniline, composites, supercapacitors.

المخلص

من بين جميع الألياف الطبيعية، جذب السليلوز قدرًا كبيرًا من الاهتمام نتيجة لخصائصه المتميزة واستدامته. من ناحية أخرى، يشير الجرافين اهتمامًا متزايدًا باعتباره النجم الصاعد في تكنولوجيا النانو بخصائصه الاستثنائية. لذلك، توفر المتراكبات المؤلفة من السليلوز/البوليمرات الموصلة/الجرافين مزيجًا فريدًا من الفوائد البيئية والأداء المحسن لتطبيقات تخزين الطاقة، بما فيها المكثفات الفائقة، والتي تعد أهم الأجهزة الواعدة لتخزين الطاقة.

في هذه الأطروحة، تم تحضير متراكبات ناقلة من ألياف السليلوز/بولينيلين وتهجينها بنسب مختلفة من أكسيد الجرافين المُختزل (rGO)، وذلك بالاعتماد على سلسلة من العمليات تتضمن استخلاص كل من ألياف السليلوز الميكروية (بمردود = 52.1٪ وبلورة = 77.8٪) من نبات Retama Raetam، ولييفات السليلوز النانوية (CNW) (بلورة = 82.04٪) من القطن، تحضير rGO من خلال أكسدة الجرافيت مع استخدام الرج بالأمواج فوق الصوتية، بلمرة مونومر الأنيلين (in situ) في وجود CMF أو CNW، ثم تهجين المتراكبات المعدة بنسب مختلفة من rGO. تم تشخيص خصائص المتراكبات المحضرة وتطبيقها كأقطاب للمكثفات الفائقة وتم فحص أدائها وسعتها التخزينية باستخدام طرق كهروكيميائية مختلفة. حيث تم الحصول على قيم سعة محسنة بشكل ملحوظ تصل إلى 465.32 فاراد/غ.

الكلمات المفتاحية : ألياف السليلوز الميكروية، لييفات نانوية، الجرافين، البولي أنيلين، المتراكبات، المكثفات الفائقة.

Résumé

Parmi les fibres naturelles, la cellulose a beaucoup attiré l'attention en raison de ses propriétés fascinantes et de sa durabilité. D'autre part, le graphène suscite de plus en plus d'intérêt en tant qu'étoile montante de la nanotechnologie avec ses caractéristiques exceptionnelles. Par conséquent, les composites de cellulose/polymères conducteurs/graphène offrent une combinaison unique d'avantages environnementaux et de performances améliorées pour les applications de stockage d'énergie, y compris les supercondensateurs, qui sont les dispositifs de stockage d'énergie les plus prometteurs.

Dans la présente thèse, des fibres conductrices de cellulose enrobées par de polyaniline et hybridées avec de l'oxyde de graphène réduit (rGO) en différentes proportions ont été fabriquées par l'adoption d'une série d'opérations simples comprenant ; l'extraction de microfibrilles de cellulose (CMF) (avec un rendement = 52,1% et une cristallinité = 77,8%) à partir de la plante *Retama Raetam*, et de nanowhiskers de cellulose (CNW) (avec une cristallinité = 82,04%) à partir du coton, puis la synthèse de rGO par l'oxydation du graphite assistée par ultra-sonication, et ensuite la polymérisation in situ du monomère aniline en présence de CMF ou de CNW, puis l'hybridation des composites préparés avec différentes proportions de rGO. Ces composites ont ensuite été caractérisés et appliqués en tant qu'électrodes de supercondensateur et leur performance supercapacitive a été étudiée à l'aide de différentes méthodes électrochimiques. Ainsi, des capacités spécifiques appréciables allant jusqu'à 465,32 F g⁻¹ ont été atteintes.

Mots-clés: microfibrilles de cellulose, nanowhiskers, graphène, polyaniline, composites, supercondensateurs.

Acknowledgments

I wish to thank first and foremost, **ALLAH** the all-powerful for endowing me -during all my years of education- with health, courage and patience to come to this day. Without **ALLAH**'s blessings, this achievement would not have been possible.

I would like to express my great appreciation to my thesis advisor **Pr. Djamel BECHKI**, for his precise guidance and encouragement. I will never hesitate to express the spirit and inspiration that he gave me during my work. It will be my great pleasure to tell that I am extremely fortunate to have worked under his supervision.

My acknowledgments are to be sent to the board of examiners: **Pr. Lakhdar SAKHRI**, **Dr. Brahim BELADEL**, and **Pr. Hamza BOUGUETAIA**, who have accepted to examine this work.

Also, I would really thank **Dr. Messaoud GOUAMID**, for his insight, support, and sharing of knowledge. My sincere thanks also go to **Dr. Soufiane BENHAMIDA**, **Pr. Ladjel SEGNI**, **Dr. Mohamed HADJADJ**, **Pr. Radhouane CHTOUROU**, **Dr. Khaled CHARRADI**, and **Dr. Haythem GAMMOUDI** for their co-operation during my project work.

Although, it is difficult to put an appropriate word, still I have a great effort to express my deepest gratitude from the beneath of my heart to my beloved **mother** and **father** and all the members in my family who inspired and encouraged me constantly to succeed my work.

My special thanks are extended to **the staff of the Department of Chemical Engineering** and **the Faculty of Applied Sciences** at Ouargla University, for their all kinds of help.

Last but not least, I would like to thank all my **friends** and **colleagues** who contributed in terms of discussion and moral support.



Table of Contents

TABLE OF CONTENTS	I
LIST OF FIGURES	IV
LIST OF TABLES	VI
LIST OF ABBREVIATIONS	VII
1. GENERAL INTRODUCTION	1
1.1. Introduction	1
1.2. Thesis Outline	3
1.3. References	3
2. CELLULOSE FIBERS: AN OVERVIEW	5
2.1. Introduction	5
2.2. Lignocellulosic biomass	5
2.3. Cellulose, an insight	7
2.4. Molecular Structure of cellulose	7
2.5. Cellulose crystalline polymorphs	9
2.6. Sources and extraction of cellulose fibers	9
2.7. Nanocellulose	11
2.7.1. Types and properties	11
2.7.2. Preparation methods	12
2.7.3. Nancellulose Applications	13
2.8. References	15
3. GRAPHENE AND ITS PROPERTIES	18
3.1. Introduction	18
3.2. Graphene structure	19
3.3. Graphene properties	20
3.3.1. Electronic properties	20
3.3.2. Mechanical properties	21
3.3.3. Thermal properties	22
3.3.4. Optical properties	23
3.4. Graphene synthesis	23
3.4.1. Mechanical exfoliation	24
3.4.2. Liquid-phase exfoliation	25
3.4.3. Electrochemical exfoliation	26
3.4.4. Graphene via reduction of graphene oxide	27
3.4.5. Chemical vapor deposition	28
3.4.6. Other methods	30
3.5. Reference	30
4. SUPERCAPACITORS AND THEIR ELECTRODE MATERIALS	35
4.1. Background	35
4.2. Brief history and basic principles	36

4.3. Supercapacitors classification	37
4.3.1. Electrochemical double-layer capacitors (EDLCs)	37
4.3.1.1. Electrode materials for EDLCs	39
4.3.2. Pseudocapacitors.....	39
4.3.2.1. Common pseudocapacitive materials.....	40
4.3.3. Hybrid supercapacitors	44
4.4. Electrochemical characterization techniques	45
4.5. Supercapacitors applications	47
4.6. References	48
5. EXTRACTION AND CHARACTERIZATION OF CELLULOSE MICROFIBERS FROM RETAMA RAETAM STEMS	52
5.1. Introduction	52
5.2. Materials and methods	53
5.2.1. Materials	53
5.2.2. Preparation of samples	54
5.2.3. Microfibers extraction	54
5.2.4. Fourier transform infrared spectroscopy.....	55
5.2.5. X-ray Diffraction (XRD) Analysis.....	55
5.2.6. Morphological structure	55
5.2.7. Thermogravimetric analysis (TGA).....	55
5.3. Results and discussion	56
5.3.1. Extraction method and cellulose yield.....	56
5.3.2. FT-IR spectroscopic analysis	56
5.3.3. X-ray Diffraction measurements.....	58
5.3.4. Morphological properties of chemically purified cellulose microfibers.....	60
5.3.5. Thermal stability.....	62
5.4. Conclusion	63
5.5. References	64
6. PREPARATION AND CHARACTERIZATION OF CELLULOSE NANOWHISKERS FROM PURE COTTON	68
6.1. Introduction	68
6.2. Materials and methods	69
6.2.1. Materials	69
6.2.2. Preparation of cellulose nanowhiskers (CNW)	69
6.2.3. Characterization methods.....	69
6.3. Results and discussion	69
6.3.1. Diffraction analysis	69
6.3.2. Morphological analysis	70
6.4. Conclusion	71
6.5. References	71
7. SYNTHESIS OF REDUCED GRAPHENE OXIDE (RGO)	73
7.1. Introduction	73
7.2. Materials and methods	74
7.2.1. Materials	74
7.2.2. Synthesis of reduced graphene oxide (rGO).....	74

7.2.3. Characterization methods.....	75
7.3. Results and discussion.....	75
7.3.1. Raman spectroscopy.....	75
7.3.2. X-ray diffraction analysis.....	76
7.4. Conclusion.....	77
7.5. References.....	77
8. SYNTHESIS AND CHARACTERIZATION OF CELLULOSE/POLYANILINE/RGO COMPOSITES	79
.....	79
8.1. Introduction.....	79
8.2. Materials and methods.....	80
8.2.1. Materials.....	80
8.2.2. Preparation of CMF/PANI and CNW/PANI composites.....	80
8.2.3. CMF/PANI/rGO composites preparation.....	80
8.2.4. CNW/PANI/rGO composites preparation.....	81
8.2.5. Characterization methods.....	81
8.3. Results and discussion.....	81
8.3.1. Synthesis process.....	81
8.3.2. Structural and Morphological analysis.....	82
8.4. Conclusion.....	86
8.5. References.....	87
9. PREPARATION OF SUPERCAPACITOR ELECTRODES AND THEIR ELECTROCHEMICAL CHARACTERIZATION.....	89
9.1. Introduction.....	89
9.2. Experimental details.....	90
9.2.1. Materials.....	90
9.2.2. Preparation of supercapacitor electrodes.....	90
9.2.3. Electrochemical characterization techniques.....	90
9.3. Results and discussion.....	91
9.3.1. Cyclic voltammetry.....	91
9.3.2. Galvanostatic charge/discharge.....	93
9.3.3. Electrochemical impedance spectroscopy (EIS).....	98
9.4. Conclusion.....	99
9.5. References.....	100
10. CONCLUSIONS AND PROSPECTS.....	103

List of Figures

Figure 2.1: Structure of lignocellulosic biomass containing cellulose, hemicellulose, and lignin.	7
Figure 2.2: The structure and the inter- and intra-chain hydrogen bonding in cellulose I.	8
Figure 2.3: Transformation of cellulose into its different polymorphs.	9
Figure 2.4: TEM micrographs of CNCs (a), CNFs (b), and SEM micrograph of BC (c).	11
Figure 3.1: Graphene is the basic building block for all graphitic materials [7].	19
Figure 3.2: (a) Graphene hexagonal structure [15], (b) Schematic of the σ bonds and the p orbitals [16].	19
Figure 3.3: Electronic band structure of graphene: (a) the conduction band touches valence band at the K and K' points, and (b) linear band dispersion relation near the Dirac points showing gapless features, and (c) electronic properties of graphene depend on the layer number.	21
Figure 3.4: Schematic of the optothermal Raman measurement technique [41].	22
Figure 3.5: (a) An assembled graphene/PET touch panel [31], (b) white light transmittance through mono and bilayer graphene [44].	23
Figure 3.6: Schematic representation of micro-mechanical cleavage of graphite.	25
Figure 3.7: Schematic of an electrochemical cell used for graphite exfoliation (a) [59], and proposed mechanisms for graphite exfoliation in LiClO_4/PC electrolyte (b) [60], and in $\text{NaOH}/\text{H}_2\text{O}_2/\text{H}_2\text{O}$ electrolyte (c) ...	26
Figure 3.8: Schematic illustration of the preparation of reduced graphene oxide (rGO) from graphite	28
Figure 3.9: Diagram of the graphene growth mechanism by CVD method, transport and reaction processes ...	29
Figure 3.10: (a) Illustration of several techniques for CNTs unzipping [83], and (b) typical steps of graphene epitaxial growth on an SiC substrate.	30
Figure 4.1: Schematic of the Leyden jar [7].	36
Figure 4.2: The electrical double layer models, (a) Helmholtz model, (b) Gouy-Chapman model, and (c) Stern model. [21]	38
Figure 4.3: Charging schematic of EDL capacitor [22].	39
Figure 4.4: Schematic of charge storage via pseudocapacitance [27].	40
Figure 4.5: Chemical structures of main conducting polymers (CPs) used in supercapacitors.	42
Figure 4.6: Reversible doping/dedoping of polyaniline.	44
Figure 4.7: Application fields of supercapacitors.	47
Figure 4.8: Schematic illustration of wayside regenerative braking energy storage system (ESS) for subway trains. [57]	48
Figure 5.1: Photograph of the Retama raetam plant.	53
Figure 5.2: FT-IR spectra of (a) untreated sample, (b) alkali treated sample, and (c) bleached cellulose microfibrils.	57
Figure 5.3: XRD diffractogram of extracted R. raetam cellulose microfibrils.	59
Figure 5.4: SEM images of extracted R. raetam cellulose microfibrils.	60
Figure 5.5: TGA (a) and DTG (b) curves of the untreated sample and the bleached cellulose microfibrils.	62

Figure 6.1: XRD data of pure cotton and hydrolyzed cellulose nanowhiskers (CNW).....	70
Figure 6.2: SEM micrographs of single cotton fiber (a) and hydrolyzed CNW (b, c).....	71
Figure 7.1: Raman spectra of pristine graphite and reduced graphene oxide (rGO).	76
Figure 7.2: XRD of pristine graphite and reduced graphene oxide (rGO).	76
Figure 8.1: Representative schematic of the composites preparation process.	82
Figure 8.2: XRD data of (a) CMF, CMF/PANI and CMFPGs composites, (b) CNW, CNW/PANI and CNWPGs composites.	83
Figure 8.3: Raman spectra of (a) CMF, CMF/PANI and CMFPGs composites, (b) CNW, CNW/PANI and CNWPGs composites.	84
Figure 8.4: SEM micrographs of CMF (a), CMF/PANI (b), CMFPG10 (c), CNW (d), CNW/PANI (e), and CNWPG10 (f).....	86
Figure 9.1: (a) CV curves of bare Pt, CMF/PANI, CMFPG10, and CMFPG20 at 50 mV s ⁻¹ . (b) Normalized integrated CV areas (%). (c) CV curves of CMFPG10 at different scan rates.....	92
Figure 9.2: (a) CV curves of bare GC, CNW/PANI, CNWPG10, CNWPG20 and CNWPG40 at 100 mV s ⁻¹ . (b) Normalized integrated CV areas (%). (c) CV curves of CNWPG10 at different scan rates.	93
Figure 9.3: (a) GCD profiles of CMF/PANI, CMFPG10, and CMFPG20 at a current density of 1 A g ⁻¹ . (b) GCD profiles of CMFPG10 at different current densities. (c) Cs of CMFPG10 as a function of various current densities.	94
Figure 9.4: (a) GCD profiles of CNW/PANI, CNWPG10, CNWPG20 and CNWPG40 at a current density of 1 A g ⁻¹ . (b) GCD profiles of CNWPG10 at different current densities. (c) Cs of CNWPG10 as a function of various current densities.	95
Figure 9.5: The impedance data of CNW/PANI and CNWPGs composite electrodes.....	99

List of Tables

Table 2.1: Chemical composition of some typical cellulose-containing natural sources [15].....	10
Table 5.1: The main observed IR bands and their assignments.	58
Table 5.2: Comparison of the crystallinity indices of cellulose microfibers from various sources.	59
Table 5.3: Comparison of the diameters of cellulose microfibers extracted from various sources by different extraction methods.	61
Table 5.4: DTG _{max} and char yields of cellulose microfibers from different sources.....	63
Table 7.1: Intensity ratios I_D/I_G for pristine graphite and rGO.....	76
Table 8.1: The main observed Raman bands and their assignments.....	85
Table 9.1: Comparison of the performance of PANI-based graphene composites in supercapacitor electrodes at a current density of 1 A g^{-1}	97

List of Abbreviations

APS	Ammonium persulphate
BC	Bacterial cellulose
CE	Counter electrode
CFG	Carboxyl-functionalized graphene
CMF	Cellulose microfibers
CMFPGs	Cellulose microfibers/polyaniline/reduced graphene oxide composites
CMOS	Complementary metal-oxide-semiconductor
CNC	Cellulose nanocrystals
CNF	Cellulose nanofibers
CNTs	Carbon nanotubes
CNW	Cellulose nanowhiskers
CNWPGs	Cellulose nanowhiskers/polyaniline/reduced graphene oxide composites
CPE	Constant phase element
CPs	Conducting polymers
CrI	Crystallinity index
C_{sp}	Specific capacitance
CV	Cyclic voltammetry
CVD	Chemical vapor deposition
DMF	N,N-dimethylformamide
DMSO	Dimethyl sulfoxide
DNA	Deoxyribonucleic acid
DP	Degree of polymerization
EB	Emeraldine base
EDLCs	Electrochemical double-layer capacitors
EIS	Electrochemical impedance spectroscopy
ES	Emeraldine salt
ESR	Equivalent series resistance
ESS	Energy storage system

FETs	Field effect transistors
FT-IR	Fourier transform infrared spectroscopy
GC	Glassy carbon
GCD	Galvanostatic charging/discharging
GICs	Graphite intercalated compounds
GNRs	Graphene nanoribbons
GNS	Graphene nanosheets
GO	Graphene oxide
HEVs	Hybrid-electric vehicles
HOPG	Highly oriented pyrolytic graphite
HSCs	Hybrid supercapacitors
IHP	Inner Helmholtz plane
LB	Leucoemeraldine base
LCDs	Liquid crystal displays
LEDs	Light emitting diodes
LPE	Liquid-phase exfoliation
LS	Leucoemeraldine salt
MFC	Microfibrillated cellulose
NCC	Nanocrystalline cellulose
NEC	Nippon electric company
NEMs	Nanoelectromechanical systems
NFC	Nanofibrillated cellulose
NHE	Normal hydrogen electrode
NMP	N-methylpyrrolidone
OCP	Open-circuit potential
OFGs	Oxygen-containing functional groups
OHP	Outer Helmholtz plane
OLEDs	Organic light emitting diodes
PANI	Polyaniline
PANI-HS	Polyaniline hollow spheres
PC	Propylene carbonate
PC	Propylene carbonate

PE	Polyethylene
PECVD	Plasma-enhanced chemical vapor deposition
PEDOT	Poly-[3,4-ethylenedioxythiophene]
PET	Polyethylene terephthalate
PNB	Pernigraniline base
PNS	Pernigraniline salt
PP	Polypropylene
PPy	Polypyrrole
PTh	Polythiophene
PVA	Polyvinyl alcohol
RE	Reference electrode
rGO	Reduced graphene oxide
SCE	Saturated calomel electrode
SEI	Solid/electrolyte interface
SEM	Scanning electron microscopy
SHE	Standard hydrogen electrode
SOHIO	Standard oil company of Ohio
SSA	Specific surface area
TCFs	Transparent conductive films
TGA	Thermogravimetric analysis
UDP)	Uridine diphosphate
UPS	Uninterruptible power supply
WE	Working electrode
XRD	X-ray Diffraction

1

General Introduction

1.1. Introduction

Over the last few decades, The use of natural fibers instead of synthetic fibers as reinforcement materials for polymer composites has gained considerable attention because of their unique characteristics, such as renewability, biodegradability, processing flexibility, low density, high specific strength and low-cost [1, 2]. In addition, natural fibers have applications in various fields such as bioenergy industries, automobiles, paper manufacturing and textile, owing to their properties and broad availability [1, 3]. As a result, nowadays, the subject of many researchers worldwide focuses on the need to find alternative fiber sources [4]. Among all natural fibers, cellulose has attracted much interest as it is the most abundant renewable resource in nature and the degradation of cellulosic biomass is an important part of the biosphere's carbon cycle [5]. It is a polydispersed linear polymer with a fibrillar structure composed of poly- β (1 \rightarrow 4)-D-glucose units with a syndiotactic configuration [6, 7], found in the cell walls as a network of nanofibrils embedded in a non-cellulosic matrix [8]. Cellulose is, currently, the most promising feedstock for various industrial and domestic life applications owing to its interesting properties [9]. These interesting properties include its robust mechanical strength, its high functionality as well as the porous canals feature in natural cellulose fibers, which work as an additional ion diffusion route for the charge/discharge processes, has opened the gate for cellulose to be applied in energy storage cells fabrication [10].

Graphene, the rising star of nanotechnology, is a flat monolayer of carbon atoms packed into a two-dimensional (2D) hexagonal lattice, firstly isolated in 2004 and came into the limelight of material science in 2010 through the announcement of Noble Prize in Physics [11]. Graphene is a hot topic in the circles of science and engineering, being an alternative to replace many traditional materials for different applications and gathering quickly growing research interest because of its tremendous mechanical performance, distinctive optical properties, and exceptional electrical and thermal conductivities [12, 13]. Various methods are being developed for producing graphene based on both bottom-up and top-down approaches, some of these methods are currently scalable and others still on the laboratory scale [12, 14].

Furthermore, conductive polymers/cellulose composites are recently becoming a trend in composites research because of their good properties as compared to their conventional counterparts that had already found applications in, for instance, adsorbents, sensors, batteries, and supercapacitors. Moreover, Polyaniline (PANI) is one of the most used conductive polymers, especially for supercapacitor electrodes, due to its controllable electrical conductivity and doping/dedoping chemistry as well as facile synthesis and low-cost [15]. In this context, chemical polymerization of PANi on cellulose fibers has recently been used for synthesizing conductive composite films and similar materials; for instance, Stejskal et al. [16] reported the in-situ coating of cellulose paper with PANI as a flame-retardant to prevent the complete destruction of the paper during burning. Via in-situ polymerization of aniline on bacterial cellulose (BC), Mashkour et al. [17] fabricated BC/PANI nanobiocomposites used as bio-anodes in microbial fuel cells. Avelar Dutra and co-authors [18] used PANI-deposited cellulose fiber composite as an adsorbent for the removal of *meloxicam* from aqueous media. Wang et al. [19] reported the synthesis of BC nanofiber-supported PANI nanocomposites with flake-shaped morphology as supercapacitor electrodes. Moreover, Xu and co-workers [20] constructed highly cycling stable electrode materials for supercapacitors via in situ synthesis of PANI on cellulose matrix by using phytic acid as a “bridge”.

In addition, graphene has recently been used to enhance the capacitive performance of PANI, based on the fact that PANI is a well enough electron donor and graphene is a good electron acceptor. The electrical conductivity, the charge transfer properties, and the specific capacitance of graphene/PANi composites are significantly improved compared to pure PANI [21, 22].

In the present thesis, ternary cellulose/PANI/rGO composites are fabricated by adopting a series of steps based on a combined methodology of in-situ chemical polymerization and solution mixing. The advantages of PANI, the outstanding properties of rGO, and worthy physical properties of cellulose along with its biocompatibility and biodegradability, will be fully combined to promote supercapacitor electrodes performance.

1.2. Thesis Outline

The present work is part of the development research of composite materials based on graphene and fibers for the storage of electrical energy.

The thesis is divided into two parts; (I) a descriptive theoretical part: to give a theoretical underpinning to our research object through a comprehensive review on the materials involved in this research, namely, cellulose fibers, graphene, as well as PANI, in addition to a thorough overview on supercapacitors, their types, electrode materials, characterization methods, and their applications. (II) an experimental practical part: which involves the extraction of cellulose microfibrils (CMF) and cellulose nanowhiskers (CNW) from selected sources, the synthesis of reduced graphene oxide (rGO) by a sonication-assisted oxidation of graphite, and then the preparation of cellulose/PANI/rGO composites. These composite materials reinforced with cellulose fibers are then characterized and applied as supercapacitor electrodes and their electrochemical behavior is studied by different electrochemical methods. The results obtained are discussed, commented and compared with available data from the literature and conclusions are drawn.

1.3. References

- [1]. P. Baskaran, M. Kathiresan, P. SenthamaraiKannan, S. Saravanakumar. Characterization of new natural cellulosic fiber from the bark of dichrostachys cinerea. *Journal of Natural Fibers*. **2018**. 15(1), 62-8.
- [2]. L. Mohammed, M. N. M. Ansari, G. Pua, M. Jawaid, *et al.* A Review on Natural Fiber Reinforced Polymer Composite and Its Applications. *International Journal of Polymer Science*. **2015**. 2015, 15.
- [3]. R. M. Sheltami, I. Abdullah, I. Ahmad, A. Dufresne, *et al.* Extraction of cellulose nanocrystals from mengkuang leaves (*Pandanus tectorius*). *Carbohydrate Polymers*. **2012**. 88(2), 772-9.
- [4]. N. F. M. Zain, S. M. Yusop, I. Ahmad. Preparation and characterization of cellulose and nanocellulose from pomelo (*Citrus grandis*) albedo. *Journal of Nutrition and Food Sciences*. **2014**. 5(1), 334.
- [5]. L. Zhao, Q. Pang, J. Xie, J. Pei, *et al.* Enzymatic properties of *Thermoanaerobacterium thermosaccharolyticum* β -glucosidase fused to *Clostridium cellulovorans* cellulose binding domain and its application in hydrolysis of microcrystalline cellulose. *BMC Biotechnology*. **2013**. 13(1), 101.

- [6]. S. Naduparambath, T. Jinitha, V. Shaniba, M. Sreejith, *et al.* Isolation and characterisation of cellulose nanocrystals from sago seed shells. *Carbohydrate Polymers*. **2018**. 180, 13-20.
- [7]. M. Vestena, I. P. Gross, C. M. O. Muller, A. T. N. Pires. Isolation of whiskers from natural sources and their dispersed in a non-aqueous medium. *Polímeros*. **2016**. 26, 327-35.
- [8]. R. J. Bernardo, M. F. Gírio, M. R. Łukasik. The Effect of the Chemical Character of Ionic Liquids on Biomass Pre-Treatment and Posterior Enzymatic Hydrolysis. *Molecules*. **2019**. 24(4).
- [9]. M. M. Khattab, N. A. Abdel-Hady, Y. Dahman. 21 - Cellulose nanocomposites: Opportunities, challenges, and applications, in *Cellulose-Reinforced Nanofibre Composites*, ed. by M. Jawaid, S. Boufi, A. K. H.P.S, Woodhead Publishing. **2017**. 483-516.
- [10]. Z. Gui, H. Zhu, E. Gillette, X. Han, *et al.* Natural Cellulose Fiber as Substrate for Supercapacitor. *ACS Nano*. **2013**. 7(7), 6037-46.
- [11]. R. Geetha Bai, N. Ninan, K. Muthoosamy, S. Manickam. Graphene: A versatile platform for nanotheranostics and tissue engineering. *Progress in Materials Science*. **2018**. 91, 24-69.
- [12]. N. A. A. Ghany, S. A. Elsherif, H. T. Handal. Revolution of Graphene for different applications: State-of-the-art. *Surfaces and Interfaces*. **2017**. 9, 93-106.
- [13]. M. Chakraborty, M. S. J. Hashmi. Wonder material graphene: properties, synthesis and practical applications. *Advances in Materials and Processing Technologies*. **2018**. 4(4), 573-602.
- [14]. Y. Seekaew, O. Arayawut, K. Timsorn, C. Wongchoosuk. Chapter Nine - Synthesis, Characterization, and Applications of Graphene and Derivatives, in *Carbon-Based Nanofillers and Their Rubber Nanocomposites*, ed. by S. Yaragalla, R. Mishra, S. Thomas, N. Kalarikkal, H. J. Maria, Elsevier. **2019**. 259-83.
- [15]. Q. Meng, K. Cai, Y. Chen, L. Chen. Research progress on conducting polymer based supercapacitor electrode materials. *Nano Energy*. **2017**. 36, 268-85.
- [16]. J. Stejskal, M. Trchová, I. Sapurina. Flame-retardant effect of polyaniline coating deposited on cellulose fibers. *Journal of Applied Polymer Science*. **2005**. 98(6), 2347-54.
- [17]. M. Mashkour, M. Rahimnejad, M. Mashkour. Bacterial cellulose-polyaniline nano-biocomposite: A porous media hydrogel bioanode enhancing the performance of microbial fuel cell. *Journal of Power Sources*. **2016**. 325, 322-8.
- [18]. F. V. Avelar Dutra, B. C. Pires, T. A. Nascimento, V. Mano, *et al.* Polyaniline-deposited cellulose fiber composite prepared via in situ polymerization: enhancing adsorption properties for removal of meloxicam from aqueous media. *RSC Advances*. **2017**. 7(21), 12639-49.
- [19]. H. Wang, E. Zhu, J. Yang, P. Zhou, *et al.* Bacterial Cellulose Nanofiber-Supported Polyaniline Nanocomposites with Flake-Shaped Morphology as Supercapacitor Electrodes. *The Journal of Physical Chemistry C*. **2012**. 116(24), 13013-9.
- [20]. D. Xu, X. Xiao, J. Cai, J. Zhou, *et al.* Highly rate and cycling stable electrode materials constructed from polyaniline/cellulose nanoporous microspheres. *Journal of Materials Chemistry A*. **2015**. 3(32), 16424-9.
- [21]. S. K. Kandasamy, K. Kandasamy. Recent Advances in Electrochemical Performances of Graphene Composite (Graphene-Polyaniline/Polypyrrole/Activated Carbon/Carbon Nanotube) Electrode Materials for Supercapacitor: A Review. *Journal of Inorganic and Organometallic Polymers and Materials*. **2018**. 28(3), 559-84.
- [22]. N. A. Kumar, H.-J. Choi, Y. R. Shin, D. W. Chang, *et al.* Polyaniline-Grafted Reduced Graphene Oxide for Efficient Electrochemical Supercapacitors. *ACS Nano*. **2012**. 6(2), 1715-23.

2

Cellulose Fibers: An Overview

2.1. Introduction

“Back to nature” is the *mantra* of the modern world. The current worldwide trend is toward developing new products made from renewable and sustainable resources that are biodegradable, non-petroleum based, and have low environmental, animal/human health and safety risks [1, 2]. In this context, lignocellulosic biomass is the most abundant feedstock on earth and is one of the promising renewable and sustainable resources [3]. Lignocellulosic biomass consists of three major structural biopolymers, namely cellulose, hemicellulose, and lignin. Of these, cellulose is the most promising feedstock owing to its applications in various industries [1]. It has a fibrous structure consisting of insoluble bundles of linear D-glucose polymers held together by interchain hydrogen bonding and van der Waals interactions. Cellulose fibers are extracted from different sources; the fibers properties depend on their origin and the extraction methods used as well. For many centuries, cellulose has served humanity in a wide variety of applications, from crude building resources to feedstock for advanced synthetic materials [4].

This section aims to provide the reader with a comprehensive overview of cellulose and nanocellulose including, cellulose raw materials and extraction methods, structural features, morphologies, physicochemical properties and applications.

2.2. Lignocellulosic biomass

Lignocellulosic biomass refers to any material derived from living or once living material comprising lignin, cellulose and hemicellulose, including all plants and plant derived materials, i.e.,

agricultural crops and trees, wood and wood residues, municipal residues, and other residue materials. It is the largest amount of sustainable carbon material group and the most promising feedstock for the sustainable production of biochemical, bioethanol, and biofuels [5]. In particular, lignocellulosic biomass is a source of natural fibers that can replace petroleum-based polymers because of its exceptional ecological properties. In addition, biomass wastes, such as agricultural wastes and forest residues, have a high potential for reuse as fuel or feedstock for the production of high value-added materials without competition with human and animal food chains [6].

The cell wall of land plants forms an organic complex composite material that fulfills various functions. It is characterized by a framework of polysaccharides (see **Figure 2.1**), specifically crystalline cellulose nanofibrils embedded in an amorphous matrix containing hemicellulose, polyphenolic material (lignin), pectin, and proteins. However, the content ratio of these components varies due to the difference in species, types, and sources of lignocellulosic biomass [6-8]. Cellulose is the major constituent of the cell walls of plants, its structure, morphology and applications will be further discussed in this chapter. Hemicellulose is the second predominant component in a lignocellulosic biomass. It is an amorphous branched heteropolymer of pentoses (C5 carbohydrates), hexoses (C6 carbohydrates), and sugar acids; the ratio of which depends on the type of biomass. Hemicellulose serves as an interfacial coupling agent between highly polar cellulose and less polar lignin matrix [6, 9]. Hemicellulose common types are xylans, which are abundantly present in hardwood and glucomannans, which are mostly found in softwood [6]. In recent years, applications of hemicellulose have been widely investigated, particularly in the manufacturing of food additives, emulsifiers, plastic films for the protection and foods or superabsorbent hydrogels [10]. However, application of hemicelluloses in area such as packaging and biomedicine still holds considerable promise for the future [11]. Lignin represents about 10–25 wt.% of dry lignocellulosic biomass, it binds together the different components of the cell wall, and confers a rigid, impermeable, resistance to microbial attack and oxidative stress. Lignin is an amorphous heteropolymer network of phenyl propane units (p-coumaryl, coniferyl and sinapyl alcohol) held together by different linkages [6, 12]. Recently, there has been a vast growing enthusiasm for developing novel lignin-based derivatives for practical applications in many fields such as adsorbents, flocculants, adhesives, anti-oxidants, energy storing films, and vehicles for drug delivery and gene therapy [13].

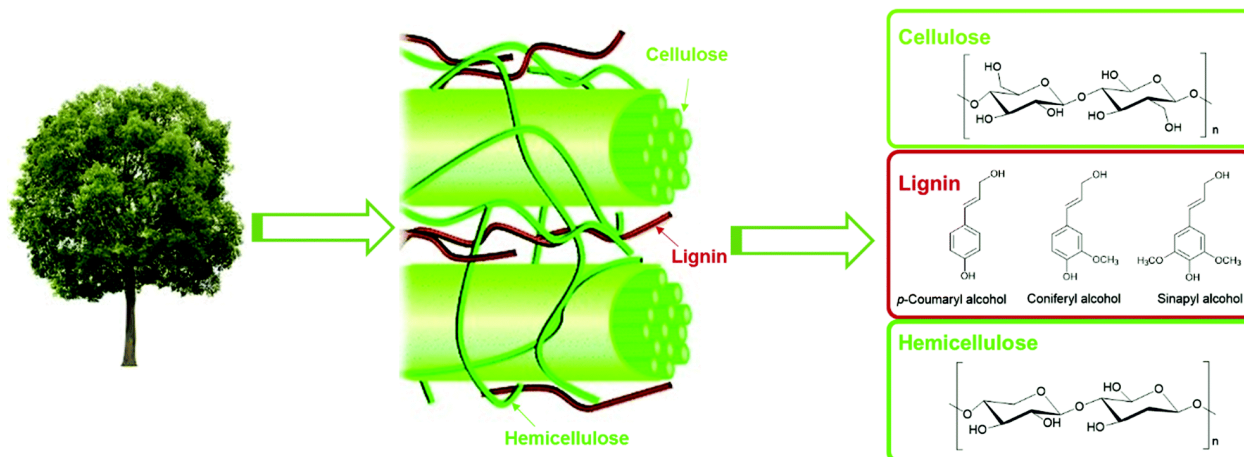


Figure 2.1: Structure of lignocellulosic biomass containing cellulose, hemicellulose, and lignin. [14]

2.3. Cellulose, an insight

Cellulose is the most abundant, renewable polymer resource on the planet. It has been estimated that about 10^{11} - 10^{12} tons are synthesized annually by photosynthesis in a rather pure form, i.e., in the seed hairs of the cotton plant, but mostly is combined with lignin and hemicelluloses in the cell walls of woody plants [15]. It is certainly one of the most important structural elements in plants and other living species. Its existence as the common material of plant cell walls was first investigated by Braconnot in 1819 [16] and Payen in 1838 [17]. In 1839, the resulting carbohydrate was named “cellulose” in a report of the French Academy, which evaluated Payen's work [18]. Cellulose has been used for centuries in highly diverse applications, mainly in the form of intact wood and textile fibers such as cotton or flax, or in the form of paper and board. Moreover, cellulose is a versatile starting material for chemical conversions, aiming at the production of artificial, cellulose derivatives used in many areas of industry and domestic life such as food, printing, cosmetic, oil well drilling, textile, pharmaceutical and biomedical applications [1, 19]. In addition to the empirical knowledge acquired over thousands of years on dyeing cellulose fibers and biodegradation of cellulose by rotting ...etc., cellulose and its derivatives have been widely studied recently, with the focus on their biological, chemical, and mechanical properties [20, 21].

2.4. Molecular Structure of cellulose

Understanding molecular structure of cellulose is important to explain its characteristic properties, such as hydrophilicity, biodegradability and high functionality [20]. **Figure 2.2** illustrates the structure and the inter- and intra-chain hydrogen bonding pattern in cellulose I.

Cellulose is a linear polysaccharide composed of $\beta(1-4)$ -linked D-glucopyranose ring units in the 4C_1 -chair conformation, which exhibits the lowest energy conformation. In contrast to the $\alpha(1-4)$ linkage as occurs in starch, The $\beta(1-4)$ linkage between glucose units, gives cellulose unique structural features. The successive glucose units are rotated by 180° relative to each other to form a disaccharide “cellobiose” with a length of 1.3 nm, which is the structural repetitive unit of the cellulose chain. Uridine diphosphate (UDP) glucose is the direct precursor for cellulose biosynthesis. Each anhydroglucose ring within the cellulose chain has three reactive hydroxyl groups; a primary group at C6, and two secondary groups at C2 and C3 positioned in the plane of the ring [20, 22, 23]. Furthermore, cellulose has several hydrogen bonding systems, which have a significant impact on its properties; for example, the limited solubility in most solvents, the reactivity of the $-OH$ groups, as well as the cellulose crystallinity are due to the strong hydrogen bonding systems. The intramolecular hydrogen bonds, together with the β -glycosidic covalent linkage, are responsible for the rigidity or stiffness of the cellulose polymer. While, intermolecular hydrogen bonding is responsible for the strong interaction between cellulose chains [22].

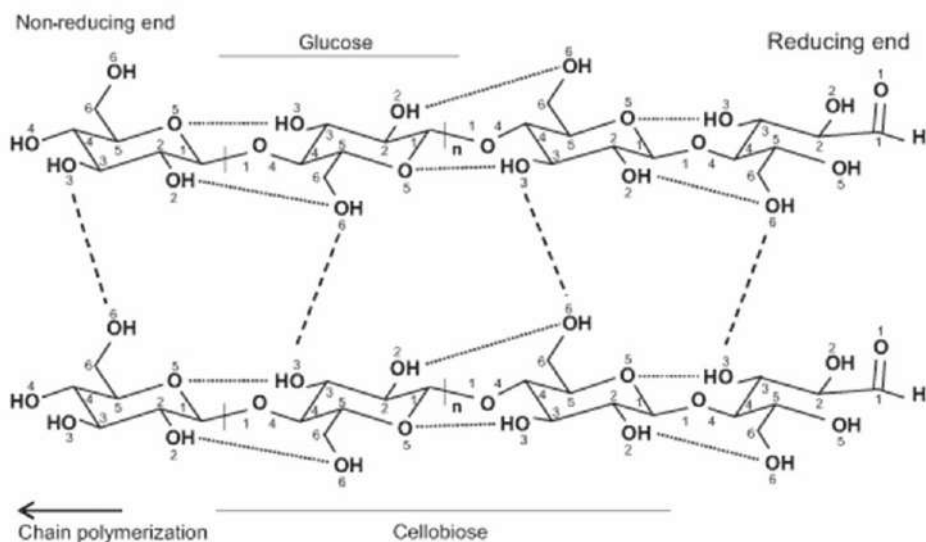


Figure 2.2: The structure and the inter- and intra-chain hydrogen bonding in cellulose I. [23]

As is typical for a polymer formed by “polycondensation”, two different ending groups are found in each cellulose chain edge; a non-reducing group is present where a closed ring structure is found. A reducing group with both an aliphatic structure and a carbonyl group is found at the other end of the chains. The cellulose chain is thus a polarized molecule. New glucose units are added at the non-reducing end allowing chain elongation [22-24]. The average number of repeated glucose units in each

chain, which is known as “the degree of polymerization (DP)”, significantly varies with the origin and treatment of the raw material. Cotton and other plant fibers have DP values in the range of 800-10000, while the DP values of wood pulp are typically 300-1700 [25].

2.5. Cellulose crystalline polymorphs

Different hydrogen-bonding configurations change the packing and molecular orientation of the cellulose chains, leading to the formation of different crystalline structures or polymorphs that differ in symmetry and chain geometry [6, 26]. Therefore, there are six different crystalline polymorphs of cellulose: cellulose I, II, III_I, III_{II}, IV_I, and IV_{II}. Cellulose II is the most crystalline thermodynamic stable form and its molecules are more densely packed, while cellulose I is the most abundant form found in nature. Cellulose I can be converted to other crystalline polymorphs by chemical or physical treatments (**Figure 2.3**). It presents in two different crystalline modifications, namely, cellulose I_α and I_β, which can be found alongside each other; the I_α/I_β ratio depends on the origin of the cellulose; higher plant cellulose mainly consists of cellulose I_β, whereas cellulose produced by primitive organisms crystallizes in the I_α phase [22, 23, 26].

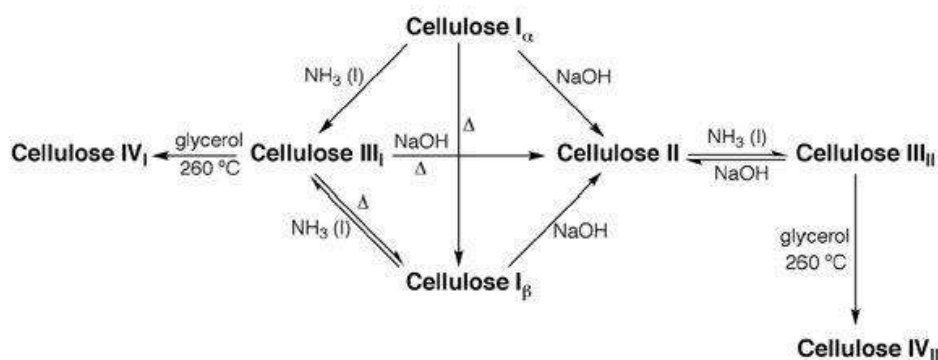


Figure 2.3: Transformation of cellulose into its different polymorphs. [27]

2.6. Sources and extraction of cellulose fibers

Cellulose fibers can be extracted from a variety of sources, such as annual plants, animals, and microbes. These include seed fiber (cotton), wood fibers (hardwoods and softwoods), bast fibers (flax, hemp, jute, ramie ... etc.), grasses (bagasse, bamboo ... etc.), simple marine animals, such as tunicates, algae, and bacteria [1]. However, commercial cellulose production concentrates on naturally highly pure sources such as cotton or on harvested sources such as wood [15]. Chemical composition of some typical cellulose-containing natural sources is exhibited in **Table 2.1**.

Table 2.1: Chemical composition of some typical cellulose-containing natural sources [15].

<i>Source</i>	<i>Composition (%)</i>			
	<i>Cellulose</i>	<i>Hemicellulose</i>	<i>Lignin</i>	<i>Extract</i>
Hardwood	43–47	23–25	16–24	2–8
North American	66–67	17–21	20–36	3–6
Softwood	40–44	25–29	25–32	1–5
Bagasse	40	30	20	10
Corn cobs	45	35	15	5
Corn stalks	35–45	25	17–21	4–7
Cotton	95	2	1	0.4
Flax (retted)	71	21	2	6
Flax (unretted)	63	12	3	13
Hemp	70	22	6	2
Henequen	78	4–8	13	4
Jute	71	14	13	2
Kenaf	36	21	18	2
Ramie	76	17	1	6
Rice straw	43	33	20	<1
Sisal	73	14	11	2
Sugarcane bagasse	45–55	20–25	18–24	>1
Wheat straw	30	50	15	5

The isolation of highly pure cellulose has been extensively studied for many years due to the complexity of the cell wall structure [28]. It would be necessary to combine both chemical and mechanical treatments in order to dissolve lignin, hemicellulose, and other non-cellulosic substances. A protocol based on acidified sodium chlorite is frequently applied to delignify woody materials as an initial step in the isolation of cellulose. Commonly, alkali treatment is performed to dissolve hemicelluloses before or after delignification. It is well known that treatment with chlorite can remove almost all of the lignin, and the following isolation of cellulose with alkali extraction can be performed at room temperature, which has been applied to isolate cellulose from woody materials for analysis for more than a century [29, 30].

Pulping and bleaching are two vital procedures widely used in paper industries to remove lignins, hemicelluloses, and other non-cellulosic substances and obtain pulp fiber with high cellulose purity and brightness through chemical and mechanical processes. In these procedures, NaOH, Na₂S, H₂SO₄, Na₂SO₃, NaHSO₃ and/or SO₂ are the major active chemicals used in chemical pulping for impregnation and delignification. However, the presence of excessive amounts of residual lignin in isolated cellulose fibers after delignification significantly affects their structure and properties. Fibers with high amounts of lignin are stiff and coarse, and have a brownish color. Therefore, it is challenging

to obtain fibers that are relatively free of residual lignin. To attain this goal, chemical bleaching, which is used to obtain fibers with higher cellulose content from delignified and unbleached fibers, is usually considered as a continuation of delignification process to isolate cellulose from woody raw materials [29].

Nowadays, there are various procedures for extraction of cellulose fibers including: delignification and alkali extraction, steam explosion, alkaline peroxide extraction, organic solvent extraction (Organosolv method), acid hydrolysis, and biological treatments [29]. The different processes result in varying fiber purities and strengths [22].

2.7. Nanocellulose

2.7.1. Types and properties

The term “nanocellulose”, which was first evolved publicly in the early 1980s, is widely used to describe a wide range of cellulose-based nanomaterials with at least one dimension in the nanometer scale. Depending on sources and dimensions, nanocellulose can be classified into three main categories: (I) cellulose nanocrystals (CNC), also known as nanocrystalline cellulose (NCC) and cellulose nanowhiskers (CNW), (II) cellulose nanofibers (CNF), also referred to as nanofibrillated cellulose (NFC) or microfibrillated cellulose (MFC), and (III) bacterial cellulose (BC) also identified as microbial cellulose or biocellulose [31, 32]. **Figure 2.4** shows TEM images of the three categories.

Nanocellulose is a biodegradable transparent material with low density (around 1.6 g/cm^3), high axial elastic modulus (up to 220 GPa) which is greater than that of Kevlar fiber, high tensile strength (up to 10 GPa) which is greater than that of cast iron, low coefficient of thermal expansion ($\sim 1 \text{ ppm/K}$), good thermal stability (up to $300 \text{ }^\circ\text{C}$), together with a strength/weight ratio of 8 times higher than that of stainless steel. Moreover, nanocellulose has a large reactive surface of hydroxyl groups which can be functionalized to various surface properties [6, 33, 34].

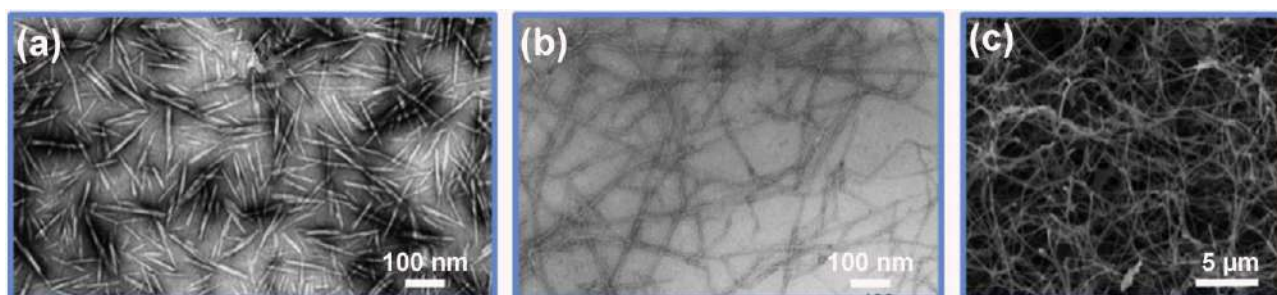


Figure 2.4: TEM micrographs of CNCs (a), CNFs (b), and SEM micrograph of BC (c). [31]

2.7.2. Preparation methods

Cellulose fibrils aggregate with (a) highly ordered regions (crystalline structure), and (b) disordered regions (amorphous structure) [17]. The former promote high stiffness and strength of cellulose, while the latter contribute to the flexibility of the bulk material. The aggregations of ordered and disordered regions consist of cellulose fibers of 3-100 μm in diameter and 1-4 mm in length for general lignocellulosic biomass [6]. Several methods have been developed to disintegrate cellulose fibers and prepare nanocellulose from cellulosic materials. These methods can be categorized into three main techniques: acid hydrolysis, mechanical processes, and biological approaches including enzymatic treatments. Different extraction methods resulted in differences in types and properties of the obtained nanocellulose [6, 35].

Currently, CNC are mainly produced by selective acid hydrolysis of amorphous cellulose regions under controlled temperature. A typical production process consists of acid hydrolysis, washing, centrifugation, dialysis, and sonication then drying. Removing the amorphous region of cellulose in the hydrolysis step results in highly crystalline particles with source-dependent dimensions, for instance, 5–20 nm diameter x 100–500 nm length, for plant source CNC. Sulfuric acid is most commonly used in hydrolysis process. It grafts negatively charged sulfate half-ester groups onto the surface of the particles, thereby preventing their re-aggregation in aqueous suspensions due to the resulting electrostatic repulsion between particles [31, 36].

CNC present as a liquid crystal solution in water due to concentration-dependent liquid crystalline self-assembly behavior. Thus results in macroscale, transparent, ordered films under normal evaporative conditions of CNC suspensions. CNC films have been extensively studied for various applications, mainly because of their chiral nematic organization and optical and mechanical properties as well as their gas barrier and water sorption capacities. However, the commercialization of CNC products is still very limited due to the time consuming production process and the low yield, especially when the initial sources contain high amounts of amorphous cellulose [31, 37].

On the other hand, the extraction of CNF from cellulosic fibers can be achieved by: (I) chemical treatments (e.g. TEMPO oxidation), (II) mechanical treatments (e.g. High pressure homogenization, cryocrushing, grinding, and milling), (III) enzymatic treatments, or (IV) combination of the previous treatments. However, the mechanical approach is the most commonly employed [31, 35].

Analogous to CNC, the fundamental characteristics of CNF also depend on the raw material source and the employed extraction process. However, unlike CNC which have near-perfect crystallinity, CNF are micrometer-long entangled fibrils that contain both amorphous and crystalline cellulose domains. Entanglement of the long particles leads to highly viscous aqueous suspensions even at relatively low concentrations (< 1 wt.%) [31, 35].

BC is synthesized extracellularly by cellulose-producing bacteria belonging to the genera: *Acetobacter* (*Gluconacetobacter*), *Agrobacterium*, *Acanthamoeba*, *Achromobacter*, *Zooglea*, *Aerobacter*, *Azotobacter*, *Rhizobium*, *Sarcina*, *Salmonella*, *Escherichia*, *Pseudomonas*, and *Alcaligenes*, with *Acetobacter xylinum* (or *Gluconacetobacter xylinus*) being the most efficient amongst them. To produce BC, Bacteria are cultivated for few days in an aqueous culture media containing glucose, phosphate, carbon, and nitrogen sources. The cell membrane of the cellulose-producing bacteria is composed of a network structure of ribbon-shaped cellulosic fibrils that are 20-100 nm wide, assembled from bundles of 2–4 nm wide nanofibrils. The structures and properties of the produced BC can be regulated by cultivation conditions such as nutrient source, oxygen ratio, bacterial strain type, incubation time, and cultivation in a bioreactor. Moreover, BC is synthesized as pure cellulose, unlike plant-derived nanocellulose, which may require pretreatment to remove lignin and hemicellulose before hydrolysis [31, 35, 37, 38].

2.7.3. Nanocellulose Applications

Nanocellulose, with its outstanding properties and biodegradability, is one of the most attractive materials for various applications in many fields such as nanocomposite materials, surface modified materials, and transparent papers with special functions [31, 39].

Cellulose-based nanocomposite materials show special properties including high mechanical strength and high thermal properties with lightweight and transparency. CNC, CNF and BC represent better alternatives for synthetic fillers to reinforce polymer nanocomposites used in various fields such as automotive industry, optoelectronics, energy storage, biosensors, tissue scaffolds, drug delivery, catalysis, packaging and furniture production...etc. [6, 18, 35].

For instance, Wang et al. [40] added nanocellulose extracted from soybean to three different polymers, namely, polyvinyl alcohol (PVA), polypropylene (PP) and polyethylene (PE), the resulting reinforced polymers exhibited significantly improved tensile strength and stiffness compared with the base polymers. In addition, Robles et al. [41] used nanocellulose obtained from blue agave bagasse as

reinforcement in poly (lactic acid) to form new composite materials with enhanced thermal properties and crystallization and a better interaction among matrix fillers.

Furthermore, nanocellulose can be used for surface modification of various substrates, owing to its high reactive surface area of hydroxyl groups. Direct chemical modification or covalent attachment of molecules with hydroxyl groups of nanocellulose surface is the most commonly used method [6]. In this context, Phanthong et al. [42] fabricated an amphiphobic nanocellulose-modified paper with super hydrophobic and oleophobic properties, by coating nanocellulose on a filter paper and treating the coated paper using chemical vapor deposition with trichloro(1H,1H,2H,2H-tridecafluoro-n-octyl)silane. Such anti-wetting property is very useful for developing special surfaces of self-cleaning, anti-bacterial and anti-reflective properties [42].

On the other hand, transparent and foldable nanocellulose-based films are applied in electronic devices, solar cells, flexible displays, and flexible circuits ...etc. [6, 31, 36]. For example, Nogi et al. [43] fabricated transparent nanocellulose paper from wood flour, with high-strength (223 MPa), high Young's modulus (13 GPa), and minimal thermal expansion (8.5 ppm/K) which is suitable for electronic devices.

Nanocellulose is also widely applied in medical field due to its low toxicity, biocompatibility, biodegradability and excellent physical properties [6, 44, 45]. For instance, nanocellulose dressing can be well adhered with wound and easily detached by itself after skin recovery [6, 31]. Hakkarainen et al. [46] used the nanofibrillated cellulose from the bleached birch pulp fibers for wound dressing, and found that the nanofibrillated cellulose was highly biocompatible with the skin graft donor sites. Other applications of nanocellulose in the medical field including drug excipients, drug delivery into target cells, immobilization and recognition of enzyme/protein, blood vessel and soft tissue replacements, skin and bone tissue repair materials, and antimicrobial materials are also investigated in recent years [44, 45].

Besides the above applications, nanocellulose is also applied in other fields such as thickener in cosmetics, texturing agent in food, filler of special textiles, biodegradable package, CO₂ adsorbent, oil recovery and many more [6, 36, 45, 47, 48].

2.8. References

- [1]. M. M. Khattab, N. A. Abdel-Hady, Y. Dahman. 21 - Cellulose nanocomposites: Opportunities, challenges, and applications, in *Cellulose-Reinforced Nanofibre Composites*, ed. by M. Jawaid, S. Boufi, A. K. H.P.S, Woodhead Publishing. **2017**. 483-516.
- [2]. H. Kargarzadeh, M. Mariano, D. Gopakumar, I. Ahmad, *et al.* Advances in cellulose nanomaterials. *Cellulose*. **2018**. 25(4), 2151-89.
- [3]. Y. T. Xiao, W. L. Chin, S. B. Abd Hamid. Facile Preparation of Highly Crystalline Nanocellulose by Using Ionic Liquid. *Advanced Materials Research*. **2015**. 1087, 106-10.
- [4]. N. Nagachar, J. McManus. Microbial Cellulose Synthesis, in *Microbial Factories: Biofuels, Waste treatment: Volume 1*, ed. by V. C. Kalia, Springer India, New Delhi. **2015**. 203-16.
- [5]. H. V. Lee, S. B. A. Hamid, S. K. Zain. Conversion of Lignocellulosic Biomass to Nanocellulose: Structure and Chemical Process. *The Scientific World Journal*. **2014**. 2014, 20.
- [6]. P. Phanthong, P. Reubroycharoen, X. Hao, G. Xu, *et al.* Nanocellulose: Extraction and application. *Carbon Resources Conversion*. **2018**. 1(1), 32-43.
- [7]. M. Sorieul, A. Dickson, J. S. Hill, H. Pearson. Plant Fibre: Molecular Structure and Biomechanical Properties, of a Complex Living Material, Influencing Its Deconstruction towards a Biobased Composite. *Materials*. **2016**. 9(8).
- [8]. R. J. Bernardo, M. F. Gírio, M. R. Łukasik. The Effect of the Chemical Character of Ionic Liquids on Biomass Pre-Treatment and Posterior Enzymatic Hydrolysis. *Molecules*. **2019**. 24(4).
- [9]. J. S. Borah, D. S. Kim. Recent development in thermoplastic/wood composites and nanocomposites: A review. *Korean Journal of Chemical Engineering*. **2016**. 33(11), 3035-49.
- [10]. G. Gallina, E. R. Alfageme, P. Biasi, J. García-Serna. Hydrothermal extraction of hemicellulose: from lab to pilot scale. *Bioresource Technology*. **2018**. 247, 980-91.
- [11]. N. M. L. Hansen, D. Plackett. Sustainable Films and Coatings from Hemicelluloses: A Review. *Biomacromolecules*. **2008**. 9(6), 1493-505.
- [12]. P. Bajpai. Structure of Lignocellulosic Biomass, in *Pretreatment of Lignocellulosic Biomass for Biofuel Production*, ed. by P. Bajpai, Springer Singapore, Singapore. **2016**. 7-12.
- [13]. E. Ten, W. Vermerris. Recent developments in polymers derived from industrial lignin. *Journal of Applied Polymer Science*. **2015**. 132(24).
- [14]. X. Zhang, H. Lei, S. Chen, J. Wu. Catalytic co-pyrolysis of lignocellulosic biomass with polymers: a critical review. *Green Chemistry*. **2016**. 18(15), 4145-69.
- [15]. T. Heinze, O. A. El Seoud, A. Koschella. Production and Characteristics of Cellulose from Different Sources, in *Cellulose Derivatives: Synthesis, Structure, and Properties*, ed. by T. Heinze, O. A. El Seoud, A. Koschella, Springer International Publishing, Cham. **2018**. 1-38.
- [16]. H. Braconnot. Sur la Conversion du Corps Ligneux en Gomme, en Sucre, et en un Acide d'une Nature Particulière, par le Moyen de l'Acide Sulfurique; Conversion de la Même Substance Ligneuse en Ulmine par la Potasse. *Annales de Chimie et de Physique*. **1819**. 12, 172-95.
- [17]. A. Payen. Mémoire sur la composition du tissu propre des plantes et du ligneux. *Comptes rendus*. **1838**. 7, 1052-6.
- [18]. A. K. Bharimalla, S. P. Deshmukh, N. Vigneshwaran, P. G. Patil, *et al.* Nanocellulose-Polymer Composites for Applications in Food Packaging: Current Status, Future Prospects and Challenges. *Polymer-Plastics Technology and Engineering*. **2017**. 56(8), 805-23.
- [19]. S. Hokkanen, A. Bhatnagar, M. Sillanpää. A review on modification methods to cellulose-based adsorbents to improve adsorption capacity. *Water Research*. **2016**. 91, 156-73.

- [20]. L. D. Rajapaksha, H. A. D. Saumyadi, A. M. P. B. Samarasekara, D. A. S. Amarasinghe, *et al.* Development of cellulose based light weight polymer composites, in *Book Development of cellulose based light weight polymer composites*, ed., ed. by Editor, City. **2017**. Chap. Chapter, 182-6.
- [21]. D. Klemm, H.-P. Schmauder, T. Heinze, E. J. Vandamme, *et al.* Cellulose, in *Biopolymers Online*. **2005**.
- [22]. T. Heinze. Cellulose: Structure and Properties, in *Cellulose Chemistry and Properties: Fibers, Nanocelluloses and Advanced Materials*, ed. by O. J. Rojas, Springer International Publishing, Cham. **2016**. 1-52.
- [23]. R. A. Festucci-Buselli, W. C. Otoni, C. P. Joshi. Structure, organization, and functions of cellulose synthase complexes in higher plants. *Brazilian Journal of Plant Physiology*. **2007**. 19, 1-13.
- [24]. P. Singh, H. Duarte, L. Alves, F. Antunes, *et al.* From cellulose dissolution and regeneration to added value applications—synergism between molecular understanding and material development, in *Cellulose-Fundamental Aspects and Current Trends*, InTech. **2015**.
- [25]. J. D. Fontana, H. S. Koop, M. Tiboni, A. Grzybowski, *et al.* Chapter 7 - New Insights on Bacterial Cellulose, in *Food Biosynthesis*, ed. by A. M. Grumezescu, A. M. Holban, Academic Press. **2017**. 213-49.
- [26]. K.-Y. Lee, A. Santmartí. Crystallinity and Thermal Stability of Nanocellulose, in *Nanocellulose and Sustainability*, CRC Press. **2018**. 67-86.
- [27]. R. Abouzeid. Advanced cellulose composites, preparation and properties. PhD Thesis. Grenoble. **2012**.
- [28]. E. S. Abdel-Halim. Preparation and characterization of poly(acrylic acid)-hydroxyethyl cellulose graft copolymer. *Carbohydrate Polymers*. **2012**. 90(2), 930-6.
- [29]. C.-F. Liu, R.-C. Sun. Chapter 5 - Cellulose, in *Cereal Straw as a Resource for Sustainable Biomaterials and Biofuels*, ed. by R.-C. Sun, Elsevier, Amsterdam. **2010**. 131-67.
- [30]. B. Ghanbarzadeh, H. Almasi. Biodegradable Polymers, in *Biodegradation-life of science*, ed. by C. Rolando, R. Francisca, InTechPublications, Croatia. **2013**. 141-86.
- [31]. T. Abitbol, A. Rivkin, Y. Cao, Y. Nevo, *et al.* Nanocellulose, a tiny fiber with huge applications. *Current Opinion in Biotechnology*. **2016**. 39, 76-88.
- [32]. N. L. V. Carreño, A. M. Barbosa, B. S. Noremberg, M. M. S. Salas, *et al.* Advances in Nanostructured Cellulose-based Biomaterials, in *Advances in Nanostructured Cellulose-based Biomaterials*, ed. by N. L. V. Carreño, A. M. Barbosa, B. S. Noremberg, M. M. S. Salas, S. C. M. Fernandes, J. Labidi, Springer International Publishing, Cham. **2017**. 1-32.
- [33]. T. Wongjaiyen, W. Brostow, W. Chonkaew. Tensile properties and wear resistance of epoxy nanocomposites reinforced with cellulose nanofibers. *Polymer Bulletin*. **2018**. 75(5), 2039-51.
- [34]. K. Nelson, T. Retsina, M. Iakovlev, A. van Heiningen, *et al.* American Process: Production of Low Cost Nanocellulose for Renewable, Advanced Materials Applications, in *Materials Research for Manufacturing: An Industrial Perspective of Turning Materials into New Products*, ed. by L. D. Madsen, E. B. Svedberg, Springer International Publishing, Cham. **2016**. 267-302.
- [35]. B. Thomas, M. C. Raj, A. K. B, R. M. H, *et al.* Nanocellulose, a Versatile Green Platform: From Biosources to Materials and Their Applications. *Chemical Reviews*. **2018**. 118(24), 11575-625.
- [36]. E. C. Lengowski, E. A. Bonfatti Júnior, M. M. N. Kumode, M. E. Carneiro, *et al.* Nanocellulose in the Paper Making, in *Sustainable Polymer Composites and Nanocomposites*, ed. by Inamuddin, S. Thomas, R. Kumar Mishra, A. M. Asiri, Springer International Publishing, Cham. **2019**. 1027-66.
- [37]. J. Rojas, M. Bedoya, Y. Ciro. Current trends in the production of cellulose nanoparticles and nanocomposites for biomedical applications, in *Cellulose-Fundamental Aspects and Current Trends*, Intech: Vigo, Spain. **2015**. Vol. 8, 193-228.

- [38]. A. Blanco, M. C. Monte, C. Campano, A. Balea, *et al.* Chapter 5 - Nanocellulose for Industrial Use: Cellulose Nanofibers (CNF), Cellulose Nanocrystals (CNC), and Bacterial Cellulose (BC), in *Handbook of Nanomaterials for Industrial Applications*, ed. by C. Mustansar Hussain, Elsevier. **2018**. 74-126.
- [39]. R. Singla, A. Guliani, A. Kumari, S. K. Yadav. Nanocellulose and Nanocomposites, in *Nanoscale Materials in Targeted Drug Delivery, Theragnosis and Tissue Regeneration*, ed. by S. K. Yadav, Springer Singapore, Singapore. **2016**. 103-25.
- [40]. B. Wang, M. Sain. Isolation of nanofibers from soybean source and their reinforcing capability on synthetic polymers. *Composites Science and Technology*. **2007**. 67(11), 2521-7.
- [41]. E. Robles, I. Urruzola, J. Labidi, L. Serrano. Surface-modified nano-cellulose as reinforcement in poly(lactic acid) to conform new composites. *Industrial Crops and Products*. **2015**. 71, 44-53.
- [42]. P. Phanthong, G. Guan, S. Karnjanakom, X. Hao, *et al.* Amphiphobic nanocellulose-modified paper: fabrication and evaluation. *RSC Advances*. **2016**. 6(16), 13328-34.
- [43]. M. Nogi, S. Iwamoto, A. N. Nakagaito, H. Yano. Optically Transparent Nanofiber Paper. *Advanced Materials*. **2009**. 21(16), 1595-8.
- [44]. N. Lin, A. Dufresne. Nanocellulose in biomedicine: Current status and future prospect. *European Polymer Journal*. **2014**. 59, 302-25.
- [45]. C. Guise, R. Fangueiro. Biomedical Applications of Nanocellulose, in *Book Biomedical Applications of Nanocellulose*, ed., ed. by Editor, Springer Netherlands, City. **2016**. Chap. Chapter, 155-69.
- [46]. T. Hakkarainen, R. Koivuniemi, M. Kosonen, C. Escobedo-Lucea, *et al.* Nanofibrillar cellulose wound dressing in skin graft donor site treatment. *Journal of Controlled Release*. **2016**. 244, 292-301.
- [47]. M. Kaushik, A. Moores. Review: nanocelluloses as versatile supports for metal nanoparticles and their applications in catalysis. *Green Chemistry*. **2016**. 18(3), 622-37.
- [48]. D. Klemm, E. D. Cranston, D. Fischer, M. Gama, *et al.* Nanocellulose as a natural source for groundbreaking applications in materials science: Today's state. *Materials Today*. **2018**. 21(7), 720-48.

3

Graphene and its properties

3.1. Introduction

Carbon is the fourth most abundant element in our Milky Way Galaxy, following hydrogen, helium, and oxygen [1]. It is the *materia prima* for life and the basis of all organic chemistry [2]. Due to carbon bond flexibility, carbon-based systems show a significantly large number of different structures with different physical properties [3]. Carbon allotropes are subject of intense theoretical and experimental investigations for their superb structural, electronic, and chemical properties, and while some carbon allotropes -such as graphite and diamond- are naturally found on earth as minerals, the others are synthetic. Following the 0D fullerenes (Buckyballs) and the 1D carbon nanotubes (Buckytubes), 2D graphene is the youngest representative of the synthetic carbon allotropes [4-6]. Graphene is a flat monolayer of carbon atoms packed into a two-dimensional (2D) hexagonal lattice. As **Figure 3.1** exhibits, graphene is the basic building block for graphitic materials of all other dimensionalities, since 2D graphene sheets can be wrapped into 0D buckyballs, rolled into 1D nanotubes, or stacked into 3D graphite [6-8]. Graphene as a planar conjugated carbon sheets has attracted the interest of theoreticians since the 1940's [9], when it was served as a model system for understanding the electronic properties of graphite, but it was long presumed not to exist in its free-standing form due to the thermodynamic instability of two-dimensional crystals according to the classical Mermin-Wagner theorem [10]. However, the latter theory was surprisingly challenged in 2004 by Novoselov, Geim and co-workers at Manchester University, when single layers of graphene were successfully isolated for the first time by mechanical cleavage [11]. Their groundbreaking experiments on graphene were honored with the Nobel Prize in Physics in 2010. Since its discovery, graphene with

its outstanding electrical, mechanical, thermal and optical properties, in particular, the high charge-carrier mobility, the excellent electrical and thermal conductivities, the large specific surface area combined with mechanical strength and transparency, make graphene an exciting field for theoretical studies and experimental research with thousands of papers published per year [12, 13]. Therefore, graphene and graphene-based materials are finding increasingly more applications in diverse technological sectors including electronic devices, sensors, composite materials, photodetectors, solar cells, energy storage devices, automotive industry and medicine.[12, 14]

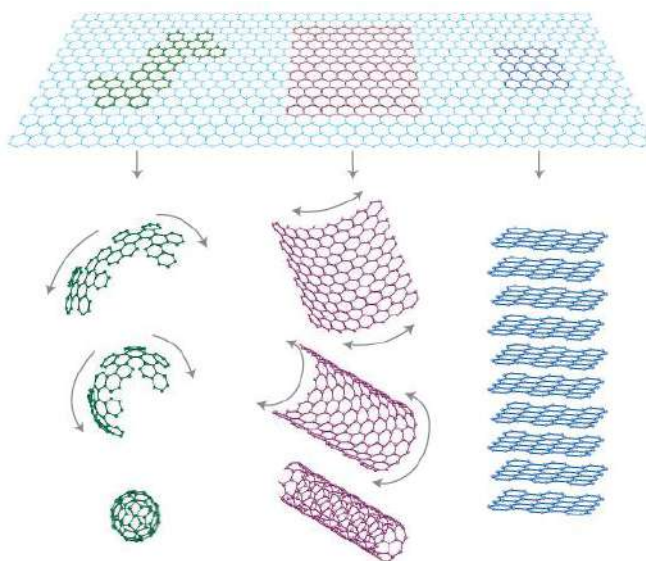


Figure 3.1: Graphene is the basic building block for all graphitic materials [7].

3.2. Graphene structure

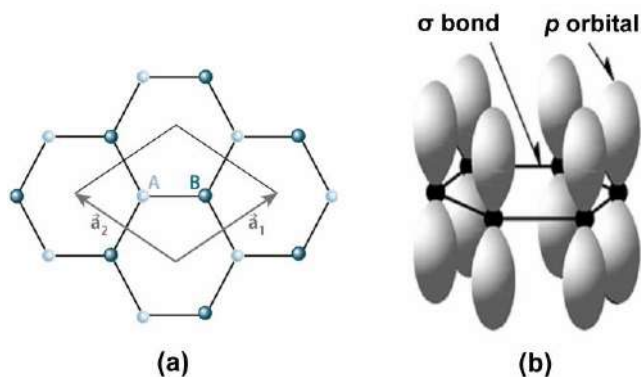


Figure 3.2: (a) Graphene hexagonal structure [15], (b) Schematic of the σ bonds and the p orbitals [16].

Graphene is a 2D crystal consisting of hexagonally arranged, covalently bonded carbon atoms, with a C-C bond length of 0.142 nm [8, 17]. The honeycomb lattice has a unit cell represented in **Figure 3.2 (a)**, by the vectors a_1 and a_2 , where $|a_1|=|a_2|=a$, with $a=2.461 \text{ \AA}$, each unit cell contains two atoms, A and B [15, 18]. The carbon atoms in graphene are sp^2 hybridized, which means that the s , p_x and p_y orbitals of carbon atoms form strong covalent σ bonds, while the remaining p_z orbital form π bonding, oriented perpendicular to the lattice (**Figure 3.2 (b)**) [16, 19]. The strong σ bondings are responsible for the mechanical robustness of the honeycomb framework, while the π -orbital electrons contribute to the formation of a delocalized electron network [17], which is responsible for the superior electrical conductivity of graphene [5, 19]. Moreover, Graphene can have some “intrinsic” corrugations or ripples and other defects such as topological shapes (pentagons, heptagons, or their combination), vacancies, adatoms, edges, cracks, and adsorbed impurities [17].

3.3. Graphene properties

3.3.1. Electronic properties

Graphene has attracted much interest primarily due to its extraordinary electronic properties [20]. Which depend on the layer thickness and stacking configurations [21]. Monolayer graphene is a zero bandgap semiconductor in which the empty conduction band meets the filled valence band at two Dirac points (K and K') (See **Figure 3.3**). It has a linear Dirac-like spectrum around the Fermi energy [21-24]. Bilayer graphene has a parabolic spectrum with an extremely small band overlap of 0.16 meV and can be also referred to as a zero-gap semiconductor [21, 22, 25]. Moreover, band structures for three and more graphene layers (**Figure 3.3 (c)**) become increasingly complicated along with the presence of several charge carriers and large overlaps of conduction and valence bands. [25] Electrons in graphene mimic massless relativistic particles (so called Dirac fermions), travelling at high Fermi velocity ($\sim 10^6 \text{ m/s}$) [26, 27]. Furthermore, The charge mobility of graphene supported on an insulating substrate is about $1.5 \times 10^4 \text{ cm}^2/\text{Vs}$, and $6 \times 10^4 \text{ cm}^2/\text{Vs}$ at 300 and 4 K, respectively, with electrons and holes in concentrations of about 10^{13} cm^{-2} [11, 28]. The low temperature mobility for suspended graphene can reach about $2 \times 10^5 \text{ cm}^2/\text{Vs}$ [29] and can even exceed $2.5 \times 10^5 \text{ cm}^2/\text{Vs}$ [30], which is >100 times higher than that of silicon ($1.5 \times 10^3 \text{ cm}^2/\text{Vs}$) [28]. Furthermore, graphene sheet resistance is as low as $\sim 30 \text{ \Omega/sq}$ due to its exceptional conductivity [31].

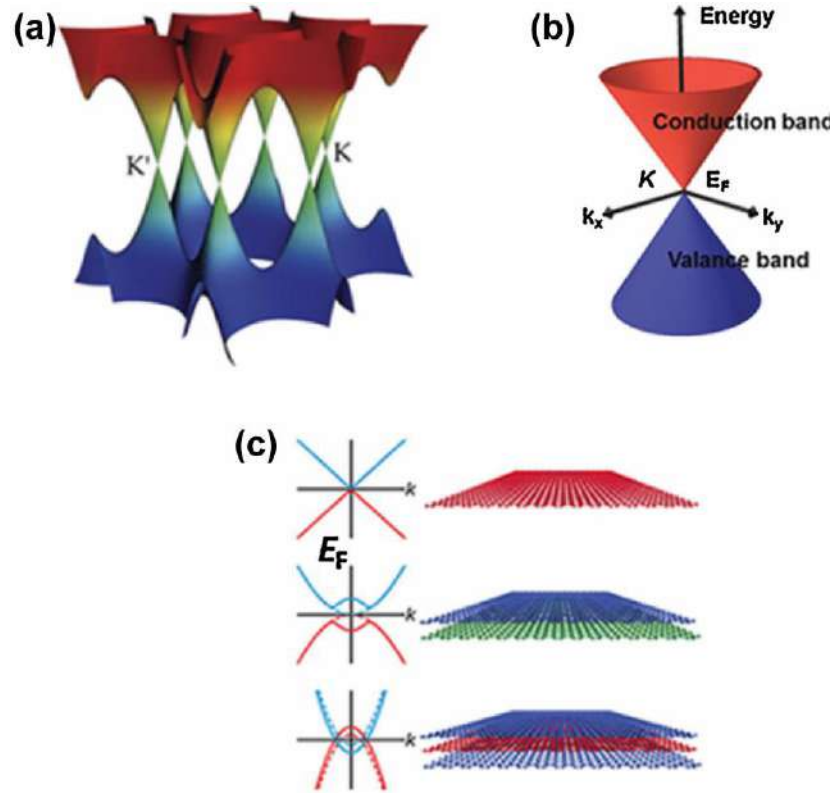


Figure 3.3: Electronic band structure of graphene: (a) the conduction band touches valence band at the K and K' points, and (b) linear band dispersion relation near the Dirac points showing gapless features, and (c) electronic properties of graphene depend on the layer number. [25]

3.3.2. Mechanical properties

The inherent strength is one of graphene's stand-out properties, it is the strongest material ever tested [32]. The mechanical properties of monolayer graphene have been investigated theoretically using quantum mechanics calculations, molecular dynamic simulations and continuum models [33]. Different theoretical values were reported by using different effective graphene sheet thicknesses, and different potential functions (force-constants) with several algorithms [33]. Reddy et al. [34] have described the mechanical properties of graphene sheets based on equivalent continuum modeling. They reported a Young's modulus value of around 1.11 TPa, which is the same as that obtained by Van Lier et al. [35] using *ab initio* methods. However, Gao and Hao [36] and Yanovsky et al. [37] reported graphene's Young's modulus values of 0.6-1.1 TPa and 0.737-1.127 TPa using quantum molecular dynamics simulation and quantum mechanics calculations, respectively.

Experimentally, Frank et al. [38] used the force displacement of an atomic force microscope (AFM) tip to measure the Young's modulus and the effective spring constant of stacks of graphene sheets (<5 layers) suspended over trenches patterned in SiO₂ film. The measured Young's modulus was found to be 0.5 TPa with a spring constant ranging from 1 to 5 N/m. Lee et al. [32] investigated the elastic properties and intrinsic breaking strength of graphene by an AFM nanoindentation technique on a free-standing monolayer graphene sheet suspended over an Si substrate with circular cavities, their reported values for Young's modulus and tensile strength were 1.0±0.1 TPa and 130 GPa, respectively. These reported values for graphene Young's modulus are about 5 times higher than that of steel (230 GPa) [24]. They also showed single layer graphene to have a breaking strength of 42 Nm⁻¹ which is over 200 times greater than that of steel. However, these values are believed to be dependent on the purity of graphene sheets [8, 32]. These impressive mechanical strength of graphene is attributed to its unique structural architecture and the strength of covalent σ bonds between carbon atoms [33]. Furthermore, monolayer graphene is the lightest material so far with a surface density of 0.77 mg/m² [39], and it is considered as the world's thinnest membrane that is impermeable to all gases including helium [40].

3.3.3. Thermal properties

Using a noncontact optothermal Raman measurement technique, a thermal conductivity value up to 5300 Wm⁻¹K⁻¹ was reported by Balandin et al. [41] for a mechanically exfoliated monolayer graphene sheet suspended over a wide trench in Si/SiO₂ substrate as shown in **Figure 3.4**. This reported thermal conductivity value is higher than that of diamond (2310 Wm⁻¹K⁻¹), multi-wall carbon nanotubes (3000 Wm⁻¹K⁻¹), single-wall carbon nanotubes (3500 Wm⁻¹K⁻¹) and far higher than that of copper (~400 Wm⁻¹K⁻¹) [8, 42]. Furthermore, graphene's thermal conductivities ranging from 10³ to 10⁴ Wm⁻¹ K⁻¹ were calculated theoretically using various methods [43].

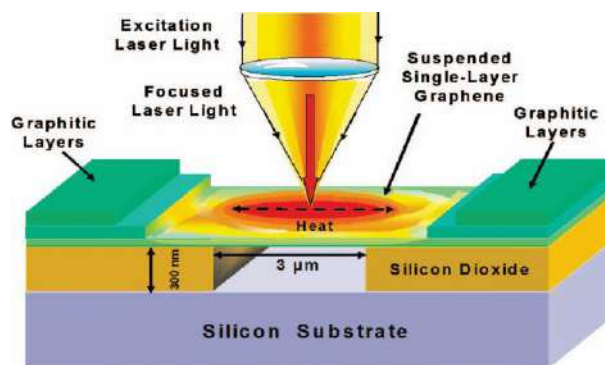


Figure 3.4: Schematic of the optothermal Raman measurement technique [41].

These outstanding thermal properties pave the way for graphene and graphene derivatives for different applications in thermal sensors, heat dissipators and composites with excellent thermal conductivities [8].

3.3.4. Optical properties

With moderately high optical transmittance (97.7 %), graphene materials show promise for transparent conductive films (TCFs) manufacturing [17] (see **Figure 3.5 (a)**). Experimental measurements showed a monolayer graphene sheet to absorb 2.3 % of the white light with negligible reflectance ($< 0.1\%$) [44], it is also observed that graphene's transmittance decreases linearly with the number of layers (**Figure 3.5 (b)**). Basically, each layer absorption $A = 1 - T \approx \pi \alpha \approx 2.3\%$; (where $\alpha = 2\pi e^2 / hc \approx 1/137$ is the fine structure constant, e is the electron charge, c is the light speed, and h is Planck's constant) [17].

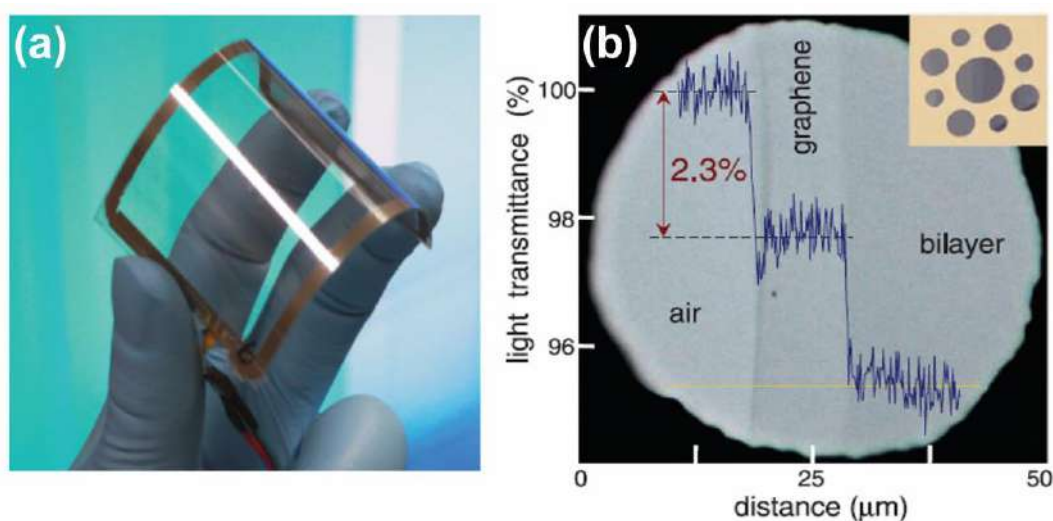


Figure 3.5: (a) An assembled graphene/PET touch panel [31], (b) white light transmittance through mono and bilayer graphene [44].

3.4. Graphene synthesis

It was in 1975 when B. Lang [45] reported the formation of few-layer graphite by thermally decomposed carbon on single crystal platinum (Pt) substrates, the layers were not designated as graphene due to a lack of characterization techniques or perhaps due to its limited possible applications. Scattered attempts to produce atomically thin layers of graphite have been reported since then. However, researchers have not shown much interest to extensively investigated the process due to the failure to identify the beneficial applications of the product and the lack of consistency between

properties of such graphite sheets formed on different crystal planes of metals [46]. In 2004, Andre Geim, Konstantin Novoselov and co-workers firstly isolated free-standing graphene sheet at Manchester University by the mechanical exfoliation technique using an adhesive tape [11]. This process was the first repeatable synthesis of graphene through exfoliation. Since then, there has been a huge interest in exploring graphene production methods and potential applications.

In the following, the main methods used for graphene synthesis are reviewed based on top-down and bottom-up approaches.

3.4.1. Mechanical exfoliation

In mechanical exfoliation, which is one of the top-down approaches, graphene is peeled from the bulk graphite layer by layer (**Figure 3.7**), thus overcoming the Van der Waals attraction between adjacent graphene flakes [47].

One such study was conducted by Ruoff's group in 1999, who isolated thin graphitic flakes on SiO₂ substrates by mechanical rubbing of patterned islands on highly oriented pyrolytic graphite (HOPG) without reporting any electrical characterization [48]. Later, in 2005, thinner graphite flakes (10 nm, ~30 layers) on Si/SiO₂ substrates were produced using a similar adapted approach and the electrical properties were reported [49]

In 2004, Geim et al. [11] first isolated graphene by repeated peeling of HOPG flake using an adhesive tape, the graphite flake gets thinner and thinner by continuous peeling, resulting in mono-, bi- and few-layer graphene which was identified by optical microscopy over specially prepared SiO₂(300 nm)/Si substrates. This simple but highly effective technique is called "Scotch tape method" or "micro-mechanical cleavage". In the same context, Huc et al. [50] have produced large (~10 μm) and flat graphene flakes by manipulating the substrate bonding of HOPG on Si substrate and controlled exfoliation. Likewise, Shukla et al. [51] prepared mm-sized mono- to few-layer graphene by bonding bulk graphite to borosilicate glass, followed by exfoliation to leave single- or few-layer of graphene on the substrate.

Mechanical exfoliation has produced the highest quality samples, but the method is neither high throughput nor high-yield [52]. Therefore, it cannot be used for industrial large-scale production, thus, other methods have been developed.

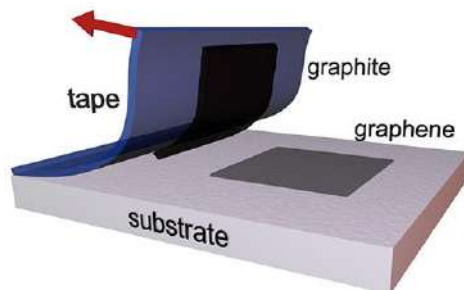


Figure 3.6: Schematic representation of micro-mechanical cleavage of graphite.

3.4.2. Liquid-phase exfoliation

Liquid-phase exfoliation (LPE) of graphite involves wet chemical dispersion in suitable liquid media in the presence or absence of surfactants followed by ultrasound or shear force induced exfoliation to extract single to few-layer graphene sheets. During exfoliation, the growth and collapse of the microscopic bubbles and voids in liquids due to pressure fluctuations act on the bulk graphite to overcome interlayer Van der Waal's forces and induce graphite exfoliation into smaller flakes gradually [8, 28]. The yield of monolayer graphene (up to 12 wt.%) and total concentration of graphene dispersions (up to 63 mg/mL) can be considerably improved through repeated exfoliation, extended sonication time, and subjecting to solvothermal and supercritical treatments [25].

The surface energy γ of graphene was estimated to be 46.7 mJ/m^2 [53]. Therefore, the suitable liquid medium should have close surface energy in order to minimize the interfacial tension between the solvent and the graphene layers [8]. N-methylpyrrolidone (NMP) ($\gamma=40.1 \text{ mJ/m}^2$), N,N-dimethylformamide (DMF) ($\gamma=37.1 \text{ mJ/m}^2$), and dimethyl sulfoxide (DMSO) ($\gamma=42.98 \text{ mJ/m}^2$), are the most used solvents, however, NMP is the best organic solvent for monolayer and few-layer graphene [25]. Other attempts to exfoliate graphite in low boiling point solvents such as acetone, propanol, Butanol, tetrahydrofuran, chloroform, etc. have been also reported [54-56]. Furthermore, direct exfoliation of graphite in water is impossible due to the high surface energy of water ($\gamma= 72.75 \text{ mJ/m}^2$) and the hydrophobic nature of graphene as well [8, 57]. These challenges are usually overcome by using various polymers, nonionic and ionic surfactants including poly(vinyl pyrrolidone), sodium cholate, 4-dodecylbenzenesulfonic acid, sodium deoxycholate, and sodium dodecylbenzenesulfonate [8, 28]. Such additives help to promote the exfoliation of graphite and ensure long-term stabilization of graphene suspensions, for instance, Ionic surfactants adsorbed on the sides of graphene sheets produce

charged sheets, thus prevents sheet aggregation due to coulomb repulsion [28]. The reader can be directed to [58] for a thorough investigation on surfactant-assisted graphite exfoliation.

Stable liquid-exfoliated graphene dispersions can be used to form flexible, transparent, conducting, and freestanding films, and can function as conducting inks for Inkjet-printed electronics [28].

3.4.3. Electrochemical exfoliation

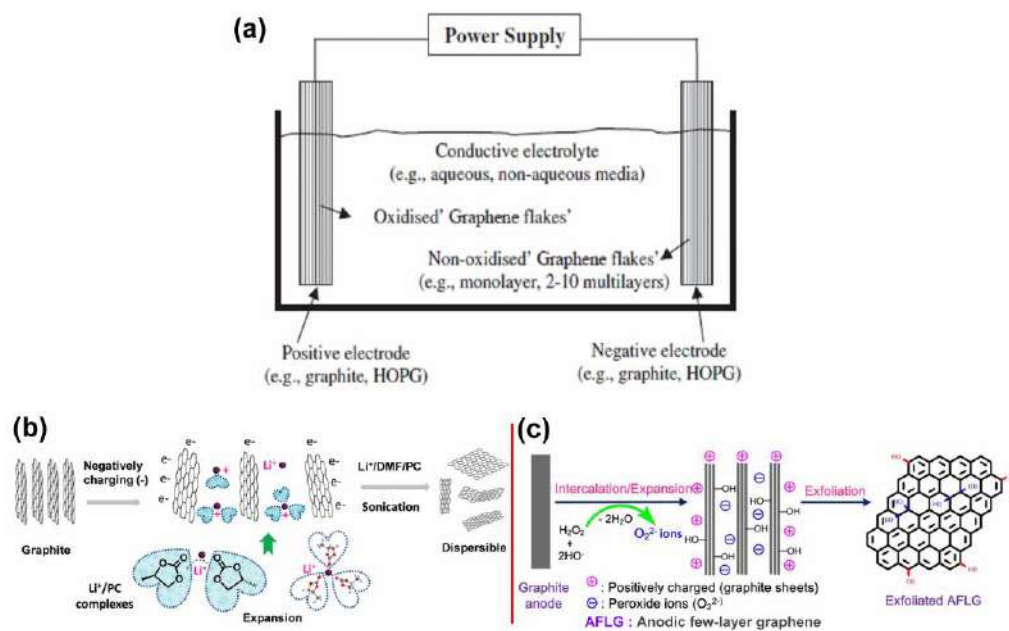


Figure 3.7: Schematic of an electrochemical cell used for graphite exfoliation (a) [59], and proposed mechanisms for graphite exfoliation in LiClO₄/PC electrolyte (b) [60], and in NaOH/H₂O₂/H₂O electrolyte (c) [61].

Electrochemical exfoliation is a form of large-scale production of graphene from natural graphite or HOPG rods or foils. Graphite is used for both working and counter electrodes (**Figure 3.7** (a)) or for working-electrode only [24, 62]. The electrodes were immersed into an electrolytic bath, i.e., organic electrolytes, aqueous electrolytes or electrolyte mixtures with surfactants and polymers [24, 28]. Electrolyte selection is essential for successful graphite exfoliation and active research in this field continues to identify the best aqueous and non-aqueous based electrolytes that can be used effectively to achieve efficient electrochemical graphite exfoliation [8]. In this regard, sulfuric acid (H₂SO₄) and phosphoric acid (H₃PO₄) are proven to be good options due to the intercalation of electrolyte anions,

radicals and their solvated complexes between graphite layers [28]. The process of exfoliation is usually started by applying a positive current to the electrodes. The graphite-based electrode will be oxidized and the electrolyte negatively charged ions will be intercalated into the layers of graphite. Subsequently, a negative potential is applied to facilitate the exfoliation process [8]. In a non-oxidative electrochemical process, negative graphite electrode is charged in LiClO_4 /propylene carbonate (PC) electrolyte (**Figure 3.7 (b)**). Thus, an expansion of the graphite electrode occurs during high current density charging (-15 ± 5 V) due to the co-intercalation of PC with Li^+ to form ternary graphite intercalated compounds (GICs). With sonication-assisted exfoliation of GICs in a mixture of DMF/PC, more than 70% of graphene sheets with layer number < 5 can be produced [25, 28, 60].

3.4.4. Graphene via reduction of graphene oxide

Reducing graphene oxide (GO) to reduced graphene oxide (rGO) is the most popular wet chemical method for graphene production in large quantities. Its popularity is due to low-cost, excellent yield, high scalability potential and the ability to disperse functionalized graphene in various solvents [63]. This method involves intercalation of graphite with an oxidant that introduces functional oxygen groups on the surface of graphene sheets, which help to disperse and stabilize GO homogeneously in water [8, 64] (see **Figure 3.8**). Generally, graphite is oxidized to graphite oxide using oxidants such as potassium permanganate in concentrated acidic media, based on Brodie method, Staudenmaier method, or Hummers method [65], which is the most widely used protocol with several modifications and improvements [8, 66]. Aqueous graphite oxide suspension is then sonicated to yield individual dispersed GO sheets in water. The aggressive chemical treatment of graphite introduces functional groups such as ($-\text{OH}$) and ($\text{C}-\text{O}-\text{C}$) in the basal plane, and ($\text{C}=\text{O}$) and ($-\text{COOH}$) on the edges of graphene sheets, in addition to five- and six-membered-ring lactols decorating along the peripheral edges of GO as well as esters of tertiary alcohols on the surface [8, 19, 25, 28].

Reduced GO (rGO) is basically a modified graphene, its structure and properties are closely match with pristine graphene [28]. rGO is obtained from GO through a reduction process. A lot of research is taking place in this area and different methods are developed for reducing GO. The quality, the properties and the potential areas of application of the produced graphene are significantly affected by the reduction method [8]. The defects introduced through the oxidation of graphite can be partially removed via the reduction processes. However, none of the current known methods can restore and completely remove all graphene defects caused by oxidation [8, 67]. It is therefore important to find

more efficient ways in which the quantity of functional groups introduced by oxidation on graphene surface can be easily controlled and minimized [8, 68].

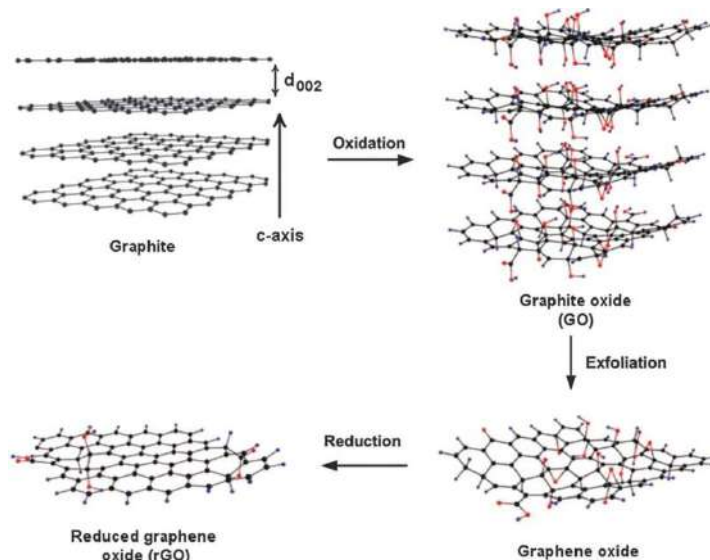


Figure 3.8: Schematic illustration of the preparation of reduced graphene oxide (rGO) from graphite [69].

Chemical, thermal and microwave are the three main current methods used to reduce GO [8]. Reducing agents used in chemical methods include hydrazine hydrate, phenyl hydrazine, hydroiodic acid, sodium borohydride, amino acid, pyrrole, dopamine, hydroquinone, glucose, and ascorbic acid [8, 65, 66]. In thermal methods, the oxygen containing functional groups are decomposed to CO_2 and H_2O [8, 70], due to thermal treatment of GO at high temperatures. Microwave irradiation was also effective in reducing GO to few-layer graphene [71].

Thermal and microwave treatment eliminate the need for chemical treatment, which may involve very toxic and dangerous materials such as hydrazine, especially in large volumes. However, high local temperatures on the surface ($> 1000\text{ }^\circ\text{C}$) can be detrimental, for example, on flexible substrates [8]. For more comprehensive reviews on GO reduction methods, the reader is referred to Refs. [67, 72].

3.4.5. Chemical vapor deposition

Chemical vapor deposition (CVD) is one of the most appropriate methods for scalable production of high quality and large-area graphene films [24, 73]. It involves the pyrolysis of hydrocarbon compounds on the surface of transition metal catalysts within a reaction chamber and

under processing conditions of gas flow rate, pressure, and temperature [24]. The quality of the final product, which is obtained as a film on a substrate, is mainly determined by the processing parameters [24, 25]. Various substrates can be used for graphene film growths including nickel (Ni) [74], copper (Cu) [75, 76], iron (Fe) [77], and cobalt (Co) [78]. Methane (CH_4), acetylene (C_2H_2), and other hydrocarbon gases are usually used as a carbon source [24]. Two main CVD methods are widely used to dissociate the carbon source, namely, thermal CVD and plasma-enhanced CVD (PECVD) [24, 79]. The main advantage of PECVD compared to thermal CVD is that it can be conducted at low temperature, low pressure and low concentration of carbon sources [24, 76, 80], however it generally produces graphene films of lower quality than thermal methods [81].

CVD process mechanism is illustrated in **Figure 3.9** and comprises eight steps [82]: (1) mass transport of the reactant, (2) reaction of the film precursor, (3) diffusion of gas molecules, (4) adsorption of the precursor, (5) diffusion of the precursor into the substrate, (6) surface reaction, (7) desorption of the product, and (8) removal of the byproduct.

In the case of thermal CVD, the substrate is typically pre-heated to around 1000 °C under a continuous flow of hydrogen and/or argon [81]. The growth itself is performed at high temperature ranging from 650 to 1000 °C. The high temperature, results in thermal decomposition of carbon sources into carbon and hydrogen atoms [24]. Hydrogen (H_2) and argon (Ar) can be used to maintain a reducing environment, and to fine-tune the pressure, respectively [81]. Moreover, Ar and H_2 were also used as carrier gases to remove unwanted oxides on the surface of the metal catalyst [24].

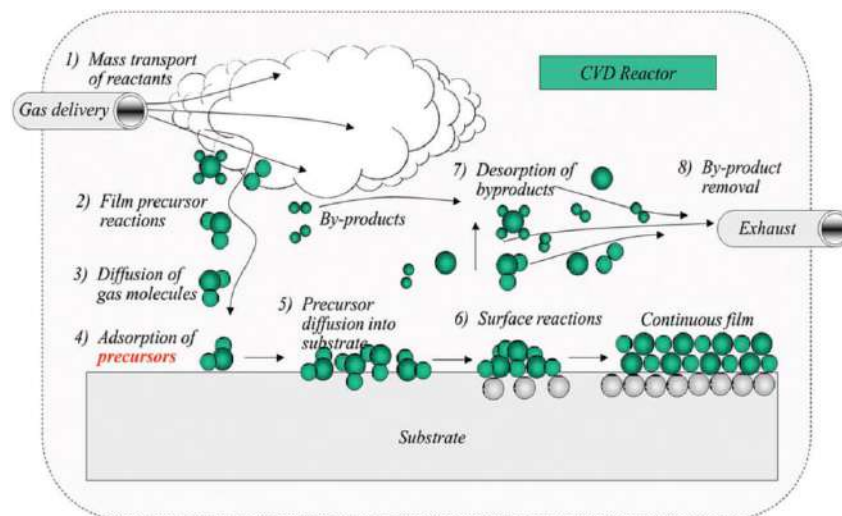


Figure 3.9: Diagram of the graphene growth mechanism by CVD method, transport and reaction processes [82].

It is noteworthy that current methods for transferring graphene involve attacking the metal substrate with etching agents. However, this results in higher costs, toxic wastes and structural damage to graphene [25].

3.4.6. Other methods

Other methods to produce graphene have also been developed over the past few years including, unzipping carbon nanotubes longitudinally to yield thin elongated graphene strips called “graphene nanoribbons (GNRs)” [19] through metal-catalyzed cutting, oxidation and reduction, plasma etching, Laser irradiation, intercalation and exfoliation, and sonication ... etc. (**Figure 3.10 (a)**) [83]. In addition to epitaxial growth of graphene on silicon carbide SiC, wherein, SiC is thermally decomposed to produce monolayer graphene through the graphitization of SiC by silicon (Si) sublimation during high temperature vacuum annealing (**Figure 3.10 (b)**) [19, 25, 28].

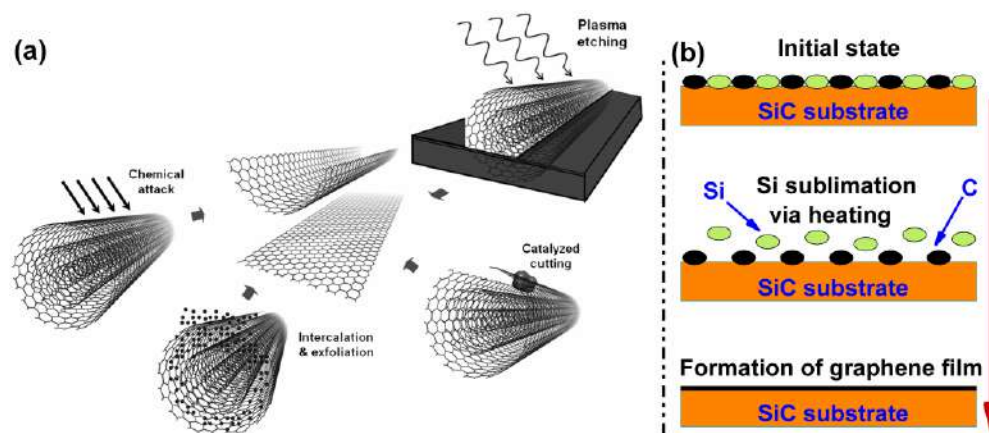


Figure 3.10: (a) Illustration of several techniques for CNTs unzipping [83], and (b) typical steps of graphene epitaxial growth on an SiC substrate.

3.5. Reference

- [1]. L. M. Ziurys, D. T. Halfen, W. Geppert, Y. Aikawa. Following the Interstellar History of Carbon: From the Interiors of Stars to the Surfaces of Planets. *Astrobiology*. **2016**. 16(12), 997-1012.
- [2]. A. H. Castro Neto, F. Guinea, N. M. R. Peres, K. S. Novoselov, *et al.* The electronic properties of graphene. *Reviews of Modern Physics*. **2009**. 81(1), 109-62.
- [3]. N. A. A. Ghany, S. A. Elsherif, H. T. Handal. Revolution of Graphene for different applications: State-of-the-art. *Surfaces and Interfaces*. **2017**. 9, 93-106.
- [4]. A. Hirsch. The Graphene Flagship—A Giant European Research Project. *Angewandte Chemie International Edition*. **2015**. 54(32), 9132-3.
- [5]. A. G. Pandolfo, A. F. Hollenkamp. Carbon properties and their role in supercapacitors. *Journal of Power Sources*. **2006**. 157(1), 11-27.

- [6]. Y. Chen, Y. Xie, S. A. Yang, H. Pan, *et al.* Nanostructured Carbon Allotropes with Weyl-like Loops and Points. *Nano Letters*. **2015**. 15(10), 6974-8.
- [7]. A. K. Geim, K. S. Novoselov. The rise of graphene. *Nature Materials*. **2007**. 6, 183.
- [8]. J. Phiri, P. Gane, T. C. Maloney. General overview of graphene: Production, properties and application in polymer composites. *Materials Science and Engineering: B*. **2017**. 215, 9-28.
- [9]. P. R. Wallace. The Band Theory of Graphite. *Physical Review*. **1947**. 71(9), 622-34.
- [10]. N. D. Mermin. Crystalline Order in Two Dimensions. *Physical Review*. **1968**. 176(1), 250-4.
- [11]. K. S. Novoselov, A. K. Geim, S. V. Morozov, D. Jiang, *et al.* Electric Field Effect in Atomically Thin Carbon Films. *Science*. **2004**. 306(5696), 666.
- [12]. A. C. Ferrari, F. Bonaccorso, V. Fal'ko, K. S. Novoselov, *et al.* Science and technology roadmap for graphene, related two-dimensional crystals, and hybrid systems. *Nanoscale*. **2015**. 7(11), 4598-810.
- [13]. S. Eigler, A. Hirsch. Chemistry with Graphene and Graphene Oxide—Challenges for Synthetic Chemists. *Angewandte Chemie International Edition*. **2014**. 53(30), 7720-38.
- [14]. J. I. Paredes, S. Villar-Rodil, P. Solís-Fernández, M. J. Fernández-Merino, *et al.* Preparation, characterization and fundamental studies on graphenes by liquid-phase processing of graphite. *Journal of Alloys and Compounds*. **2012**. 536, S450-S5.
- [15]. M. S. Dresselhaus, A. Jorio, R. Saito. Characterizing Graphene, Graphite, and Carbon Nanotubes by Raman Spectroscopy. *Annual Review of Condensed Matter Physics*. **2010**. 1(1), 89-108.
- [16]. J. Hass, W. A. d. Heer, E. H. Conrad. The growth and morphology of epitaxial multilayer graphene. *Journal of Physics: Condensed Matter*. **2008**. 20(32), 323202.
- [17]. Y. Zhu, S. Murali, W. Cai, X. Li, *et al.* Graphene and Graphene Oxide: Synthesis, Properties, and Applications. *Advanced Materials*. **2010**. 22(35), 3906-24.
- [18]. N. M. R. Peres. The transport properties of graphene. *Journal of Physics: Condensed Matter*. **2009**. 21(32), 323201.
- [19]. H. C. Lee, W.-W. Liu, S.-P. Chai, A. R. Mohamed, *et al.* Review of the synthesis, transfer, characterization and growth mechanisms of single and multilayer graphene. *RSC Advances*. **2017**. 7(26), 15644-93.
- [20]. S.-a. Peng, Z. Jin, D. Zhang, J. Shi, *et al.* How Do Contact and Channel Contribute to the Dirac Points in Graphene Field-Effect Transistors? *Advanced Electronic Materials*. **2018**. 4(8), 1800158.
- [21]. L. Zhang, Z. Liu. Photochemistry of Graphene, in *Photofunctional Layered Materials*, ed. by D. Yan, M. Wei, Springer International Publishing, Cham. **2015**. 213-38.
- [22]. B. Partoens, F. M. Peeters. From graphene to graphite: Electronic structure around the K point. *Physical Review B*. **2006**. 74(7), 075404.
- [23]. F. Fresno. Heterojunctions: Joining Different Semiconductors, in *Design of Advanced Photocatalytic Materials for Energy and Environmental Applications*, ed. by J. M. Coronado, F. Fresno, M. D. Hernández-Alonso, R. Portela, Springer London, London. **2013**. 311-27.
- [24]. Y. Seekaew, O. Arayawut, K. Timsorn, C. Wongchoosuk. Chapter Nine - Synthesis, Characterization, and Applications of Graphene and Derivatives, in *Carbon-Based Nanofillers and Their Rubber Nanocomposites*, ed. by S. Yaragalla, R. Mishra, S. Thomas, N. Kalarikkal, H. J. Maria, Elsevier. **2019**. 259-83.
- [25]. Y. Yang, C. Han, B. Jiang, J. Iocozzia, *et al.* Graphene-based materials with tailored nanostructures for energy conversion and storage. *Materials Science and Engineering: R: Reports*. **2016**. 102, 1-72.
- [26]. K. S. Novoselov, A. K. Geim, S. V. Morozov, D. Jiang, *et al.* Two-dimensional gas of massless Dirac fermions in graphene. *Nature*. **2005**. 438(7065), 197-200.
- [27]. R. Geetha Bai, N. Ninan, K. Muthoosamy, S. Manickam. Graphene: A versatile platform for nanotheranostics and tissue engineering. *Progress in Materials Science*. **2018**. 91, 24-69.

- [28]. M. Chakraborty, M. S. J. Hashmi. Wonder material graphene: properties, synthesis and practical applications. *Advances in Materials and Processing Technologies*. **2018**. 4(4), 573-602.
- [29]. X. Du, I. Skachko, A. Barker, E. Y. Andrei. Approaching ballistic transport in suspended graphene. *Nature Nanotechnology*. **2008**. 3, 491.
- [30]. M. Orlita, C. Faugeras, P. Plochocka, P. Neugebauer, *et al.* Approaching the Dirac Point in High-Mobility Multilayer Epitaxial Graphene. *Physical Review Letters*. **2008**. 101(26), 267601.
- [31]. S. Bae, H. Kim, Y. Lee, X. Xu, *et al.* Roll-to-roll production of 30-inch graphene films for transparent electrodes. *Nature Nanotechnology*. **2010**. 5, 574.
- [32]. C. Lee, X. Wei, J. W. Kysar, J. Hone. Measurement of the Elastic Properties and Intrinsic Strength of Monolayer Graphene. *Science*. **2008**. 321(5887), 385.
- [33]. F. Memarian, A. Fereidoon, M. Darvish Ganji. Graphene Young's modulus: Molecular mechanics and DFT treatments. *Superlattices and Microstructures*. **2015**. 85, 348-56.
- [34]. C. D. Reddy, S. Rajendran, K. M. Liew. EQUIVALENT CONTINUUM MODELING OF GRAPHENE SHEETS. *International Journal of Nanoscience*. **2005**. 04(04), 631-6.
- [35]. G. Van Lier, C. Van Alsenoy, V. Van Doren, P. Geerlings. Ab initio study of the elastic properties of single-walled carbon nanotubes and graphene. *Chemical Physics Letters*. **2000**. 326(1), 181-5.
- [36]. Y. Gao, P. Hao. Mechanical properties of monolayer graphene under tensile and compressive loading. *Physica E: Low-dimensional Systems and Nanostructures*. **2009**. 41(8), 1561-6.
- [37]. Y. G. Yanovsky, E. A. Nikitina, Y. N. Karnet, S. M. Nikitin. Quantum mechanics study of the mechanism of deformation and fracture of graphene. *Physical Mesomechanics*. **2009**. 12(5), 254-62.
- [38]. I. W. Frank, D. M. Tanenbaum, A. M. van der Zande, P. L. McEuen. Mechanical properties of suspended graphene sheets. *Journal of Vacuum Science & Technology B: Microelectronics and Nanometer Structures Processing, Measurement, and Phenomena*. **2007**. 25(6), 2558-61.
- [39]. M. Chakraborty, M. S. J. Hashmi. International research effort on graphene over the past 10 years. *Advances in Materials and Processing Technologies*. **2018**. 4(1), 166-82.
- [40]. J. S. Bunch, S. S. Verbridge, J. S. Alden, A. M. van der Zande, *et al.* Impermeable Atomic Membranes from Graphene Sheets. *Nano Letters*. **2008**. 8(8), 2458-62.
- [41]. A. A. Balandin, S. Ghosh, W. Bao, I. Calizo, *et al.* Superior Thermal Conductivity of Single-Layer Graphene. *Nano Letters*. **2008**. 8(3), 902-7.
- [42]. W. Jang, Z. Chen, W. Bao, C. N. Lau, *et al.* Thickness-Dependent Thermal Conductivity of Encased Graphene and Ultrathin Graphite. *Nano Letters*. **2010**. 10(10), 3909-13.
- [43]. A. A. Balandin. Thermal properties of graphene and nanostructured carbon materials. *Nature Materials*. **2011**. 10, 569.
- [44]. R. R. Nair, P. Blake, A. N. Grigorenko, K. S. Novoselov, *et al.* Fine Structure Constant Defines Visual Transparency of Graphene. *Science*. **2008**. 320(5881), 1308.
- [45]. B. Lang. A LEED study of the deposition of carbon on platinum crystal surfaces. *Surface Science*. **1975**. 53(1), 317-29.
- [46]. W. Choi, I. Lahiri, R. Seelaboyina, Y. S. Kang. Synthesis of Graphene and Its Applications: A Review. *Critical Reviews in Solid State and Materials Sciences*. **2010**. 35(1), 52-71.
- [47]. M. Yi, Z. Shen. A review on mechanical exfoliation for the scalable production of graphene. *Journal of Materials Chemistry A*. **2015**. 3(22), 11700-15.
- [48]. X. Lu, M. Yu, H. Huang, R. S. Ruoff. Tailoring graphite with the goal of achieving single sheets. *Nanotechnology*. **1999**. 10(3), 269-72.
- [49]. Y. Zhang, J. P. Small, W. V. Pontius, P. Kim. Fabrication and electric-field-dependent transport measurements of mesoscopic graphite devices. *Applied Physics Letters*. **2005**. 86(7), 073104.

- [50]. V. Huc, N. Bendiab, N. Rosman, T. Ebbesen, *et al.* Large and flat graphene flakes produced by epoxy bonding and reverse exfoliation of highly oriented pyrolytic graphite. *Nanotechnology*. **2008**. 19(45), 455601.
- [51]. A. Shukla, R. Kumar, J. Mazher, A. Balan. Graphene made easy: High quality, large-area samples. *Solid State Communications*. **2009**. 149(17), 718-21.
- [52]. M. J. Allen, V. C. Tung, R. B. Kaner. Honeycomb Carbon: A Review of Graphene. *Chemical Reviews*. **2010**. 110(1), 132-45.
- [53]. S. Wang, Y. Zhang, N. Abidi, L. Cabrales. Wettability and Surface Free Energy of Graphene Films. *Langmuir*. **2009**. 25(18), 11078-81.
- [54]. A. O'Neill, U. Khan, P. N. Nirmalraj, J. Boland, *et al.* Graphene Dispersion and Exfoliation in Low Boiling Point Solvents. *The Journal of Physical Chemistry C*. **2011**. 115(13), 5422-8.
- [55]. F. Fedi, F. Ricciardella, T. Polichetti, M. L. Miglietta, *et al.* Exfoliation of Graphite and Dispersion of Graphene in Solutions of Low-Boiling-Point Solvents for Use in Gas Sensors, in *Book Exfoliation of Graphite and Dispersion of Graphene in Solutions of Low-Boiling-Point Solvents for Use in Gas Sensors*, ed., ed. by Editor, Springer International Publishing, City. **2014**. Chap. Chapter, 143-7.
- [56]. L. Xu, J.-W. McGraw, F. Gao, M. Grundy, *et al.* Production of High-Concentration Graphene Dispersions in Low-Boiling-Point Organic Solvents by Liquid-Phase Noncovalent Exfoliation of Graphite with a Hyperbranched Polyethylene and Formation of Graphene/Ethylene Copolymer Composites. *The Journal of Physical Chemistry C*. **2013**. 117(20), 10730-42.
- [57]. X. Cui, C. Zhang, R. Hao, Y. Hou. Liquid-phase exfoliation, functionalization and applications of graphene. *Nanoscale*. **2011**. 3(5), 2118-26.
- [58]. R. Narayan, S. O. Kim. Surfactant mediated liquid phase exfoliation of graphene. *Nano Convergence*. **2015**. 2(1), 20.
- [59]. C. T. J. Low, F. C. Walsh, M. H. Chakrabarti, M. A. Hashim, *et al.* Electrochemical approaches to the production of graphene flakes and their potential applications. *Carbon*. **2013**. 54, 1-21.
- [60]. J. Wang, K. K. Manga, Q. Bao, K. P. Loh. High-Yield Synthesis of Few-Layer Graphene Flakes through Electrochemical Expansion of Graphite in Propylene Carbonate Electrolyte. *Journal of the American Chemical Society*. **2011**. 133(23), 8888-91.
- [61]. K. S. Rao, J. Senthilnathan, Y.-F. Liu, M. Yoshimura. Role of Peroxide Ions in Formation of Graphene Nanosheets by Electrochemical Exfoliation of Graphite. *Scientific Reports*. **2014**. 4, 4237.
- [62]. P. Yu, S. E. Lowe, G. P. Simon, Y. L. Zhong. Electrochemical exfoliation of graphite and production of functional graphene. *Current Opinion in Colloid & Interface Science*. **2015**. 20(5-6), 329-38.
- [63]. Y. L. Zhong, Z. Tian, G. P. Simon, D. Li. Scalable production of graphene via wet chemistry: progress and challenges. *Materials Today*. **2015**. 18(2), 73-8.
- [64]. V. Singh, D. Joung, L. Zhai, S. Das, *et al.* Graphene based materials: Past, present and future. *Progress in Materials Science*. **2011**. 56(8), 1178-271.
- [65]. M. S. A. Bhuyan, M. N. Uddin, M. M. Islam, F. A. Bipasha, *et al.* Synthesis of graphene. *International Nano Letters*. **2016**. 6(2), 65-83.
- [66]. B. L. Dasari, J. M. Nouri, D. Brabazon, S. Naher. Graphene and derivatives – Synthesis techniques, properties and their energy applications. *Energy*. **2017**. 140, 766-78.
- [67]. S. Pei, H.-M. Cheng. The reduction of graphene oxide. *Carbon*. **2012**. 50(9), 3210-28.
- [68]. G. Eda, M. Chhowalla. Chemically Derived Graphene Oxide: Towards Large-Area Thin-Film Electronics and Optoelectronics. *Advanced Materials*. **2010**. 22(22), 2392-415.
- [69]. H. Bai, C. Li, G. Shi. Functional Composite Materials Based on Chemically Converted Graphene. *Advanced Materials*. **2011**. 23(9), 1089-115.

- [70]. C. Vallés, J. David Núñez, A. M. Benito, W. K. Maser. Flexible conductive graphene paper obtained by direct and gentle annealing of graphene oxide paper. *Carbon*. **2012**. 50(3), 835-44.
- [71]. H. J. Han, Y. N. Chen, Z. J. Wang. Effect of microwave irradiation on reduction of graphene oxide films. *RSC Advances*. **2015**. 5(113), 92940-6.
- [72]. C. K. Chua, M. Pumera. Chemical reduction of graphene oxide: a synthetic chemistry viewpoint. *Chemical Society Reviews*. **2014**. 43(1), 291-312.
- [73]. Z. Yan, Z. Peng, J. M. Tour. Chemical Vapor Deposition of Graphene Single Crystals. *Accounts of Chemical Research*. **2014**. 47(4), 1327-37.
- [74]. F. Yavari, Z. Chen, A. V. Thomas, W. Ren, *et al.* High Sensitivity Gas Detection Using a Macroscopic Three-Dimensional Graphene Foam Network. *Scientific Reports*. **2011**. 1, 166.
- [75]. Y. Seekaew, D. Phokharatkul, A. Wisitsoraat, C. Wongchoosuk. Highly sensitive and selective room-temperature NO₂ gas sensor based on bilayer transferred chemical vapor deposited graphene. *Applied Surface Science*. **2017**. 404, 357-63.
- [76]. T.-o. Terasawa, K. Saiki. Growth of graphene on Cu by plasma enhanced chemical vapor deposition. *Carbon*. **2012**. 50(3), 869-74.
- [77]. H. An, W.-J. Lee, J. Jung. Graphene synthesis on Fe foil using thermal CVD. *Current Applied Physics*. **2011**. 11(4, Supplement), S81-S5.
- [78]. S. M. Wang, Y. H. Pei, X. Wang, H. Wang, *et al.* Synthesis of graphene on a polycrystalline Co film by radio-frequency plasma-enhanced chemical vapour deposition. *Journal of Physics D: Applied Physics*. **2010**. 43(45), 455402.
- [79]. L. Cheng, K. Yun, A. Lucero, J. Huang, *et al.* Low temperature synthesis of graphite on Ni films using inductively coupled plasma enhanced CVD. *Journal of Materials Chemistry C*. **2015**. 3(20), 5192-8.
- [80]. Y. Okigawa, R. Kato, T. Yamada, M. Ishihara, *et al.* Electrical properties and domain sizes of graphene films synthesized by microwave plasma treatment under a low carbon concentration. *Carbon*. **2015**. 82, 60-6.
- [81]. K. E. Whitener, P. E. Sheehan. Graphene synthesis. *Diamond and Related Materials*. **2014**. 46, 25-34.
- [82]. V. P. Pham, H.-S. Jang, D. Whang, J.-Y. Choi. Direct growth of graphene on rigid and flexible substrates: progress, applications, and challenges. *Chemical Society Reviews*. **2017**. 46(20), 6276-300.
- [83]. L. Ma, J. Wang, F. Ding. Recent Progress and Challenges in Graphene Nanoribbon Synthesis. *Chemphyschem*. **2013**. 14(1), 47-54.

4

Supercapacitors and their electrode materials

4.1. Background

In today's world, the need for more energy is steadily increasing. Both households and industries require large amounts of power [1]. As a result, finding a way to power the future while maintaining a robust socio-economic growth and a clean environment is one of the biggest challenges will be faced in the coming decades [2].

Although energy storage and conversion is a historical subject of research and commercial efforts, the increase in energy consumption and the depletion of fossil fuels as well as the increased levels of pollution have sparked a keen interest in harnessing energy from renewable bio-friendly sources such as sunlight, wind, and water. However, the lack of continuous availability of these alternate sources demands efficient and affordable energy storage devices and technologies for sustained supply. The existing technologies range from rechargeable batteries with capacities on the order of mWh to “pumped storage hydroelectricity” at MWh or greater scales. [1, 3, 4]

The driving force behind the continuous development of diverse energy conversion and storage technologies was and still is the cost resulting from, i.e., availability of resources, active materials synthesis, devices manufacturing, energy capacity, power capability, provision reliability, service life, recyclability, and environmental impact [3]. Batteries, supercapacitors and fuel cells are recognized as the most important energy storage/conversion devices.

Supercapacitors or ultra-capacitors, with high power densities and extended cycle lives over commercial batteries play an important role as promising energy storage systems for solving the thorny issues of fossil fuel exhaustions and climatic changes [5]. Using high specific surface area electrodes and thinner dielectrics, supercapacitors attain higher capacitances while sharing the same fundamental principles as conventional capacitors. They have energy densities greater than those of conventional capacitors and power densities higher than those of batteries [6]. For such properties, supercapacitors have received considerable attention from both academia and industry as they meet the needs of a wide range of energy storage applications requiring fast, safe and stable charging cycles, such as backup systems, portable devices and electric vehicles [5].

4.2. Brief history and basic principles

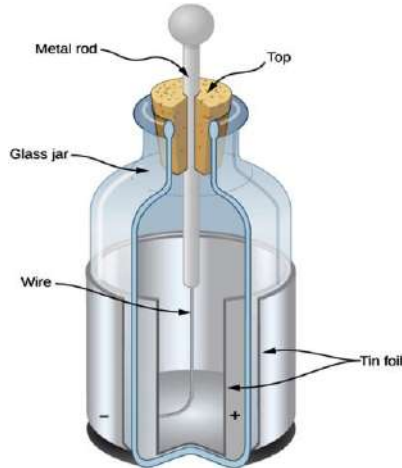


Figure 4.1: Schematic of the Leyden jar [7].

The Leyden jar, which was invented independently in 1745 and 1746, was considered as the first device for storing electrical charge, it is the ancestor of the modern capacitors. It consisted of two metal foils coated on the inner and outer surfaces of an insulative container, and a metal rod inserted vertically through the jar lid to make contact with the inner foil (**Figure 4.1**) [7-9]. This led to the discovery of parallel-plate capacitors, in which two conductive plates separated by a dielectric medium accumulate equal but opposite charges, resulting in an electric field between the plates. The dielectric is generally an electrically insulating material such as ceramic, polymer, liquid, or even a vacuum [7]. In 1886, electrolytes were initially developed as dielectrics by Charles Pollak [7, 10], who invented the first stable electrolytic capacitor [11].

In 1957, Becker H.I. described the concept of the earliest prototype of electrochemical double-layer capacitors (EDLCs) based on carbon with a high specific surface area (SSA) coated on a metallic current collector in an H_2SO_4 solution [7, 12, 13]. In the 1970s, NEC (Nippon Electric Company, Japan) developed and successfully marketed the EDLCs under SOHIO's license for CMOS memory power-saving units in electronics, NEC introduced the term "Supercapacitor" and this application was considered as the starting point for electrochemical capacitors use in commercial devices [6, 13].

4.3. Supercapacitors classification

Based on the dominant energy storage mechanism, supercapacitors are classified into three categories: electrochemical double-layer capacitors (EDLCs), pseudocapacitors, and hybrid supercapacitors (HSCs) [6, 14, 15].

4.3.1. Electrochemical double-layer capacitors (EDLCs)

An electric double layer is a structure that appears when a charged object is immersed into a liquid. The ions in the liquid accumulate at the object/fluid interface to counter balance the surface charge through Coulomb's force, thus, an electric double-layer is formed (i.e., a layer of surface charge and a layer of ions). The separation between the surface charge and the attracted oppositely charged ions is on the order of nanometers. Such a small separation would result in an ultra-high capacitance at the object/fluid interface, a feature which is exploited in supercapacitors [6, 10, 16-18].

As illustrated in **Figure 4.2**, several models were proposed to describe the aforementioned solid/liquid interface, namely; the Helmholtz model, the Gouy–Chapman model and the Stern model. (in **Figure 4.2**: Ψ is the potential, Ψ_0 is the electrode potential, IHP is the inner Helmholtz plane, and OHP is the outer Helmholtz plane).

The German physicist Helmholtz first proposed the existence of an electrical double layer due to the buildup of charges of opposite signs across the electrode/electrolyte interface, the electrolyte ions are rigidly arranged at a " d " distance from the electrode. It was the simplest approximation for modeling the spatial charge distribution at double layer interfaces, though it does not adequately explain what occurs in nature.

The Helmholtz model was further modified by Gouy and Chapman taking into account that the ions are mobile in the electrolyte solutions and not rigidly attached to the surface. The electrolyte ions are under the combined influences of diffusion and electrostatic forces, resulting in the so-called

“diffuse layer”. However, the Gouy-Chapman model fails to estimate the experimental data of interfacial capacitance, since it considers the ions as point charges and that they can approach the surface with no limits, which is not true. Later, Stern stated that the ions do have a finite size, so cannot approach the surface with no limits, he combined both Helmholtz and Gouy-Chapman models to reorganize two ion diffusion layers, i.e., a compact layer (also called the Stern layer) and a diffuse layer [7, 10, 16, 19-21].

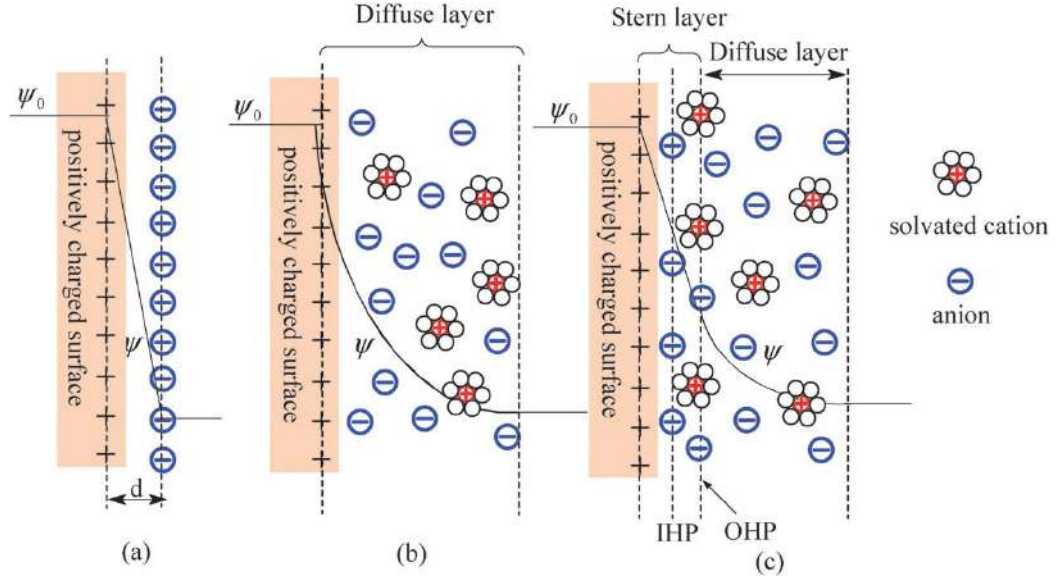


Figure 4.2: The electrical double layer models, (a) Helmholtz model, (b) Gouy-Chapman model, and (c) Stern model. [21]

Therefore, in EDLCs, both the compact and the diffuse layers contribute to the total capacitance. Moreover, as equation (4.1) indicates, the equivalent circuit of the entire double-layer for each electrode can be treated as the series connection of the capacitances $C_{compact}$ and $C_{diffuse}$. [10]

$$\frac{1}{C_{total}} = \frac{1}{C_{compact}} + \frac{1}{C_{diffuse}} \quad (4.1)$$

The charging schematic of EDL capacitor is illustrated in **Figure 4.3**. There is no electron transfer or ion exchange across the interface, only a physical adsorption of ions is involved. Furthermore, the ionically permeable separator prevents short circuiting the two conducting plates [22, 23].

EDLCs main advantage is that they can withstand millions of cycles, since there is no physical change in the electrodes during charge and discharge processes [6, 15].

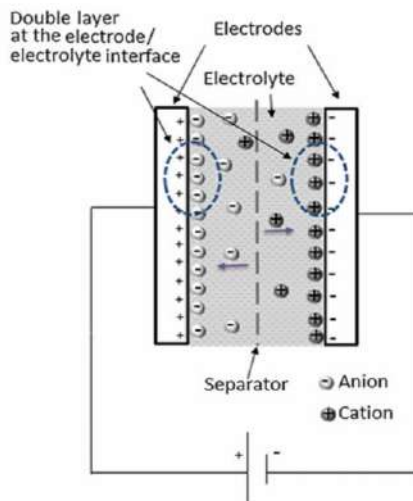


Figure 4.3: Charging schematic of EDL capacitor [22].

4.3.1.1. Electrode materials for EDLCs

As the stored charge and the capacitance in EDLCs essentially depend on their electrode materials, carbon-based materials with a high accessible surface area such as activated carbon, carbon nanotube (CNTs), carbon nanofibers and graphene are usually used. Activated carbon is the most common electrode material used in commercial EDLCs, due to its high SSA and low cost. Graphene with its outstanding properties, as discussed in previous chapter, is proved to be suitable for developing high performance energy storage devices with enhanced rate capabilities and improved capacities. [6, 10, 13, 24]

It is worth mentioning that for porous electrode materials such as activated carbon, the ions mobility into the pores is significantly influenced by the pore size, thereby ions do not move in the bulk electrolyte the same way as they do within the pores of an electrode material. Generally, too small pores do not contribute to double layer capacitance due to their inaccessibility to the electrolyte ions. On the other hand, too wide pores contain more free space not used for capacitive charge storage. Therefore, it is necessary to tune pore sizes in order to have carbon materials with narrow, short and electrolyte-accessible pores. [16, 25]

4.3.2. Pseudocapacitors

Compared to EDLCs, where charge storage is governed by the electrostatic mechanism, pseudocapacitors store charge via faradaic processes involving charge transfer across the electrode/electrolyte interface via thermodynamically and kinetically favored electrochemical

reduction/oxidation (redox) reactions. The charge quantity (q) resulting from the reaction changes continuously with the electrode potential (V), thus, the proportionality constant (dq/dV) is called the pseudocapacitance. The power performance of an EDLC is usually higher than that of pseudocapacitors due to the slower faradaic processes involved. Nevertheless, these faradaic processes allow pseudocapacitors to achieve higher specific capacitances as compared to EDLCs. [6, 10, 16]

For a pseudocapacitive electrode, several charge storage mechanisms can be distinguished, namely, redox reactions of transition metal oxides, reversible electrochemical doping/dedoping in conducting polymers (CPs), under-potential deposition, and intercalation pseudocapacitance. [16, 26]

As an example, **Figure 4.4** illustrates the proton adsorption and the redox process of hydrous ruthenium oxide ($\text{RuO}_2 \cdot x\text{H}_2\text{O}$) in a pseudocapacitor electrode [27].

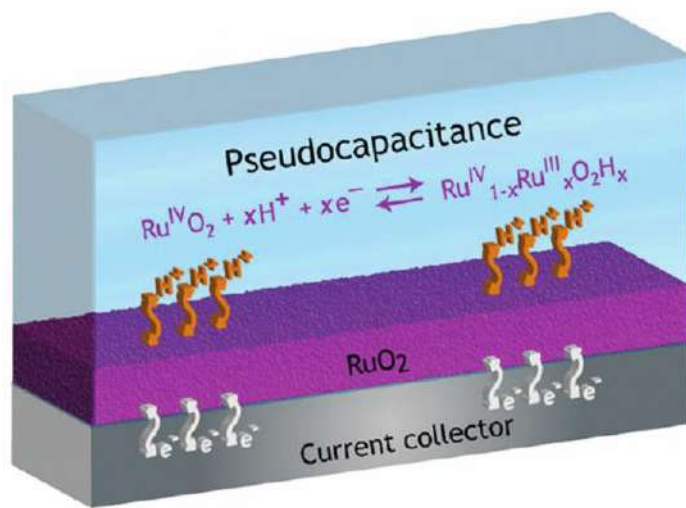


Figure 4.4: Schematic of charge storage via pseudocapacitance [27].

4.3.2.1. Common pseudocapacitive materials

A. Metal oxides

The electrode materials are the prime components of supercapacitors. As popular pseudocapacitive electrode materials, transition metal oxides have been extensively studied owing to their unique layered structure and the wide variety of oxidation states. The pseudocapacitance of metal oxides rises from the extremely fast and reversible intercalation of metal ions into the lattice, and the reversible surface chemical reactions. RuO_2 , IrO_2 , MnO_2 , Co_3O_4 , V_2O_5 , TiO_2 , NiO and MoO_3 are examples of metal oxides that are commonly used for electrode materials.

Ruthenium oxide (RuO_2) is reported to have a specific capacitance over 700 Fg^{-1} , which is around 6 times higher than those of porous carbon materials. It is the most studied metal oxide, however, its high cost and toxicity have severely limited the commercial usages of RuO_2 -based supercapacitors. Hence, researchers worldwide focus on other cheaper and less toxic alternative metal oxides/hydroxides such as, MnO_2 , Co_3O_4 , Fe_3O_4 , $\text{Co}(\text{OH})_2$, and V_2O_5 . [28, 29]

B. Conducting polymers

Polymers are defined as macromolecules composed of chemical units (monomers) that are repeated 'n' times throughout a chain. In Greek "poly" means "many" and "mer" means "parts" [30]. Cellulose, chitosan, starches, xanthan gum and proteins are examples of natural polymers, while synthetic polymers include nylon, Teflon and polyethylene and many more. In fact, the human body itself is partly composed of polymer substances, such as deoxyribonucleic acid (DNA), which is found in every cell nucleus, and keratin in hair and nails.

It was traditionally referred to polymers as electrical insulators. However, in 1977, a novel class of polymers known as intrinsically conducting polymers or electroactive conjugated polymers was discovered. Alan J. Heeger, Alan G. MacDiarmid, and Hideki Shirakawa shared the 2000 Nobel Prize in Chemistry for this scientific breakthrough. Conducting polymers (CPs) with their interesting properties have attracted the whole scientific community for a wide range of applications such as sensors, supercapacitors, polymeric batteries, light emitting diodes (LEDs), Solar cells, Field effect transistors (FETs), corrosion inhibitors, etc. [31-34]

Commonly, CPs are synthesized via; directly catalyzed synthesis [35], chemical oxidation of the monomer [36], electrochemical oxidation [37], plasma oxidation [38], and out of precursor polymers [39]. However, other methods are less used, including photoinitiated polymerization, synthesis in the inverse emulsion, condensation polymerization, and monomer oxidation with a cathodically generated intermediary during the reduction of the dissolved O_2 . [34]

CPs have several features that make them suitable materials for supercapacitors, such as low environmental impact, low cost, high conductivity in a their doped states, adjustable redox activity through chemical modification, fast charge/discharge, as well as relatively high storage capacity. However, they suffer from undergoing mechanical/chemical changes like swelling, shrinkage, cracks or breaking during long term charging/discharging processes, as a result, the working potential window of the CPs electrodes is limited by degradation over oxidation.

The most commonly used CPs for supercapacitor electrodes include polyaniline (PANI), polypyrrole (PPy), polythiophene (PTh) and poly-[3,4-ethylenedioxythiophene] (PEDOT) [40, 41].

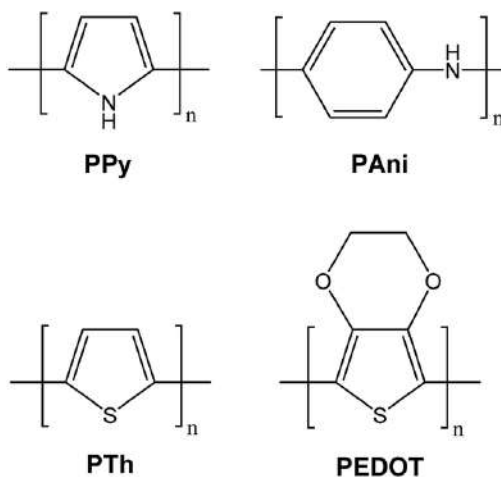


Figure 4.5: Chemical structures of main conducting polymers (CPs) used in supercapacitors.

CPs conductivity is achieved through oxidation or reduction reaction, a process termed as “doping”, which involves removing electrons from the valence band (p-doping), or adding electrons to the conduction band (n-doping), thus charge carrier counter ions (e.g. Cl^-) are required to be entrapped or released from the polymer chain, in order to cause delocalization of electrons. Such process generates charge carriers (negative (electrons) or positive (holes)) that move to opposite electrodes upon the application of an electric field. This movement is what is actually responsible for electrical conductivity. PANI, PPy and most CPs can only be p-doped, PTh and its derivatives can be either n-doped or p-doped. [24, 40, 42]

The p-doping (oxidation) and n-doping (reduction) processes can be described by the following equations, where A^- and C^+ represent the anion and cation.



CPs offer capacitance behavior through reversible redox processes i.e., doping/dedoping. Therefore, ions are transferred to the polymer backbone upon doping then released back into the electrolyte upon dedoping. These reactions in the CP occur throughout its entire bulk volume, not just

on the surface as it is observed in carbon electrodes. The doping/dedoping are highly reversible and do not involve any phase changes. [40, 43]

Unlike EDL electrode materials, the typical cyclic voltammogram of a CP electrode exhibits current peaks at redox potentials of the polymer, resulting in a deviation from the rectangular shape. Metal oxide electrodes, on the other hand, can show series of redox reactions giving a nearly rectangular cyclic voltammogram [16].

B.1. Polyaniline (PANI)

The monomer “aniline” was discovered independently by Otto Unverdorben in 1826 who named it “krystallin”, F. Ferdinand Runge in 1834 who named it “kyanol”, Carl J. Fritzsche in 1840 who called it “Anilin”, and Nikolai Zinin in 1842 who named it “benzidam”. Later, in 1843, August W. Hofmann has concluded that the previously reported substances were the same compound, which eventually became known as phenylamine or aniline [30].

Both Runge and Fritzsche have reported in 1834 and 1840 that the treatment of the oils they isolated with oxidizing agents resulted in the formation of various dark insoluble dyes, which could be practically commercialized. In 1862, Letheby developed the anodic oxidation of aniline and obtained a bluish-green precipitate at the anode. These resultant products from aniline became ultimately known as polyaniline (PANI). However, PANI did not come into common use until the rediscovery of this material in 1985 by MacDiarmid and co-workers as a conducting polymer. [30, 44]

Electrical conductivity and other properties of PANI are highly dependent on its oxidation states. PANI exists in different oxidation states, namely, fully reduced designated as leucoemeraldine base (LB), half-oxidized designated as emeraldine base (EB), and fully oxidized designated as pernigraniline base (PNB). The three base forms LB, EB, and PNB can be protonated to corresponding salt forms designated as LS, ES and PNS. As shown in **Figure 4.6**, the insulating EB form and the highly conducting ES form of PANI can be reversibly converted by doping with acid or dedoping with base. [45]

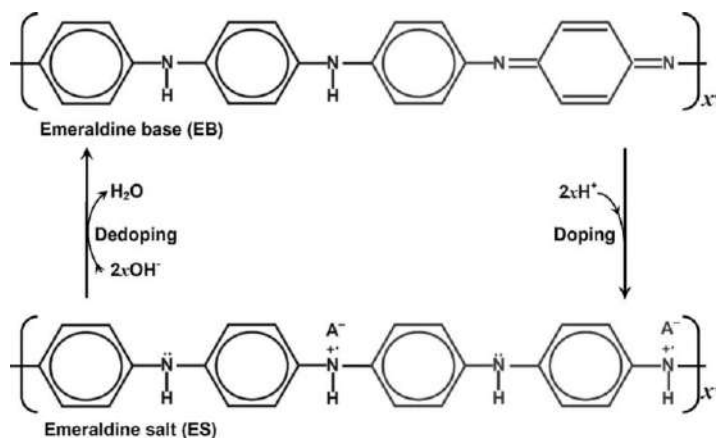


Figure 4.6: Reversible doping/dedoping of polyaniline.

The doping/dedoping mechanism and the controllable electrical conductivity as well as the facile synthesis, the low-cost, the air- and moisture-stability, all have made PANI one of the most used materials for supercapacitor electrodes. PANI has been used to modify various substrates such as carbon, nickel, stainless-steel, or blended with other materials including RuO_2 , carbon, and other CPs for supercapacitor application. [46]

Based on the most reports on PANI supercapacitors, PANI-based electrodes can deliver the charging/discharging process at 0.8 to 1.0 V potential windows. Any PANI-based supercapacitor with a potential window less than 0.6 V is not of practical interest due to the too low resulting energy density.

4.3.3. Hybrid supercapacitors

This third type is the newest type of supercapacitors. It is the most advanced supercapacitor which combines advantages of both EDL capacitance and pseudocapacitance to obtain large enhancement in the overall performance of the supercapacitor. Along with their capability to provide high currents without sacrifices in affordability or cyclic stability, the main property of a hybrid supercapacitor (HSC) is the higher volumetric and gravimetric energy density due to faradaic reaction that occurs on the pseudocapacitive or battery-type electrode. The second electrode is typically made from a carbon-based material that stores electrostatic energy in the double layer on the electrode surface. Examples of HSCs electrodes include $(\text{AC})//\text{Ni}(\text{OH})_2$, $\text{AC}//\text{V}_2\text{O}_5$, $\text{AC}//\text{MnO}_2$, $\text{Li}_4\text{Ti}_5\text{O}_{12}//\text{AC}$, $\text{AC}//\text{LiMn}_2\text{O}_4$... etc.

Currently, the HSC technology is still in its development stage with limited commercialized applications. However, HSCs are gradually being considered as next-generation energy-storage

devices. Some companies like JM Energy, FDK, NCC, and Yunasko have recently started marketing HSC devices. [1, 15, 16, 43, 47-49]

4.4. Electrochemical characterization techniques

In order to evaluate the electrochemical performance of supercapacitors, some fundamental electrochemical measurements should be performed on supercapacitor electrodes, i.e., cyclic voltammetry (CV), galvanostatic charging/discharging (GCD), and electrochemical impedance spectroscopy (EIS).

The measurements are typically conducted on a potentiostat/galvanostat, using either two or three electrode systems. The three-electrode electrochemical cell consists of a working electrode (WE), a counter electrode (CE), and a reference electrode (RE) in an electrolyte solution. Wherein, the voltage is applied between the reference and the working electrode and the corresponding current is measured between the counter and working electrodes. The electrochemical phenomena take place at the working electrode. The reference electrode has a constant potential against which the other potentials are measured, commonly used reference electrodes for aqueous solutions are the saturated calomel electrode (SCE), the silver/silver chloride electrode (Ag/AgCl), the standard hydrogen electrode (SHE), and the normal hydrogen electrode (NHE). The counter electrode is typically made of electrochemically inert materials such as gold and platinum and is used to complete the electrical circuit.

In CV, The electrochemical cell is potentiodynamically controlled by sweeping the potential between two pre-selected limits with a chosen scan rate and measuring the resulting current. The current response is plotted versus the potential to obtain a CV curve. This technique provides useful information on the stable electrochemical window, capacitance, reactions reversibility and cyclability of the active materials or devices. The system kinetics can also be studied by varying the scan rate.

Typical EDLC electrodes will exhibit CV curves approximately rectangular in shape. The pseudocapacitive contribution leads to a deviation from the rectangular shape accompanied with the presence of redox peaks. [10, 50-52]

In addition, GCD measurement technique (also called chronoamperometry) is employed to accurately determine the operating voltage and calculate the specific capacitance (C_{sp}) of a supercapacitor electrode as per the equation 4.4. in the three electrode configuration:

$$C_s = \frac{I \times \Delta t}{m \times \Delta V} \quad (4.4)$$

wherein, I is the discharge current (A), Δt is the discharge time (s), m is the loaded mass of the composite (g), and ΔV is the potential drop upon discharging (excluding the IR drop) (V).

Furthermore, energy and power densities are commonly calculated on total mass or volume basis for fully packaged supercapacitors.

It should be noted that, for non-faradaic electrode materials, the discharge curve is linear, but in contrast, it deviates from linearity for pseudocapacitive electrode materials. [10, 50-52]

On the other hand, electrochemical impedance spectroscopy (EIS) is a powerful tool for studying the frequency behavior and the equivalent series resistance (ESR) of a supercapacitor electrode. EIS measurements are conducted usually at the open-circuit potential (OCP) by imposing a small-amplitude sinusoidal perturbation (5 ~ 10 mV) over a wide range of frequency.

Unless the electrode is purely resistive, impedance is a complex quantity, since the current may show a phase shift ϕ compared to the voltage/time function, thus,

$$Z = Z' + jZ'' \quad (4.5)$$

where Z' and Z'' are respectively the real and imaginary parts of impedance. The plot of $-Z''$ versus Z' is called Nyquist plot. The ESR of the electrode can be obtained from the X-axis intercept of the Nyquist plot.

Due to the complexity of charge storage mechanisms (EDL and pseudocapacitance) and other phenomena arising from different surface morphologies of the studied supercapacitor electrodes, conventional capacitor models such as the Randles circuit are inadequate for modeling supercapacitors. Hence, EIS is a promising technique in extracting model parameters and modeling equivalent circuits. [10, 50, 51]

4.5. Supercapacitors applications



Figure 4.7: Application fields of supercapacitors.

By the 1970s, NEC had successfully marketed its first supercapacitors for CMOS memory power-backup in computers, since then, supercapacitors were moving from niche to widespread applications and more and more companies were investing in the development of supercapacitors including Nippon Chemi-Con, Maxwell Technologies, KEMET Electronics, Panasonic, ELNA, Nichicon, Nissan Motors (Ageo), NESS, Murata, YUNASKO and many others. Globally, the supercapacitor market is growing steadily and rapidly.

Currently, one of the most promising applications of supercapacitors is their use in the transportation field. In hybrid-electric vehicles (HEVs), such as in some *Toyota* and *Honda* HEV models, supercapacitors absorb and store virtually all kinetic energy from the braking systems, power would then be released to help hybrid cars and buses to accelerate and/or assist a faster and reliable engine start-up. Furthermore, many forklift manufacturers employed supercapacitors to provide lift to electric forklifts, easing the stress on the battery pack which runs the forklift. A forklift with a fuel cell powertrain needs supercapacitors to meet the power requirements in lifting operations. In rails, energy is recovered from regenerative braking systems and used for assisting train acceleration and powering

vehicles where wiring systems are not available (**Figure 4.8**). Moreover, supercapacitors are implemented in aircrafts to open emergency doors in the case of power failures as in *Airbus A380*. [6, 10, 13, 53-56]

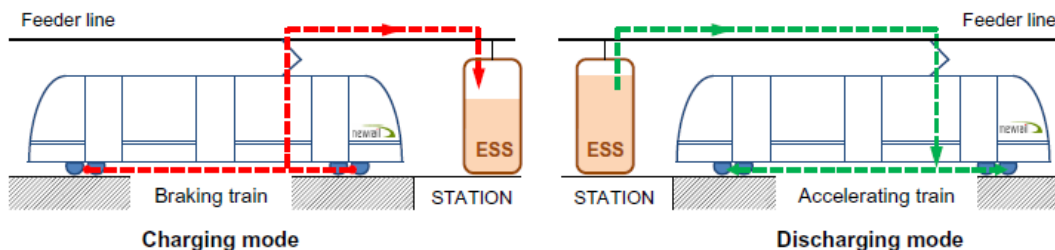


Figure 4.8: Schematic illustration of wayside regenerative braking energy storage system (ESS) for subway trains. [57]

In UPS systems for hospitals, banking centers, data centers, airport control towers, and cell phone towers, supercapacitors, owing to their fast response, serve as an emergency power backup that can rapidly supply power once the primary energy source is failed, so the equipment would be securely shut down or a secondary power source would be initiated [10, 53, 58].

In addition, as affordable energy storage devices, supercapacitors are used to stabilize the output of renewable energy installations, and in general to ensure the reliability and stability of power grids by delivering quick bursts of energy during peak power demands, then quickly recover the lost energy for sustained supply. [10, 53]

4.6. References

- [1]. I. Hadjipaschalis, A. Poullikkas, V. Efthimiou. Overview of current and future energy storage technologies for electric power applications. *Renewable and Sustainable Energy Reviews*. **2009**. 13(6), 1513-22.
- [2]. Z. Wang, P. Tammela, M. Strømme, L. Nyholm. Cellulose-based Supercapacitors: Material and Performance Considerations. *Advanced Energy Materials*. **2017**. 7(18), 1700130.
- [3]. G. Z. Chen. Understanding supercapacitors based on nano-hybrid materials with interfacial conjugation. *Progress in Natural Science: Materials International*. **2013**. 23(3), 245-55.
- [4]. S. K. Kandasamy, K. Kandasamy. Recent Advances in Electrochemical Performances of Graphene Composite (Graphene-Polyaniline/Polypyrrole/Activated Carbon/Carbon Nanotube) Electrode Materials for Supercapacitor: A Review. *Journal of Inorganic and Organometallic Polymers and Materials*. **2018**. 28(3), 559-84.
- [5]. Z. Huang, L. Li, Y. Wang, C. Zhang, *et al.* Polyaniline/graphene nanocomposites towards high-performance supercapacitors: A review. *Composites Communications*. **2018**. 8, 83-91.
- [6]. Z. S. Iro, C. Subramani, S. Dash. A Brief Review on Electrode Materials for Supercapacitor. *Int. J. Electrochem. Sci*. **2016**. 11, 10628-43.

- [7]. G. S. Gudavalli, T. P. Dhakal. Chapter 8 - Simple Parallel-Plate Capacitors to High-Energy Density Future Supercapacitors: A Materials Review, in *Emerging Materials for Energy Conversion and Storage*, ed. by K. Y. Cheong, G. Impellizzeri, M. A. Fraga, Elsevier. **2018**. 247-301.
- [8]. M. Ue. Chemical Capacitors and Quaternary Ammonium Salts. *Electrochemistry*. **2007**. 75(8), 565-72.
- [9]. J. Chung, H. Yong, H. Moon, S. T. Choi, *et al.* Capacitor-Integrated Triboelectric Nanogenerator Based on Metal-Metal Contact for Current Amplification. *Advanced Energy Materials*. **2018**. 8(15), 1703024.
- [10]. A. Yu, V. Chabot, J. Zhang. *Electrochemical supercapacitors for energy storage and delivery: fundamentals and applications*. CRC press. **2013**.
- [11]. J. Both. Electrolytic capacitors, 1890 to 1925: early history and basic principle. *IEEE Electrical Insulation Magazine*. **2015**. 31(1), 22-9.
- [12]. C. Peng, S. Zhang, D. Jewell, G. Z. Chen. Carbon nanotube and conducting polymer composites for supercapacitors. *Progress in Natural Science*. **2008**. 18(7), 777-88.
- [13]. P. SIMON, Y. GOGOTSI. Materials for electrochemical capacitors, in *Nanoscience and Technology*, Co-Published with Macmillan Publishers Ltd, UK. **2009**. 320-9.
- [14]. Z.-S. Wu, X. Shi, H. Xiao, J. Qin, *et al.* Graphene-based Porous Materials for Advanced Energy Storage in Supercapacitors, in *Innovations in Engineered Porous Materials for Energy Generation and Storage Applications*, CRC Press. **2018**. 59-85.
- [15]. J. Libich, J. Máca, J. Vondrák, O. Čech, *et al.* Supercapacitors: Properties and applications. *Journal of Energy Storage*. **2018**. 17, 224-7.
- [16]. A. González, E. Goikolea, J. A. Barrena, R. Mysyk. Review on supercapacitors: Technologies and materials. *Renewable and Sustainable Energy Reviews*. **2016**. 58, 1189-206.
- [17]. W. K. Chee, H. N. Lim, Z. Zainal, N. M. Huang, *et al.* Flexible Graphene-Based Supercapacitors: A Review. *The Journal of Physical Chemistry C*. **2016**. 120(8), 4153-72.
- [18]. M. Endo, T. Takeda, Y. Kim, K. Koshiba, *et al.* High power electric double layer capacitor (EDLC's); from operating principle to pore size control in advanced activated carbons. *Carbon letters*. **2001**. 1(3_4), 117-28.
- [19]. D. J. Bonthuis, S. Gekle, R. R. Netz. Profile of the Static Permittivity Tensor of Water at Interfaces: Consequences for Capacitance, Hydration Interaction and Ion Adsorption. *Langmuir*. **2012**. 28(20), 7679-94.
- [20]. V. S. Bagotsky. *Fundamentals of electrochemistry*. John Wiley & Sons. **2005**. Vol. 44.
- [21]. L. L. Zhang, X. S. Zhao. Carbon-based materials as supercapacitor electrodes. *Chemical Society Reviews*. **2009**. 38(9), 2520-31.
- [22]. P. A. Basnayaka, M. K. Ram, E. K. Stefanakos, A. Kumar. Nanostructured Hybrid Graphene-Conducting Polymers for Electrochemical Supercapacitor Electrodes, in *Handbook of Nanoelectrochemistry: Electrochemical Synthesis Methods, Properties, and Characterization Techniques*, ed. by M. Aliofkhaezaei, A. S. H. Makhlof, Springer International Publishing, Cham. **2016**. 479-501.
- [23]. K. Wang, Y. Song, R. Yan, N. Zhao, *et al.* High capacitive performance of hollow activated carbon fibers derived from willow catkins. *Applied Surface Science*. **2017**. 394, 569-77.
- [24]. G. Wang, L. Zhang, J. Zhang. A review of electrode materials for electrochemical supercapacitors. *Chemical Society Reviews*. **2012**. 41(2), 797-828.
- [25]. J. Chmiola, G. Yushin, Y. Gogotsi, C. Portet, *et al.* Anomalous Increase in Carbon Capacitance at Pore Sizes Less Than 1 Nanometer. *Science*. **2006**. 313(5794), 1760.
- [26]. J. B. Cook, H.-S. Kim, T. C. Lin, C.-H. Lai, *et al.* Pseudocapacitive Charge Storage in Thick Composite MoS₂ Nanocrystal-Based Electrodes. *Advanced Energy Materials*. **2017**. 7(2), 1601283.

- [27]. M. B. Sassin, C. N. Chervin, D. R. Rolison, J. W. Long. Redox Deposition of Nanoscale Metal Oxides on Carbon for Next-Generation Electrochemical Capacitors. *Accounts of Chemical Research*. **2013**. 46(5), 1062-74.
- [28]. Z. Lin, E. Goikolea, A. Balducci, K. Naoi, *et al.* Materials for supercapacitors: When Li-ion battery power is not enough. *Materials Today*. **2018**.
- [29]. B. Chen. Nanomaterials for Green Energy: Next-Generation Energy Conversion and Storage. *IEEE Nanotechnology Magazine*. **2012**. 6(3), 4-7.
- [30]. S. C. Rasmussen. Revisiting the Early History of Synthetic Polymers: Critiques and New Insights. *Ambix*. **2018**. 65(4), 356-72.
- [31]. A. G. MacDiarmid. Nobel Lecture: "Synthetic metals": A novel role for organic polymers. *Reviews of Modern Physics*. **2001**. 73(3), 701-12.
- [32]. M. Ates, T. Karazehir, A. Sezai Sarac. Conducting Polymers and their Applications. *Current Physical Chemistry*. **2012**. 2(3), 224-40.
- [33]. Q. Wu, Y. Xu, Z. Yao, A. Liu, *et al.* Supercapacitors Based on Flexible Graphene/Polyaniline Nanofiber Composite Films. *ACS Nano*. **2010**. 4(4), 1963-70.
- [34]. C. Apetrei, M. D. Maximino, C. S. Martin, P. Alessio. Sensors Based on Conducting Polymers for the Analysis of Food Products, in *Polymers for Food Applications*, ed. by T. J. Gutiérrez, Springer International Publishing, Cham. **2018**. 757-92.
- [35]. H. Shirakawa, E. J. Louis, A. G. MacDiarmid, C. K. Chiang, *et al.* Synthesis of electrically conducting organic polymers: halogen derivatives of polyacetylene, (CH). *Journal of the Chemical Society, Chemical Communications*. **1977**. (16), 578-80.
- [36]. P. K. Upadhyay, A. Ahmad. Chemical synthesis, spectral characterization and stability of some electrically conducting polymers. *Chinese Journal of Polymer Science*. **2010**. 28(2), 191-7.
- [37]. D. E. Labaye, C. Jérôme, V. M. Geskin, P. Louette, *et al.* Full Electrochemical Synthesis of Conducting Polymer Films Chemically Grafted to Conducting Surfaces. *Langmuir*. **2002**. 18(13), 5222-30.
- [38]. J. Berndt, C. Pattyn, S. Hussain, E. Kovacevic. (Invited) Plasma Based Synthesis of Conductive Polymers: Experimental Results and Some Remarks about General Strategies for Plasma Based Polymerization Processes. *ECS Transactions*. **2017**. 77(3), 49-52.
- [39]. T. Uemura, M. Mamada, D. Kumaki, S. Tokito. Synthesis of Semiconducting Polymers through Soluble Precursor Polymers with Thermally Removable Groups and Their Application to Organic Transistors. *ACS Macro Letters*. **2013**. 2(9), 830-3.
- [40]. Y. Wang, Y. Ding, X. Guo, G. Yu. Conductive polymers for stretchable supercapacitors. *Nano Research*. **2019**.
- [41]. Z. Li, X. Jiao, C. Li, D. Chen. Synthesis and application of nanocages in supercapacitors. *Chemical Engineering Journal*. **2018**. 351, 135-56.
- [42]. U. S. Ramelow, R. Wagle. Spectrofluorometric analysis and electrical conductivities of styrene and methyl methacrylate polymers. *Journal of Applied Polymer Science*. **2011**. 119(3), 1469-76.
- [43]. A. Muzaffar, M. B. Ahamed, K. Deshmukh, J. Thirumalai. A review on recent advances in hybrid supercapacitors: Design, fabrication and applications. *Renewable and Sustainable Energy Reviews*. **2019**. 101, 123-45.
- [44]. S. B. Kondawar, P. T. Patil. Conducting Polymer Nanocomposites for Sensor Applications, in *Conducting Polymer Hybrids*, ed. by V. Kumar, S. Kalia, H. C. Swart, Springer International Publishing, Cham. **2017**. 223-67.
- [45]. H. Li, J. Wang, Q. Chu, Z. Wang, *et al.* Theoretical and experimental specific capacitance of polyaniline in sulfuric acid. *Journal of Power Sources*. **2009**. 190(2), 578-86.

- [46]. Q. Meng, K. Cai, Y. Chen, L. Chen. Research progress on conducting polymer based supercapacitor electrode materials. *Nano Energy*. **2017**. 36, 268-85.
- [47]. M. Widmaier. Improvement of hybrid supercapacitors by optimization of electrode design and material properties. Doctoral Thesis. Saarland University. **2018**.
- [48]. E. Lim, C. Jo, J. Lee. A mini review of designed mesoporous materials for energy-storage applications: from electric double-layer capacitors to hybrid supercapacitors. *Nanoscale*. **2016**. 8(15), 7827-33.
- [49]. J. Jiang, G. Tan, S. Peng, D. Qian, *et al.* Electrochemical performance of carbon-coated Li₃V₂(PO₄)₃ as a cathode material for asymmetric hybrid capacitors. *Electrochimica Acta*. **2013**. 107, 59-65.
- [50]. S. Zhang, N. Pan. Supercapacitors Performance Evaluation. *Advanced Energy Materials*. **2015**. 5(6), 1401401-n/a.
- [51]. M. F. El-Kady, Y. Shao, R. B. Kaner. Graphene for batteries, supercapacitors and beyond. *Nature Reviews Materials*. **2016**. 1(7), 16033.
- [52]. N. Elgrishi, K. J. Rountree, B. D. McCarthy, E. S. Rountree, *et al.* A Practical Beginner's Guide to Cyclic Voltammetry. *Journal of Chemical Education*. **2018**. 95(2), 197-206.
- [53]. J. Ernst, R. Lynds, C. Popescu, M. Sutherland. Ultra Capacitors - Capacitor Based Energy Storage, in *Book Ultra Capacitors - Capacitor Based Energy Storage*, ed., ed. by Editor, City. **2017**. Chap. Chapter, 1-6.
- [54]. P. Thounthong, S. Pierfederici, J. Martin, M. Hinaje, *et al.* Modeling and Control of Fuel Cell/Supercapacitor Hybrid Source Based on Differential Flatness Control. *IEEE Transactions on Vehicular Technology*. **2010**. 59(6), 2700-10.
- [55]. P. Simon, Y. Gogotsi. Capacitive Energy Storage in Nanostructured Carbon-Electrolyte Systems. *Accounts of Chemical Research*. **2013**. 46(5), 1094-103.
- [56]. W. Kampeerawat, T. Koseki. A strategy for utilization of regenerative energy in urban railway system by application of smart train scheduling and wayside energy storage system. *Energy Procedia*. **2017**. 138, 795-800.
- [57]. A. González-Gil, R. Palacin, P. Batty. Sustainable urban rail systems: Strategies and technologies for optimal management of regenerative braking energy. *Energy Conversion and Management*. **2013**. 75, 374-88.
- [58]. X. Zhang, H. Xue, Y. Xu, H. Chen, *et al.* An investigation of an uninterruptible power supply (UPS) based on supercapacitor and liquid nitrogen hybridization system. *Energy Conversion and Management*. **2014**. 85, 784-92.

5

Extraction and characterization of cellulose microfibers from Retama raetam stems

5.1. Introduction

Cellulose has attracted much interest among all natural fibers due to its outstanding properties such as renewability, biodegradability, processing flexibility, and high functionality, which make it a promising feedstock for industrial applications in various fields ranging from food industry to printing, cosmetic, oil well drilling, textile, pharmaceutical and biomedical sectors [1-4].

The existence of cellulose as the common material of plant cell walls was first investigated by Braconnot in 1819 [5] and Payen in 1838 [6]. It is a polydispersed linear polymer with a fibrillar structure composed of poly- β (1 \rightarrow 4)-D-glucose units with a syndiotactic configuration [7, 8], found in the cell walls as a network of nanofibrils embedded in a non-cellulosic matrix [9]. Several plants are rich in cellulose, i.e., cotton, wood, bamboo, hemp, flax, and jute ...etc. [10]. In addition, cellulose fibers have been extracted from several sources such as; milkweed stems [11], hop stems [12], rice husk [13], *Cissus quadrangularis* root [14], *dichrostachys cinerea* bark [15] and many more. Although several sources of natural fibers were investigated in detail, the isolation of cellulose fibers from *Retama raetam* has not been reported yet.

Retama raetam, locally known as R'tem, is a wild plant of the Fabaceae family (**Figure 5.1**). It is common to North and East Mediterranean regions [16]. It is largely abundant in arid area; this abundance makes it a good candidate for industrial utilization. Moreover, the *Retama* species contributes to the bio-fertilization of poor grounds because of their aptitude to associate with fixing nitrogen bacteria *Rhizobia* [17]. Therefore, the genus of the *Retama* is included in a re-vegetation program for degraded areas in semi-arid Mediterranean environments [18].

In this research, natural micro-sized cellulose fibers were extracted from *R. raetam* stems using alkali and bleaching treatments, the resultant cellulose microfibers were characterized using FTIR, SEM, XRD and TGA.



Figure 5.1: Photograph of the *Retama raetam* plant.

5.2. Materials and methods

5.2.1. Materials

Stems of *R. raetam* subject of this study were collected in Ouargla, Algeria, in 2015. Acetone, ethanol, sodium hydroxide, and hydrogen peroxide were purchased from Sigma–Aldrich (Germany) and were used without further purification.

5.2.2. Preparation of samples

Adult stems were cleaned with water and air dried, broken to the size of about 1 cm long and 1 mm width, grinded into powder with a Retsch SM100 Comfort cutting mill (Retsch GmbH, Haan, Germany), and sieved using a sieve size of 0.25 mm.

5.2.3. Microfibers extraction

The extraction of cellulose microfibers was performed using classical chemical treatments with adaptations in dewaxing, alkali and bleaching treatment processes. The totally chlorine-free extraction procedure can be described as follows:

Dewaxing

About 20g of powdered stems were first dewaxed in a Soxhlet reflux with a 2:1 (v/v) mixture of acetone/ethanol at 63 °C for 7 h. The main purpose of this step is to remove off waxes and extractives. The sample was then placed in a Buckner funnel and vacuum dried at room temperature for 3 h to remove traces of residual solvents.

Alkali treatment

The alkali treatment was performed to purify the cellulose by removing lignin and hemicellulose from *R. raetam* fibers. The extractive-free sample was treated with an alkali solution (7 wt.% NaOH) with a solvent to solid ratio of 10:1 at 80 °C for 3 h under mechanical stirring. This treatment was performed trice, after each treatment the solid was filtered and washed with distilled water until neutral pH.

Bleaching

A subsequent bleaching treatment was carried out to remove residual lignin and whiten the microfibers. The sample was immersed in a hydrogen peroxide solution (11%, v/v), the pH was adjusted to 11 using 7 wt.% NaOH, the system was vigorously stirred for 3 h at 45 °C. For more effective discoloration, the bleaching process was performed twice under the same conditions, after each treatment, the microfibers were filtered and washed with distilled water.

5.2.4. Fourier transform infrared spectroscopy

Fourier Transmission Infra-Red Spectroscopy was used to analyze the chemical changes of the samples and investigate functional groups in the extracted cellulose. The FTIR spectra were recorded on a Cary 660 FTIR Spectrometer (Agilent Technologies, USA) in a wavelength range of 4000–600 cm^{-1} with a resolution of 4 cm^{-1} .

5.2.5. X-ray Diffraction (XRD) Analysis

The crystallinity of cellulose microfibrils was investigated by X-ray diffraction (XRD) analysis, using a powder X-ray diffractometer (D8 Advance A25 Bruker AXS GbmH., Germany) with Cu $K\alpha$ radiation (1.5406 Å) at 40 kV and 25 mA, in the range of $2\theta = 5\text{--}60^\circ$ at a scanning rate of 0.02 $^\circ \text{s}^{-1}$. The crystallinity index (CrI) was calculated according to Segal equation [19]:

$$CrI = 100 \times (I_{200} - I_{am}) / I_{200} \quad (5.1)$$

where I_{200} is the diffraction intensity at $2\theta = 22\text{--}23^\circ$ and I_{am} is the minimum diffraction intensity at $2\theta = 18\text{--}20^\circ$.

The crystallite size was calculated as per the Scherrer equation [20]:

$$L_{h,k,l} = (0.94 \times \lambda) / (\beta \times \cos \theta) \quad (5.2)$$

where λ is the X-rays wavelength, β is the full width at half maximum in radians, and θ is the Bragg angle.

5.2.6. Morphological structure

A scanning electron microscope (SEM) (Quanta 250 FEG, FEI, USA) with an accelerating voltage of 15 kV was used to investigate the microstructure and the surface morphology of the obtained cellulose microfibrils.

5.2.7. Thermogravimetric analysis (TGA)

In order to study the thermal stability of the extracted cellulose microfibrils, thermogravimetric analysis (TGA) was performed using a Mettler Toledo TGA/DSC 3+ instrument. The scan was carried out from 25 to 600 $^\circ\text{C}$ at a heating rate of 10 $^\circ\text{C}/\text{min}$ and under nitrogen atmosphere.

5.3. Results and discussion

5.3.1. Extraction method and cellulose yield

A stepwise totally chlorine-free procedure for the isolation of cellulose microfibrils from *Retama raetam* was proposed based on that adopted by Sun et al. [21] with modifications. These modifications involve increasing sodium hydroxide and hydrogen peroxide concentrations as well as improving treatment time and/or temperature to enhance non-cellulosic components removal. Therefore, the isolation of *R. raetam* cellulose microfibrils was successfully achieved without any additional harsh acid treatments (**Table 5.3**), which makes the suggested extraction process not only eco-friendly and cost-saving, but also yielding cellulose microfibrils of high crystallinity and smaller diameters as further confirmed by XRD and SEM results.

Cellulose microfibrils yield was gravimetrically determined (calculated as the percentage of the extracted cellulose microfibrils over the initial raw sample weight) and was found to be 52.1%. This yield value is higher than that reported in literature for cellulose microfibrils extracted from *Hibiscus sabdariffa* fibers (38.6%) [22] and comparable to yield values of 52, 52 and 55% for cellulose microfibrils extracted from Coconut palm leaf sheath [23], African Napier grass [24] and Palmyra palm fruits [25], respectively.

5.3.2. FT-IR spectroscopic analysis

Infrared spectroscopy is currently one of the most important analytical techniques available to scientists [26]. It presents a relatively easy method of obtaining direct information on chemical changes that occur during chemical treatments [27]. Furthermore, FT-IR analysis was conducted to investigate the presence of different functional groups in the isolated samples. **Figure 5.2** shows the IR spectra of (a) untreated sample, (b) alkali treated sample and (c) bleached cellulose microfibrils. As summarized in **Table 5.1**, the cellulose spectrum is similar to those reported in literature for cellulose fibers [28].

The band at 3332 cm^{-1} relates to the stretching of H-bonded OH groups, and the one at 2901 cm^{-1} to the C–H stretching [29], it is observed that the band around 3332 cm^{-1} is narrower and has a higher intensity for cellulose, which demonstrated that the extracted cellulose contained more –OH groups than in untreated sample [30]. The band at 1644 cm^{-1} is associated with –OH bending of the absorbed water [31]. Typical bands assigned to cellulose at 1159 cm^{-1} and 897 cm^{-1} are due to C–O–C stretching at the b-(1→4)-glycosidic linkages [32]. The presence of these peaks showed the increase in the

5. Extraction and characterization of cellulose microfibrils from *Retama raetam* stems

percentage of cellulosic components after removal of non-cellulosic materials by chemical treatments [33]. The absorption peak at $\sim 1734\text{ cm}^{-1}$ on the spectrum of the untreated sample (a) is attributed to the C=O stretching of the acetyl and uronic ester groups of polysaccharides [8, 34], it is also related to the p-coumeric acids of lignin and/or hemicellulose [31], the absence of this peak after successive chemical treatments indicates the removal of most of lignin and hemicelluloses from the microfibrils. Another indicator of lignin and hemicellulose removal during the chemical treatments is the significant decrease in the intensity of the peak around 1236 cm^{-1} which is related to the $-\text{COO}$ vibration of acetyl groups in hemicellulose and/or the C–O stretching of the aryl group in lignin [25]. Noticeable peaks on spectrum (c) at 1429 cm^{-1} relates to the CH_2 bending and at 1370 cm^{-1} to the O–H bending. The absorbance at $\sim 1316\text{ cm}^{-1}$ is attributed to the C–C and C–O skeletal vibrations [35]. The C–O–C pyranose ring skeletal vibration occurs in 1054 cm^{-1} and 1031 cm^{-1} . [36]

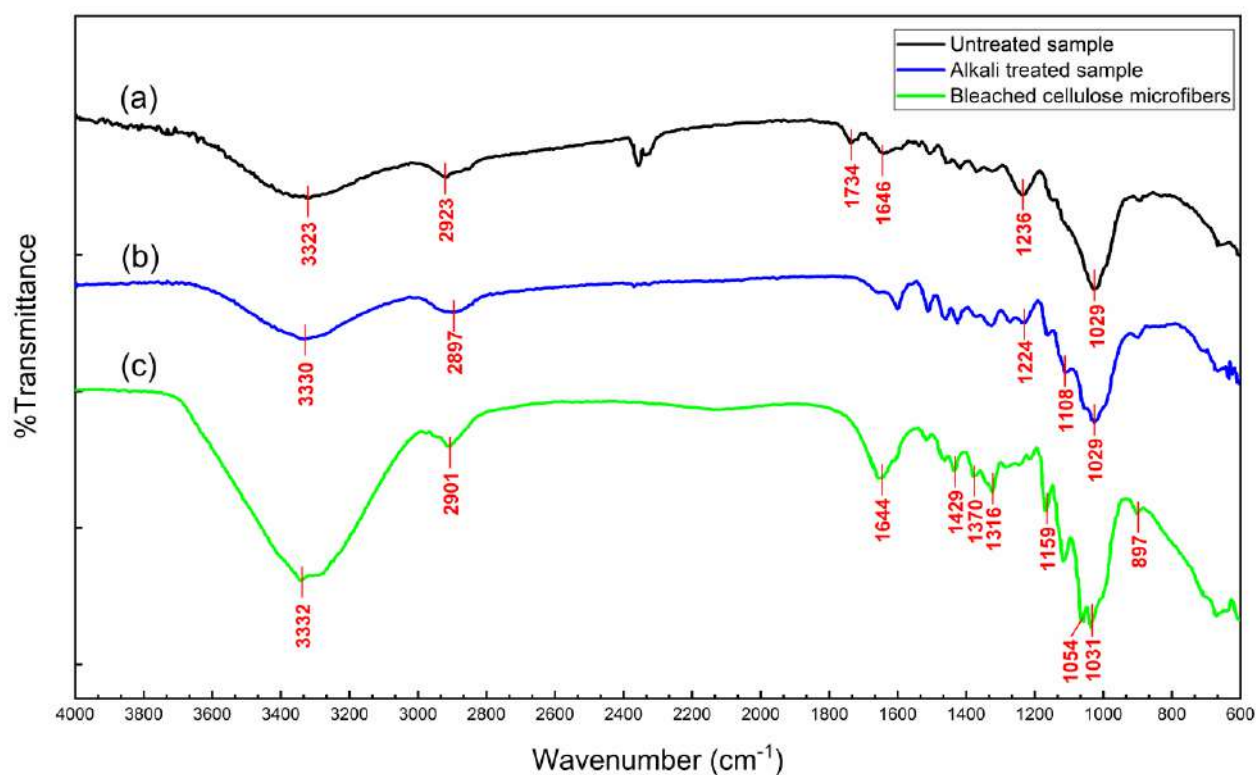


Figure 5.2: FT-IR spectra of (a) untreated sample, (b) alkali treated sample, and (c) bleached cellulose microfibrils.

Table 5.1: The main observed IR bands and their assignments.

Spectra	Wavenumber (cm ⁻¹)	Assignment	Ref.
(a), (b), (c)	876-897	C–O–C stretching at the β-(1→4)-glycosidic linkages	[32]
(a), (b), (c)	1029-1031	C–O–C pyranose ring skeletal vibration	[36]
(b), (c)	1051-1054	C–O–C pyranose ring skeletal vibration	[36]
(a), (b), (c)	1144-1159	C–O–C stretching at the β-(1→4)-glycosidic linkages	[32]
(a), (b)	1224-1236	–COO vibration of acetyl groups / C–O stretching of the aryl group	[25]
(a), (b), (c)	1316-1327	C–C and C–O skeletal vibrations	[35]
(a), (b), (c)	1370-1374	O–H bending	[35]
(a), (b), (c)	1417-1429	CH ₂ bending	[35]
(a), (b), (c)	1644-1646	OH bending of the absorbed water	[31]
(a)	1734	C=O stretching	[34]
(a), (b), (c)	2896-2922	C–H stretching	[29]
(a), (b), (c)	3323-3332	H-bonded OH groups stretching	[29]

5.3.3. X-ray Diffraction measurements

The cellulose amorphous phase is characterized by the low diffracted intensity at a 2θ value of 19.12° , whilst the peaks at 15.14° , 16.25° , 22.75° and 34.39° are attributable to the crystallographic planes of (1-10), (110), (200) and (004), respectively, which are characteristic of the typical cellulose I structure [24, 37]. The crystallinity index (CrI) of the bleached microfibers was determined using equation (5.1) and was found to be 77.8%. Obviously, as illustrated in **Table 5.2**, this CrI value is higher than the value of 73.91% reported by Kale et al. for commercial microcrystalline cellulose from wood pulp [20]. Moreover, it is higher than the CrI values reported in the literature for cellulose

microfibrils isolated using different methods from various sources such as Sugarcane bagasse (50%) [38], Agave fibers (64.4%) [39], mengkuang leaves (69.5%) [40] and Soy hulls (69.6%) [31].

Furthermore, the crystallite size ($L_{h,k,l}$) which was found to be 3.62 nm is comparable to the reported sizes of cellulose crystallites (4 to 7 nm generally) [41]. However, the calculated $L_{h,k,l}$ value is much lower than that reported for hydrolyzed commercial microcrystalline cellulose (10.32 nm). The higher CrI and the lower $L_{h,k,l}$ values suggest that the adopted stepwise chlorine-free extraction treatments were effective in removing most of amorphous domains leading to break the bundles of cellulose fibers to form smaller cellulose crystallites [42, 43].

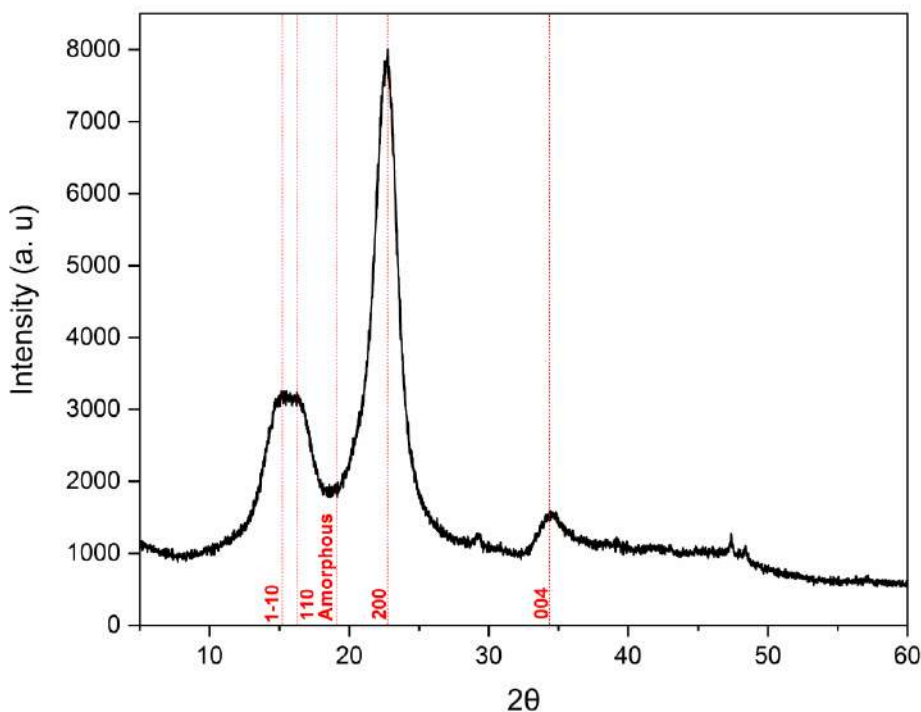


Figure 5.3: XRD diffractogram of extracted *R. raetam* cellulose microfibrils.

Table 5.2: Comparison of the crystallinity indices of cellulose microfibrils from various sources.

Source	Crystallinity index (CrI)	Reference
Coconut palm leaf sheath	47.7%	[23]
Sugarcane bagasse	50%	[38]
Agave fibers	64.4%	[39]
Mengkuang leaves	69.5%	[40]
Soy hulls	69.6%	[31]
Commercial microcrystalline cellulose	73.91%	[20]
Sisal fibers	75% ±1	[44]

Wheat straw	77.8%	[31]
Retama Reatam	77.8%	This work
Hibiscus sabdariffa	78.95%	[22]
Palmyra palm Fruits	81.9%	[25]

5.3.4. Morphological properties of chemically purified cellulose microfibrils

Figure 5.4 shows SEM micrographs of the chemical-purified cellulose microfibrils. After they had been subjected to alkaline solution treatment and bleaching, the cellulose microfibrils were separated into individual micro-sized fibers. These micro-sized cellulose fibers were reported to be composed of strong hydrogen bonding nanofibers [45]. The diameter of the microfibrils is about 6-7 μm but the exact determination of their length is difficult.

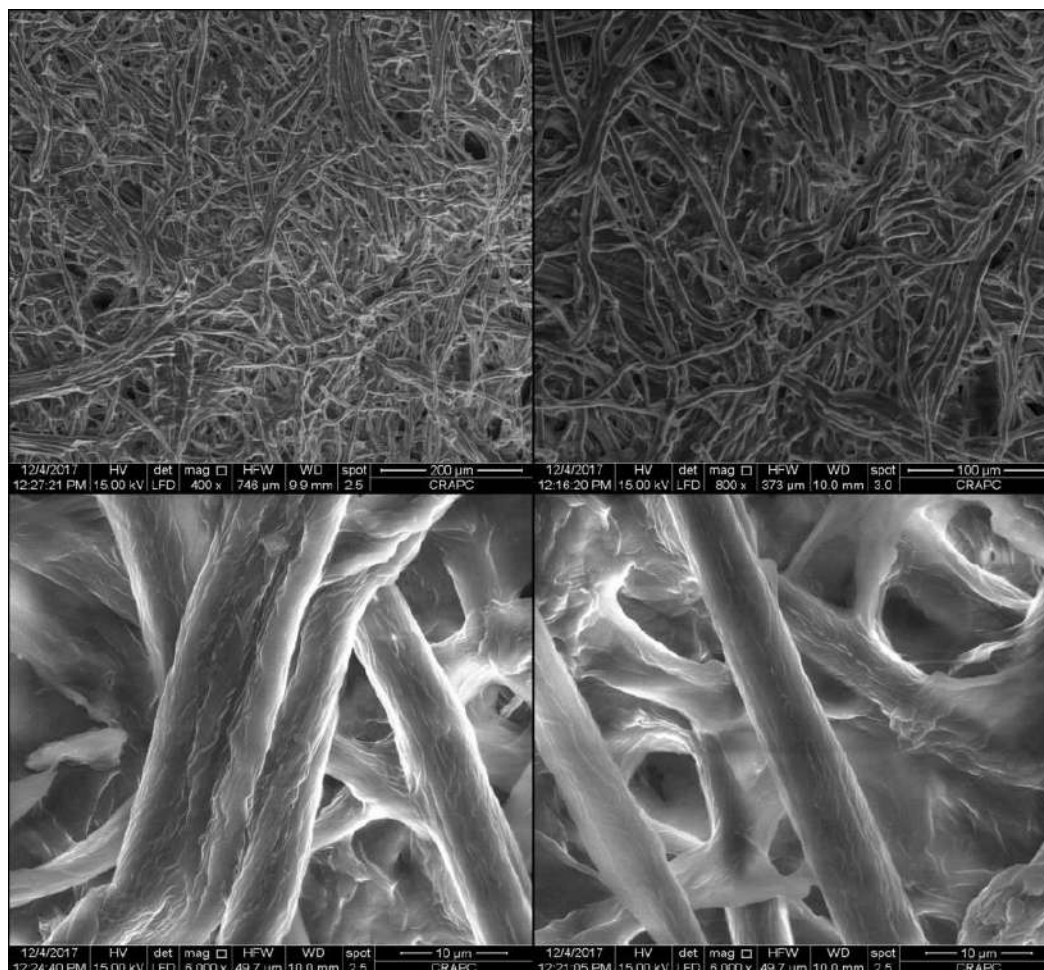


Figure 5.4: SEM images of extracted *R. raetam* cellulose microfibrils.

5. Extraction and characterization of cellulose microfibrils from *Retama raetam* stems

As **Table 5.3** demonstrates, the extracted *R. raetam* cellulose microfibrils are smaller in diameter as compared to those isolated by different extraction methods from various sources such as sisal fibers, agave fibers, coconut palm leaf sheath, soy hull and wheat straw [23, 31, 39, 44]. Moreover, they are comparable to cotton and sugarcane bagasse microfibrils extracted by sulfuric and nitric acid hydrolysis, respectively [38, 46]. This morphology and smaller diameter would enable *R. raetam* cellulose microfibrils to be used for various applications ranging from reinforcing agents in biodegradable composites, to gel forming food and cosmetic additives [39, 47].

Table 5.3: Comparison of the diameters of cellulose microfibrils extracted from various sources by different extraction methods.

Source	Extraction method	diameter (μm)	Ref.
Sisal fibers	Alkali, peroxide and HNO_3/HAc treatments	12.8-31	[44]
Coconut palm leaf sheath	Chlorination, alkali and HNO_3/HAc treatments	10-15	[23]
Soy hull	Alkali treatment and HCl Acid hydrolysis	10-15	[31]
Wheat straw	Alkali treatment and HCl Acid hydrolysis	10-15	[31]
Agave fibers	Chlorination, alkali and HNO_3/HAc treatments	8-14	[39]
Hibiscus sabdariffa	Steam explosion and oxalic acid hydrolysis	10.04	[22]
Sisal fibers	Chlorination and alkali treatments	7-11.2	[44]
Cotton	Sulfuric acid hydrolysis	5-10	[46]
Sugarcane bagasse	Nitric acid hydrolysis	5-10	[38]
Palmyra palm fruit	Chlorination, alkali and HNO_3/HAc treatments	4-11	[25]
Napier grass fibers	Chlorination, alkali and HNO_3/HAc treatments	8.3	[24]
Retama Raetam Stems	Alkali and alkaline peroxide treatments	6-7	This work
Jatropha Curcus L seed shell	Chlorination, alkali and HNO_3/HAc treatments	0.23-1.04	[47]

* HAc: Acetic Acid

5.3.5. Thermal stability

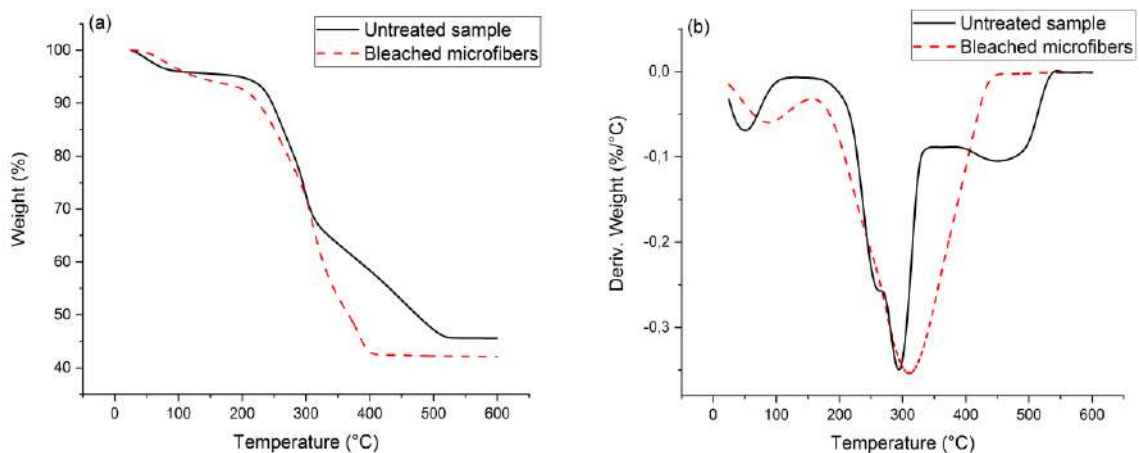


Figure 5.5: TGA (a) and DTG (b) curves of the untreated sample and the bleached cellulose microfibers.

Investigating thermal properties of cellulose microfibers is a key factor for their applicability as reinforcing fillers in biocomposites [33]. **Figure 5.5 (a)** and **(b)** show, respectively, the thermogravimetric analysis (TGA), and the derivative thermogram (DTG) curves for both the raw and bleached samples. TGA curves show an initial weight loss below 155 °C, this initial drop (4.6 % for raw sample and 6.5 % for cellulose microfibers) was due to the evaporation of moisture bounded on the surface of the samples, chemisorbed water bounded inside the samples and/or the compounds of low molecular weight such as extractives presented in the raw sample [33, 48], the presence of the absorbed water was affirmed previously through the FT-IR results. The main broader cellulose thermal degradation (50.84%) occurs over 179 °C and involves synchronous multi-processes such as dehydration, depolymerization, and decomposition of glycosidic units [49]. The raw sample showed separated pyrolysis processes within a wider temperature range, including thermal depolymerization of hemicellulose up to 273 °C, decomposition of cellulose up to 348 °C, and the degradation of lignin up to 536 °C in addition to its simultaneous decomposition with other degradation stages due to its complex structure [48]. DTG curves exhibited maximum decomposition rates at $DTG_{max}=294$ °C and 311 °C for the raw and bleached samples, respectively. A shoulder can be clearly observed at 261 °C on the left side of the main peak of the raw sample DTG curve, which was due to initial decomposition of hemicellulose and non-cellulosic components [49], while the broadening at 245 °C on the

microfibrils DTG curve, could be an indicator of a broad distribution of molecular mass from cellulose or a residual content of hemicellulose which withstood the extracting procedures [44]. Finally, the formation of a charred residue took place (46 % for raw sample and 42 % for cellulose microfibrils). The higher charred residue of the raw sample is due to that fact that the non-cellulosic could induce higher char formation [33]. However, R. raetam cellulose microfibrils presented relatively high char yield when compared to literature (**Table 5.4**), indicating higher non-volatile carbonaceous material generated on pyrolysis [50] and could indicate also a good thermal stability of the extracted cellulose microfibrils [20, 51].

Table 5.4: DTG_{max} and char yields of cellulose microfibrils from different sources.

Samples	T_{max} (°C)	Char (%)	Reference
Date seeds cellulose microfibrils	300	11	[52]
Bamboo cellulose microfibrils	328	13	[53]
Rice hulls microcrystalline cellulose	283	23	[54]
bean hulls microcrystalline cellulose	281	25	[54]
Onion skin cellulose microfibrils	333	26	[55]
Retama Raetam cellulose microfibrils	311	42	This work
Cotton silver microcrystalline cellulose	340	57	[56]
Jute microcrystalline cellulose	280	61	[56]

5.4. Conclusion

The main goal of this work was to investigate the viability of Retama raetam as a novel, renewable and low-cost source of cellulose microfibrils. The successful isolation of cellulose microfibrils was achieved with a yield of 52.1% by stepwise chemical treatments. The FTIR results revealed that the chemical treatments removed most of lignin and hemicellulose from the sample. The extracted cellulose microfibrils were highly crystalline native cellulose I, with a crystallinity of 77.8% and a crystallite size of 3.62 nm. The diameter of the micro-sized fibers was about 6-7 μm. TGA/DTG curves show a maximum decomposition peak at 311°C and a high char yield. These findings proved that R. raetam is a candidate renewable source for the production of cellulose microfibrils and should stimulate further research on the use of these fibers for various applications such as cellulose nanocrystals preparation, reinforcement agent in green biocomposites, and bio-fillers for polymer matrices.

5.5. References

- [1]. L. Zhao, Q. Pang, J. Xie, J. Pei, *et al.* Enzymatic properties of *Thermoanaerobacterium thermosaccharolyticum* β -glucosidase fused to *Clostridium cellulovorans* cellulose binding domain and its application in hydrolysis of microcrystalline cellulose. *BMC Biotechnology*. **2013**. 13(1), 101.
- [2]. M. M. Khatlab, N. A. Abdel-Hady, Y. Dahman. 21 - Cellulose nanocomposites: Opportunities, challenges, and applications, in *Cellulose-Reinforced Nanofibre Composites*, ed. by M. Jawaid, S. Boufi, A. K. H.P.S, Woodhead Publishing. **2017**. 483-516.
- [3]. S. Hokkanen, A. Bhatnagar, M. Sillanpää. A review on modification methods to cellulose-based adsorbents to improve adsorption capacity. *Water Research*. **2016**. 91, 156-73.
- [4]. L. D. Rajapaksha, H. A. D. Saumyadi, A. M. P. B. Samarasekara, D. A. S. Amarasinghe, *et al.* Development of cellulose based light weight polymer composites, in *Book Development of cellulose based light weight polymer composites*, ed., ed. by Editor, City. **2017**. Chap. Chapter, 182-6.
- [5]. H. Braconnot. Sur la Conversion du Corps Ligneux en Gomme, en Sucre, et en un Acide d'une Nature Particulière, par le Moyen de l'Acide Sulfurique; Conversion de la Même Substance Ligneuse en Ulmine par la Potasse. *Annales de Chimie et de Physique*. **1819**. 12, 172-95.
- [6]. A. Payen. Mémoire sur la composition du tissu propre des plantes et du ligneux. *Comptes rendus*. **1838**. 7, 1052-6.
- [7]. S. Naduparambath, T. Jinitha, V. Shaniba, M. Sreejith, *et al.* Isolation and characterisation of cellulose nanocrystals from sago seed shells. *Carbohydrate Polymers*. **2018**. 180, 13-20.
- [8]. M. Vestena, I. P. Gross, C. M. O. Muller, A. T. N. Pires. Isolation of whiskers from natural sources and their dispersed in a non-aqueous medium. *Polímeros*. **2016**. 26, 327-35.
- [9]. R. J. Bernardo, M. F. Gírio, M. R. Łukasik. The Effect of the Chemical Character of Ionic Liquids on Biomass Pre-Treatment and Posterior Enzymatic Hydrolysis. *Molecules*. **2019**. 24(4).
- [10]. M. Li, L.-j. Wang, D. Li, Y.-L. Cheng, *et al.* Preparation and characterization of cellulose nanofibers from de-pectinated sugar beet pulp. *Carbohydrate Polymers*. **2014**. 102, 136-43.
- [11]. N. Reddy, Y. Yang. Extraction and characterization of natural cellulose fibers from common milkweed stems. *Polymer Engineering and Science*. **2009**. 49(11), 2212-7.
- [12]. N. Reddy, Y. Yang. Properties of natural cellulose fibers from hop stems. *Carbohydrate Polymers*. **2009**. 77(4), 898-902.
- [13]. N. Johar, I. Ahmad, A. Dufresne. Extraction, preparation and characterization of cellulose fibres and nanocrystals from rice husk. *Industrial Crops and Products*. **2012**. 37(1), 93-9.
- [14]. S. Indran, R. E. Raj, V. Sreenivasan. Characterization of new natural cellulosic fiber from *Cissus quadrangularis* root. *Carbohydrate Polymers*. **2014**. 110, 423-9.
- [15]. P. Baskaran, M. Kathiresan, P. Sentharamaikkannan, S. Saravanakumar. Characterization of new natural cellulosic fiber from the bark of *dichrostachys cinerea*. *Journal of Natural Fibers*. **2018**. 15(1), 62-8.
- [16]. I. Kacem, H. Majdoub, S. Roudesli. Physicochemical properties of pectin from *retama raetam* obtained using sequential extraction. *Journal of Applied Sciences*. **2008**. 8(9), 1713-9.
- [17]. H. Bokhari-Taieb Brahimi, C. Faugeron, K. Hachem, M. Kaid-Harche, *et al.* Investigation of parietal polysaccharides from *Retama raetam* roots. *African Journal of Biotechnology*. **2015**. 14(29), 2327-34.
- [18]. K. Mechergui, H. Mahmoudi, M. L. Khouja, W. Jaouadi. Factors influencing seed germination of the pastoral plant *Retama raetam* subsp. *bovei* (Fabaceae): interactive effects of fruit morphology, salinity, and osmotic stress. *Biologija*. **2017**. 63(2), 134-51.

- [19]. L. Segal, J. Creely, A. Martin Jr, C. Conrad. An empirical method for estimating the degree of crystallinity of native cellulose using the X-ray diffractometer. *Textile Research Journal*. **1959**. 29(10), 786-94.
- [20]. R. D. Kale, P. S. Bansal, V. G. Gorade. Extraction of Microcrystalline Cellulose from Cotton Sliver and Its Comparison with Commercial Microcrystalline Cellulose. *Journal of Polymers and the Environment*. **2018**. 26(1), 355-64.
- [21]. X.-F. Sun, R.-C. Sun, Y. Su, J.-X. Sun. Comparative Study of Crude and Purified Cellulose from Wheat Straw. *Journal of Agricultural and Food Chemistry*. **2004**. 52(4), 839-47.
- [22]. A. Sonia, K. Priya Dasan. Chemical, morphology and thermal evaluation of cellulose microfibers obtained from Hibiscus sabdariffa. *Carbohydrate Polymers*. **2013**. 92(1), 668-74.
- [23]. C. Uma Maheswari, K. Obi Reddy, E. Muzenda, B. R. Guduri, *et al.* Extraction and characterization of cellulose microfibrils from agricultural residue – Cocos nucifera L. *Biomass and Bioenergy*. **2012**. 46, 555-63.
- [24]. K. O. Reddy, C. U. Maheswari, M. S. Dhlamini, B. M. Mothudi, *et al.* Extraction and characterization of cellulose single fibers from native african napier grass. *Carbohydrate Polymers*. **2018**. 188, 85-91.
- [25]. K. O. Reddy, C. U. Maheswari, M. S. Dhlamini, V. P. Kommula. Exploration on the characteristics of cellulose microfibers from Palmyra palm fruits. *International Journal of Polymer Analysis and Characterization*. **2016**. 21(4), 286-95.
- [26]. M. Fan, D. Dai, B. Huang. Fourier transform infrared spectroscopy for natural fibres, in *Fourier transform-materials analysis*, ed. by S. M. Salih, InTech, Rijeka (Croatia). **2012**. 45-68.
- [27]. R. Maryana, D. Ma'rifatun, A. Wheni, K. Satriyo, *et al.* Alkaline pretreatment on sugarcane bagasse for bioethanol production. *Energy Procedia*. **2014**. 47, 250-4.
- [28]. T. Kondo. The assignment of IR absorption bands due to free hydroxyl groups in cellulose. *Cellulose*. **1997**. 4(4), 281-92.
- [29]. T. Kondo, C. Sawatari. A Fourier transform infra-red spectroscopic analysis of the character of hydrogen bonds in amorphous cellulose. *Polymer*. **1996**. 37(3), 393-9.
- [30]. P. Penjumras, R. B. A. Rahman, R. A. Talib, K. Abdan. Extraction and characterization of cellulose from durian rind. *Agriculture and Agricultural Science Procedia*. **2014**. 2, 237-43.
- [31]. A. Alemdar, M. Sain. Isolation and characterization of nanofibers from agricultural residues–Wheat straw and soy hulls. *Bioresource Technology*. **2008**. 99(6), 1664-71.
- [32]. S. Y. Oh, D. I. Yoo, Y. Shin, H. C. Kim, *et al.* Crystalline structure analysis of cellulose treated with sodium hydroxide and carbon dioxide by means of X-ray diffraction and FTIR spectroscopy. *Carbohydrate Research*. **2005**. 340(15), 2376-91.
- [33]. W. P. Flauzino Neto, H. A. Silvério, N. O. Dantas, D. Pasquini. Extraction and characterization of cellulose nanocrystals from agro-industrial residue–Soy hulls. *Industrial Crops and Products*. **2013**. 42, 480-8.
- [34]. M. Sain, S. Panthapulakkal. Bioprocess preparation of wheat straw fibers and their characterization. *Industrial Crops and Products*. **2006**. 23(1), 1-8.
- [35]. X. Gao, K.-L. Chen, H. Zhang, L.-C. Peng, *et al.* Isolation and characterization of cellulose obtained from bagasse pith by oxygen-containing agents. *BioResources*. **2014**. 9(3), 4094-107.
- [36]. J. X. Sun, X. F. Sun, H. Zhao, R. C. Sun. Isolation and characterization of cellulose from sugarcane bagasse. *Polymer Degradation and Stability*. **2004**. 84(2), 331-9.
- [37]. A. D. French. Idealized powder diffraction patterns for cellulose polymorphs. *Cellulose*. **2014**. 21(2), 885-96.

- [38]. S. Jonjankiat, T. Wittaya, W. Sridach. Improvement of poly (vinyl alcohol) adhesives with cellulose microfibre from sugarcane bagasse. *Iranian Polymer Journal*. **2011**. 20(A.M.A. Archives of Industrial Hygiene and Occupational Medicine4), 305-17.
- [39]. K. O. Reddy, J. Zhang, J. Zhang, A. V. Rajulu. Preparation and properties of self-reinforced cellulose composite films from Agave microfibrils using an ionic liquid. *Carbohydrate Polymers*. **2014**. 114, 537-45.
- [40]. R. M. Sheltami, I. Abdullah, I. Ahmad, A. Dufresne, *et al.* Extraction of cellulose nanocrystals from mengkuang leaves (*Pandanus tectorius*). *Carbohydrate Polymers*. **2012**. 88(2), 772-9.
- [41]. S. Park, J. O. Baker, M. E. Himmel, P. A. Parilla, *et al.* Cellulose crystallinity index: measurement techniques and their impact on interpreting cellulase performance. *Biotechnology for Biofuels*. **2010**. 3(1), 10.
- [42]. Y. Wang, Y. Zhao, Y. Deng. Effect of enzymatic treatment on cotton fiber dissolution in NaOH/urea solution at cold temperature. *Carbohydrate Polymers*. **2008**. 72(1), 178-84.
- [43]. J.-W. Rhim, J. P. Reddy, X. Luo. Isolation of cellulose nanocrystals from onion skin and their utilization for the preparation of agar-based bio-nanocomposites films. *Cellulose*. **2015**. 22(1), 407-20.
- [44]. J. I. Morán, V. A. Alvarez, V. P. Cyras, A. Vázquez. Extraction of cellulose and preparation of nanocellulose from sisal fibers. *Cellulose*. **2008**. 15(1), 149-59.
- [45]. K. Abe, H. Yano. Comparison of the characteristics of cellulose microfibril aggregates of wood, rice straw and potato tuber. *Cellulose*. **2009**. 16(6), 1017-23.
- [46]. C. Anindita, G. K. Kumar, B. D. Sagar, K. Sravanti, *et al.* Pure and copper doped cellulose microfibrils-a case study. *Materials Research Express*. **2018**. 5(10), 105302.
- [47]. M. Puttaswamy, G. Srinikethan, V. Shetty K. Biocomposite composed of PVA reinforced with cellulose microfibrils isolated from biofuel industrial dissipate: *Jatropha Curcus L.* seed shell. *Journal of Environmental Chemical Engineering*. **2017**. 5(2), 1990-7.
- [48]. J. C. C.S, N. George, S. K. Narayanankutty. Isolation and characterization of cellulose nanofibrils from arecanut husk fibre. *Carbohydrate Polymers*. **2016**. 142, 158-66.
- [49]. N. Kasiri, M. Fathi. Production of cellulose nanocrystals from pistachio shells and their application for stabilizing Pickering emulsions. *International Journal of Biological Macromolecules*. **2018**. 106, 1023-31.
- [50]. C. P. Azubuike, A. O. Okhamafe. Physicochemical, spectroscopic and thermal properties of microcrystalline cellulose derived from corn cobs. *International Journal Of Recycling of Organic Waste in Agriculture*. **2012**. 1(1), 9.
- [51]. K. Das, D. Ray, N. R. Bandyopadhyay, T. Ghosh, *et al.* A study of the mechanical, thermal and morphological properties of microcrystalline cellulose particles prepared from cotton slivers using different acid concentrations. *Cellulose*. **2009**. 16(5), 783-93.
- [52]. A. Nabili, A. Fattoum, M.-C. Brochier-Salon, J. Bras, *et al.* Synthesis of cellulose triacetate-I from microfibrillated date seeds cellulose (*Phoenix dactylifera L.*). *Iranian Polymer Journal*. **2017**. 26(2), 137-47.
- [53]. W. Chen, H. Yu, Y. Liu, Y. Hai, *et al.* Isolation and characterization of cellulose nanofibers from four plant cellulose fibers using a chemical-ultrasonic process. *Cellulose*. **2011**. 18(2), 433-42.
- [54]. A. M. Adel, Z. H. Abd El-Wahab, A. A. Ibrahim, M. T. Al-Shemy. Characterization of microcrystalline cellulose prepared from lignocellulosic materials. Part II: Physicochemical properties. *Carbohydrate Polymers*. **2011**. 83(2), 676-87.
- [55]. J. P. Reddy, J.-W. Rhim. Extraction and Characterization of Cellulose Microfibrils from Agricultural Wastes of Onion and Garlic. *Journal of Natural Fibers*. **2018**. 15(4), 465-73.

[56]. K. Das, D. Ray, N. R. Bandyopadhyay, S. Sengupta. Study of the Properties of Microcrystalline Cellulose Particles from Different Renewable Resources by XRD, FTIR, Nanoindentation, TGA and SEM. *Journal of Polymers and the Environment*. **2010**. 18(3), 355-63.

6

Preparation and characterization of cellulose nanowhiskers from pure cotton

6.1. Introduction

Cellulose nanofibers (CNF) and cellulose nanowhiskers (CNW) have attracted considerable attention as green nanofillers in bionanocomposites because of their potential reinforcing capabilities offered by their superior mechanical properties, high aspect ratio, low density, biocompatibility, high strength, and crystallinity [1, 2]. They promise good prospects for various applications, such as polymer composites, flexible substrates for electronics, films, medicines, and functional materials [3]. Recently, there has been a burgeoning interest in extracting nanocellulose from various plants and organisms. Among various sources, such as plants, algae, sea creatures and bacteria, natural cotton fibers hold the highest percentage of cellulose (>95 %) [4, 5]. In nature, cotton fibers with a diameter of several micrometers consist of numerous superfine fibrils in nanometer scale. The nano-architecture of the cellulose promotes isolation of nanowhiskers and nanofibrils [5]. Therefore, CNW can be obtained from cotton fibers using the acid hydrolysis method to remove amorphous phases between crystalline domains [3, 6].

In the present chapter, CNW were prepared from pure cotton by acid hydrolysis and characterized using X-ray diffractometry (XRD) and scanning electron microscopy (SEM).

6.2. Materials and methods

6.2.1. Materials

Pure cotton was obtained from Saffec-Cotiflex (Algeria). sulfuric acid was purchased from Sigma–Aldrich (Germany).

6.2.2. Preparation of cellulose nanowhiskers (CNW)

CNW were prepared from cotton source by acid hydrolysis as reported elsewhere [7, 8] with minor modifications. Typically, 8g of pure cotton was mechanically stirred in a beaker at a ratio of 1:25 (w/v) of aqueous concentrated sulfuric acid (60%, w/w) at 45 °C for 60 min. The reaction was quenched after hydrolysis by adding tenfold volume of chilled water. The hydrolyzed cellulose sample was washed four times by centrifugation at 10000 rpm for 15 min each. The resultant colloidal suspension was dialyzed in distilled water until constant pH and then air dried for further use.

6.2.3. Characterization methods

An X-ray diffractometer (D8 Advance A25, Bruker, Germany) was used to investigate the crystallinity of the prepared cellulose nanofibers. The morphologies of the samples were evaluated by a scanning electron microscopy (JSM-6360, JEOL, Japan) with an accelerating voltage of 15 kV.

6.3. Results and discussion

6.3.1. Diffraction analysis

The effect of acid hydrolysis on the crystallinity of cotton cellulose fibers was examined by X-ray diffractometry. XRD patterns of both raw cotton and CNW are shown in **Figure 6.1**.

Both diffractograms present the same diffraction features of cellulose type I (also referred to as native cellulose), which is corroborated by the fact that there is no doublet in the intensity of the main peak [9, 10]. The patterns exhibit well-defined peaks at 2θ values of 22.58° and 34.46° for the unmodified cotton and 22.88° and 34.20° for the hydrolyzed cotton corresponding, respectively, to the (200) and (004) crystallographic planes of cellulose I. Furthermore, the two peaks around $2\theta \approx 15^\circ$ - 16° are related to the (1-10) and (110) crystallographic planes, respectively [10, 11]. The latter reflections were partially overlapped for raw cotton and became more distinct after hydrolysis process, due to the removal of amorphous materials, mainly, lignin and amorphous cellulose, which cover the two peaks [12].

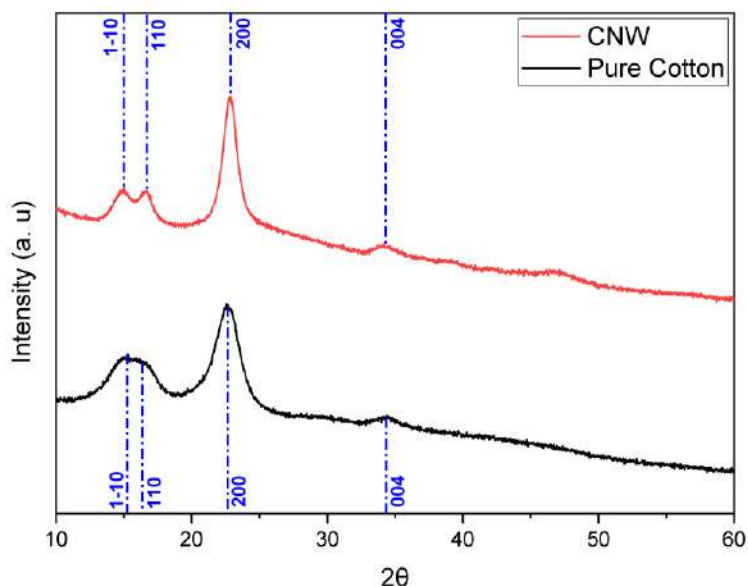


Figure 6.1: XRD data of pure cotton and hydrolyzed cellulose nanowhiskers (CNW).

Moreover, the intensities of the diffraction peaks of CNW were increased significantly compared to those of cotton fibers. This is mainly due to the increase in the crystallinity of the CNW [13]. The crystallinity indices (CrI) of cotton and CNW calculated using Segal equation [14] were 73.12% and 82.04%, respectively, which indicate a crystallinity increase by 12% after acid hydrolysis. The increase in crystallinity of CNW was due to the hydrolytic cleavage of glycosidic bonds in the accessible regions of cellulose fibers, which was accompanied by a significant loss of disordered soluble fraction of the polymer [9, 15].

6.3.2. Morphological analysis

Figure 6.2 (a), (b), and (c) shows the SEM images of raw cotton single fiber and cellulose nanowhiskers, respectively. **Figure 6.2 (a)** clearly exhibits the shape and size of an individual micro-sized fiber in the raw cotton. These raw well-separated fibrils have diameters of about 12-16 μm . Moreover, they exhibit both amorphous and crystalline regions, the latter regions arise from the linear and the conformationally homogeneous nature of the cellulose polymer and the extensive intermolecular hydrogen bonding between adjacent cellulose chains [16].

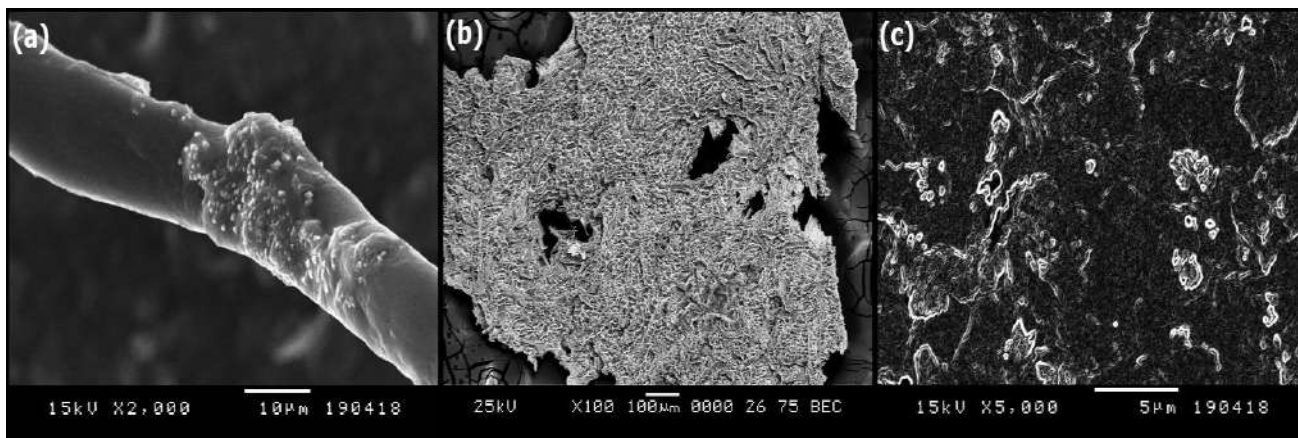


Figure 6.2: SEM micrographs of single cotton fiber (a) and hydrolyzed CNW (b, c).

Though SEM lacks the necessary resolution to allow imaging of individual nanowhiskers, the fibrillar, ribbon-like morphology of the obtained CNW is highly observable in micrographs (b) and (c), with clusters randomly strung together. The ribbons have nanoscale dimensions with varied widths and lengths. An almost similar morphology has been reported by Braun et al. for cotton linter CNW [17]. The remarkable size reduction as well as the higher CrI revealed by XRD data indicate that H_2SO_4 hydrolysis successfully led to the dissolution of amorphous domains, and therefore resulted in the longitudinal cutting of the microfibrils which generate cellulose nanocrystals (CNC) known as nanowhiskers [18].

6.4. Conclusion

Cellulose nanowhiskers (CNW) from pure cotton fibers were successfully prepared by H_2SO_4 hydrolysis without any pulping steps before the acidic treatment. XRD results showed a 12% increase in cellulose crystallinity and no modification in cellulose type after chemical treatment. Moreover, significant morphological differences between pure cotton and CNW were observed by SEM, although the fibrillar morphology was retained.

6.5. References

- [1]. J. Bras, D. Viet, C. Bruzzese, A. Dufresne. Correlation between stiffness of sheets prepared from cellulose whiskers and nanoparticles dimensions. *Carbohydrate Polymers*. **2011**. 84(1), 211-5.
- [2]. R. Dash, T. Elder, A. J. Ragauskas. Grafting of model primary amine compounds to cellulose nanowhiskers through periodate oxidation. *Cellulose*. **2012**. 19(6), 2069-79.
- [3]. Y. Li, G. Li, Y. Zou, Q. Zhou, *et al.* Preparation and characterization of cellulose nanofibers from partly mercerized cotton by mixed acid hydrolysis. *Cellulose*. **2014**. 21(1), 301-9.

- [4]. R. Arjmandi, A. Hassan, M. K. Mohamad Haafiz, Z. Zakaria. Effects of Micro- and Nano-cellulose on Tensile and Morphological Properties of Montmorillonite Nanoclay Reinforced Polylactic Acid Nanocomposites, in *Nanoclay Reinforced Polymer Composites: Natural Fibre/Nanoclay Hybrid Composites*, ed. by M. Jawaid, A. e. K. Qaiss, R. Bouhfid, Springer Singapore, Singapore. **2016**. 103-25.
- [5]. P. Satyamurthy, P. Jain, R. H. Balasubramanya, N. Vigneshwaran. Preparation and characterization of cellulose nanowhiskers from cotton fibres by controlled microbial hydrolysis. *Carbohydrate Polymers*. **2011**. 83(1), 122-9.
- [6]. R. F. Gomes, A. C. N. de Azevedo, A. G. B. Pereira, E. C. Muniz, *et al.* Fast dye removal from water by starch-based nanocomposites. *Journal of Colloid and Interface Science*. **2015**. 454, 200-9.
- [7]. J. P. S. Morais, M. d. F. Rosa, M. d. s. M. de Souza Filho, L. D. Nascimento, *et al.* Extraction and characterization of nanocellulose structures from raw cotton linter. *Carbohydrate Polymers*. **2013**. 91(1), 229-35.
- [8]. W. Zhu, W. Ma, C. Li, J. Pan, *et al.* Well-designed multihollow magnetic imprinted microspheres based on cellulose nanocrystals (CNCs) stabilized Pickering double emulsion polymerization for selective adsorption of bifenthrin. *Chemical Engineering Journal*. **2015**. 276, 249-60.
- [9]. R. D. Kale, P. S. Bansal, V. G. Gorade. Extraction of Microcrystalline Cellulose from Cotton Sliver and Its Comparison with Commercial Microcrystalline Cellulose. *Journal of Polymers and the Environment*. **2018**. 26(1), 355-64.
- [10]. A. D. French. Idealized powder diffraction patterns for cellulose polymorphs. *Cellulose*. **2014**. 21(2), 885-96.
- [11]. K. O. Reddy, C. U. Maheswari, M. S. Dhlamini, B. M. Mothudi, *et al.* Extraction and characterization of cellulose single fibers from native african napier grass. *Carbohydrate Polymers*. **2018**. 188, 85-91.
- [12]. M. A. S. Spinacé, C. S. Lambert, K. K. G. Feroselli, M.-A. De Paoli. Characterization of lignocellulosic curaua fibres. *Carbohydrate Polymers*. **2009**. 77(1), 47-53.
- [13]. A. A. Oun, J.-W. Rhim. Preparation and characterization of sodium carboxymethyl cellulose/cotton linter cellulose nanofibril composite films. *Carbohydrate Polymers*. **2015**. 127, 101-9.
- [14]. L. Segal, J. Creely, A. Martin Jr, C. Conrad. An empirical method for estimating the degree of crystallinity of native cellulose using the X-ray diffractometer. *Textile Research Journal*. **1959**. 29(10), 786-94.
- [15]. J.-W. Rhim, J. P. Reddy, X. Luo. Isolation of cellulose nanocrystals from onion skin and their utilization for the preparation of agar-based bio-nanocomposites films. *Cellulose*. **2015**. 22(1), 407-20.
- [16]. D. Trache, M. H. Hussin, M. K. M. Haafiz, V. K. Thakur. Recent progress in cellulose nanocrystals: sources and production. *Nanoscale*. **2017**. 9(5), 1763-86.
- [17]. B. Braun, J. R. Dorgan, J. P. Chandler. Cellulosic Nanowhiskers. Theory and Application of Light Scattering from Polydisperse Spheroids in the Rayleigh-Gans-Debye Regime. *Biomacromolecules*. **2008**. 9(4), 1255-63.
- [18]. A. de Campos, A. C. Corrêa, P. I. C. Claro, E. de Morais Teixeira, *et al.* Processing, Characterization and Application of Micro and Nanocellulose Based Environmentally Friendly Polymer Composites, in *Sustainable Polymer Composites and Nanocomposites*, ed. by Inamuddin, S. Thomas, R. Kumar Mishra, A. M. Asiri, Springer International Publishing, Cham. **2019**. 1-35.

7

Synthesis of reduced graphene oxide (rGO)

7.1. Introduction

Graphene, a two-dimensional hexagonal lattice of sp^2 -bonded carbon atoms has attracted considerable scientific interest because of its unique properties; a large surface area, excellent mechanical properties, a very high electronic conductivity, an exceptionally high thermal conductivity, as well as many other exceptional properties have made graphene an interesting material for various applications [1].

In wider sense, there are two different approaches for producing graphene; “Top-down” consists of breaking down of graphite into large monolayer or few-layer graphene flakes, using external forces such as mechanical, electrochemical etc., and “Bottom-up” consists of building up graphene using organic precursors [2, 3].

To date, the oxidative-exfoliation is one of the most common top-down methods for the large-scale synthesis, it produces large quantities of graphene oxide (GO), a graphene-like nanosheets which are then reduced to reduced graphene oxide (rGO) [1]. This strategy begins with the oxidation of graphite using a Brodie, Staudenmaier, Hummers, or a modified Hummers method to produce graphite oxide. During the oxidation process which is established in concentrated acids media (sulfuric acid, nitric acid, and/or phosphoric acid) using strong oxidants (potassium permanganate and potassium perchlorate), the attachment of the oxygen-containing functional groups (OFGs) increases the distance

between graphitic layers, hence weakening the van der Waals forces and effectively facilitating the exfoliation of graphite oxide into individual graphene oxide (GO) sheets by ultra-sonication. The GO is then reduced into graphene by means of chemical reduction (by various reducing agents including hydrazine and its derivatives, hydroiodic or ascorbic acid, hydroquinone, potassium and sodium hydroxide, diverse metal hydrides, hydroxylamine, sodium ammonia solution, urea and thiourea), thermal annealing or microwave irradiation. [1, 4-6]

Here, a sonication-assisted oxidative exfoliation of natural graphite was employed to obtain graphene oxide (GO), followed by its reduction with ascorbic acid as a green, inexpensive, and abundant alternative for conventional reducing agents of GO (e.g. hydrazine hydrate). The synthesized rGO was characterized using Raman spectroscopy and X-ray diffractometry.

7.2. Materials and methods

7.2.1. Materials

Graphite fine powder (Extra pure) was purchased from Merck (Germany), potassium permanganate, sodium hydroxide, sulfuric acid, and hydrochloric acid were purchased from Sigma-Aldrich (Germany) and were used as received. L-ascorbic acid was obtained from Eden-Labo (Algeria).

7.2.2. Synthesis of reduced graphene oxide (rGO)

Reduced graphene oxide (rGO) was synthesized by a modified Hummer's method [1]. Initially, 1 g of graphite was dispersed in 50 mL concentrated sulfuric acid (96-98%) with swirling in an ice-water bath. Thereafter, KMnO_4 (3 g) was then slowly added to the reaction mixture maintaining the temperature below 10 °C. The mixture was stirred at room temperature for 30 min, then sonicated for 5 min in a 120W ultrasonic cleaner. The stirring-sonication process was repeated 10 times before adding 200 mL of distilled water to quench the reaction. The mixture was sonicated for an extra 1h, and then the pH was adjusted at ~6 by adding 1M NaOH solution. Subsequently, 100 mL of 1M L-ascorbic acid aqueous solution was added to the exfoliated graphite oxide suspension. The system was then brought to 95 °C and stirred for 1 h to achieve the reduction. GO loses its hydrophilicity during this stage resulting in a black precipitate, which was simply filtered on a Whatman paper, washed with a 1M HCl solution and distilled water until neutral pH, then dried to obtain rGO powder.

7.2.3. Characterization methods

Raman spectra were recorded with a DXR SmartRaman Spectrometer (Thermo Scientific, USA) equipped with 785 nm laser in order to assess the quality of the prepared rGO and determine the microstructure of the samples. An X-ray diffractometer (D8 Advance A25, Bruker, Germany) was used for the XRD measurements.

7.3. Results and discussion

7.3.1. Raman spectroscopy

Raman spectroscopy is a standard non-destructive analysis tool for characterization of various carbon materials [7]. Therefore, it was employed to analyze the structural changes after chemical processing from graphite to reduced graphene oxide (rGO). **Figure 7.1** shows the Raman spectra of bulk graphite powder and rGO. There are two main prominent peaks for both graphite and rGO samples, assigned to G band (1582-1592 cm^{-1}) and D band (1312–1315 cm^{-1}), which represent the in-plane bond-stretching motion of the pairs of C sp^2 atoms (the E_{2g} phonons) and the breathing modes of rings or K-point phonons of A_{1g} symmetry.

Besides G and D bands, there is a weaker intensity band called 2D located at 2636-1645 cm^{-1} . The 2D band is sensitive to the number of graphene layers, namely, a sharp 2D peak of intensity greater than four times of G-band intensity represents a single-layer graphene, while a modulated bump at 2D band shows few-layer graphene [8]. Thus, the synthesized rGO is consistent with few-layer graphene. It is worth mentioning that the 2D band is Raman active for crystalline graphitic materials and it is sensitive to the π band in the graphitic electronic structure [9, 10].

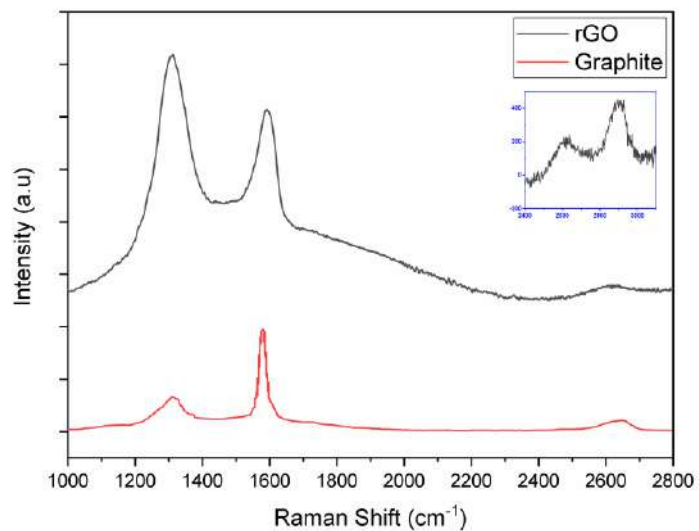
The inset of **Figure 7.1** exhibits the Raman region (2400-3100 cm^{-1}) for rGO, it shows the so-called D + G band at 2908 cm^{-1} which is induced by disorder [9].

Moreover, the intensity ratios I_D/I_G are shown in **Table 7.1**. Obviously, the I_D/I_G ratio for rGO is higher than that of pristine graphite, which is due to the defects and partially disordered crystal structure of rGO, suggesting that the synthesized rGO has a defect content as a result of residual OFGs. [11]

It is worth to note that the rGO spectrum is in accordance with Raman spectra reported in literature for rGO at the same laser excitation [9, 12, 13].

Table 7.1: Intensity ratios I_D/I_G for pristine graphite and rGO.

	Graphite	rGO
I_D	652.87	4612.58
I_G	1953.59	3571.69
I_D/I_G	0.33	1.29

**Figure 7.1:** Raman spectra of pristine graphite and reduced graphene oxide (rGO).

7.3.2. X-ray diffraction analysis

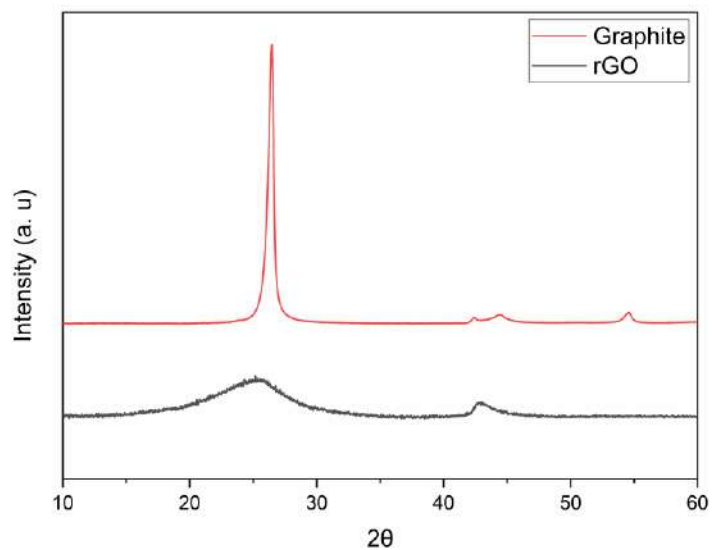
**Figure 7.2:** XRD of pristine graphite and reduced graphene oxide (rGO).

Figure 7.2 represents the XRD patterns of pristine graphite and reduced graphene oxide (rGO). Pristine graphite exhibits a sharp (002) diffraction peak at $2\theta=26.46^\circ$, reflecting an interlayer spacing of 0.336 nm according to Bragg's law. The weaker peaks at 42.40° , 44.46° and 54.56° are assigned to the (100), (101) and (004) planes, respectively.[14, 15]

For rGO, a broad and weak peak centered at $2\theta=25.16^\circ$ assigned to the (002) plane and corresponds to an interlayer spacing of 0.354 nm, which is slightly higher than that of well-ordered pristine graphite. This can be interpreted by the presence of residual OFGs, which had withstood the reduction process of graphene oxide [16]. The broad nature of the peak suggests poorly organized sheets along the stacking direction, suggesting the presence of single to very few layers of graphene [17, 18]. Furthermore, the (100) diffraction peak at $2\theta= 42.86^\circ$ indicates a turbostratic disorder of the graphene sheets [17].

7.4. Conclusion

In summary, reduced graphene oxide (rGO) has been synthesized by a sonication-assisted oxidation of graphite as a modified Hummers method; graphite powder reacted with KMnO_4 in a concentrated H_2SO_4 solution while sonicating for specific periods of time followed by reduction with ascorbic acid as a non-toxic reducing agent. Raman analysis proved the synthesis of few-layer graphene with an $I_D/I_G=1.29$. Moreover, XRD data exhibited the characteristic rGO peaks at $2\theta=25.16^\circ$ and 42.86° and suggested the presence of residual OFGs, which had withstood the reduction process of GO.

7.5. References

- [1]. S. Abdolhosseinzadeh, H. Asgharzadeh, H. Seop Kim. Fast and fully-scalable synthesis of reduced graphene oxide. *Scientific Reports*. **2015**. 5, 10160.
- [2]. X. J. Lee, B. Y. Z. Hiew, K. C. Lai, L. Y. Lee, *et al.* Review on graphene and its derivatives: Synthesis methods and potential industrial implementation. *Journal of the Taiwan Institute of Chemical Engineers*. **2018**.
- [3]. A. P. Kauling, A. T. Seefeldt, D. P. Pisoni, R. C. Pradeep, *et al.* The Worldwide Graphene Flake Production. *Advanced Materials*. **2018**. 30(44), 1803784.
- [4]. L. Chen, J. Lei, F. Wang, G. Wang, *et al.* Facile synthesis of graphene sheets from fluorinated graphite. *RSC Advances*. **2015**. 5(50), 40148-53.
- [5]. E. Abbasi, A. Akbarzadeh, M. Kouhi, M. Milani. Graphene: Synthesis, bio-applications, and properties. *Artificial Cells, Nanomedicine, and Biotechnology*. **2016**. 44(1), 150-6.

- [6]. V. Belessi, D. Petridis, T. Steriotis, K. Spyrou, *et al.* Simultaneous reduction and surface functionalization of graphene oxide for highly conductive and water dispersible graphene derivatives. *SN Applied Sciences*. **2018**. 1(1), 77.
- [7]. S. Urbonaite, L. Hälldahl, G. Svensson. Raman spectroscopy studies of carbide derived carbons. *Carbon*. **2008**. 46(14), 1942-7.
- [8]. T. K. Gupta, B. P. Singh, R. K. Tripathi, S. R. Dhakate, *et al.* Superior nano-mechanical properties of reduced graphene oxide reinforced polyurethane composites. *RSC Advances*. **2015**. 5(22), 16921-30.
- [9]. D. Zhan, Z. Ni, W. Chen, L. Sun, *et al.* Electronic structure of graphite oxide and thermally reduced graphite oxide. *Carbon*. **2011**. 49(4), 1362-6.
- [10]. J. Yan, Z. Fan, T. Wei, W. Qian, *et al.* Fast and reversible surface redox reaction of graphene–MnO₂ composites as supercapacitor electrodes. *Carbon*. **2010**. 48(13), 3825-33.
- [11]. J. Yan, T. Wei, B. Shao, Z. Fan, *et al.* Preparation of a graphene nanosheet/polyaniline composite with high specific capacitance. *Carbon*. **2010**. 48(2), 487-93.
- [12]. H. N. Abdelhamid, H.-F. Wu. Reduced graphene oxide conjugate thymine as a new probe for ultrasensitive and selective fluorometric determination of mercury(II) ions. *Microchimica Acta*. **2015**. 182(9), 1609-17.
- [13]. S. Chinnathambi, G. J. W. Euverink. Polyaniline functionalized electrochemically reduced graphene oxide chemiresistive sensor to monitor the pH in real time during microbial fermentations. *Sensors and Actuators B: Chemical*. **2018**. 264, 38-44.
- [14]. C. Monteserín, M. Blanco, E. Aranzabe, A. Aranzabe, *et al.* Effects of Graphene Oxide and Chemically-Reduced Graphene Oxide on the Dynamic Mechanical Properties of Epoxy Amine Composites. *Polymers*. **2017**. 9(9).
- [15]. Y. Huang, X. Zeng, W. Wang, X. Guo, *et al.* High-resolution flexible temperature sensor based graphite-filled polyethylene oxide and polyvinylidene fluoride composites for body temperature monitoring. *Sensors and Actuators A: Physical*. **2018**. 278, 1-10.
- [16]. J. Li, H. Xie, Y. Li, J. Liu, *et al.* Electrochemical properties of graphene nanosheets/polyaniline nanofibers composites as electrode for supercapacitors. *Journal of Power Sources*. **2011**. 196(24), 10775-81.
- [17]. D. Kale, P. Thakur. Highly efficient photocatalytic degradation and mineralization of 4-nitrophenol by graphene decorated ZnO. *Journal of Porous Materials*. **2015**. 22(3), 797-806.
- [18]. N. A. Kumar, H.-J. Choi, Y. R. Shin, D. W. Chang, *et al.* Polyaniline-Grafted Reduced Graphene Oxide for Efficient Electrochemical Supercapacitors. *ACS Nano*. **2012**. 6(2), 1715-23.

8

Synthesis and characterization of cellulose/polyaniline/rGO composites

8.1. Introduction

Owing to its high theoretical capacitance, easy synthesis, good environmental stability and low cost, polyaniline (PANI) became one of the frequently investigated advanced electrode materials for supercapacitors [1]. However, in addition to their low conductivity, neat PANI electrodes are very brittle and inevitably expands and contracts in the charge/discharge process, resulting in poor cycling stability and low power density. The incorporation of cellulose fibers, PANI, and carbon materials especially conductive and high-surface-area graphene provides an effective approach to solve neat PANI problems, leading to mechanically robust and highly conductive composite electrodes [1-3].

In the present work, conductive PANI-coated cellulose composites hybridized with rGO in different ratios were fabricated by adopting a series of simple operations as depicted in **Figure 8.1**. These operations include, mixing aniline with cellulose microfibrils (CMF) or cellulose nanowhiskers (CNW), in situ polymerization of aniline monomer in the presence of CMF or CNW, and then hybridization of the as prepared composites with different ratios of rGO. The prepared composites were characterized using X-ray diffractometry (XRD), Raman spectroscopy, and scanning electron microscopy (SEM).

8.2. Materials and methods

8.2.1. Materials

Aniline, ammonium persulfate (APS), hydrochloric acid, and acetone were purchased from Sigma–Aldrich (Germany). Reduced graphene oxide (rGO) was synthesized from graphite. Cellulose microfibrils (CMF) and cellulose nanowhiskers (CNW) were previously isolated from *R. raetam* and cotton, respectively.

8.2.2. Preparation of CMF/PANI and CNW/PANI composites

CMF/PANI and CNW/PANI composites were prepared via in situ polymerization of aniline on CMF and CNW, respectively. HCl was used as dopant and ammonium persulfate (APS) as oxidant/initiator, as reported elsewhere with slight modifications [4, 5]. Typically, 2.5g of cellulose fibers (CMF or CNW) thus obtained were dispersed by stirring and sonication in 200 ml of 1M hydrochloric acid solution dissolving aniline (2:1 molar ratio), enabling the aniline solution to fully infiltrate through the cellulose network. Subsequently, 100 ml of 0.25M ammonium persulfate solution in 1M HCl was dropwisely added to the reaction mixture to initialize the oxidative polymerization reaction. The reaction was continued for 4 h at 0-5 °C. Finally, The PANI-coated cellulose was collected as a dark green solid on a filter paper, washed successively with acetone and deionized water to remove the remaining reagents and dried at 60 °C in an air oven for 4 h.

8.2.3. CMF/PANI/rGO composites preparation

CMF/PANI/rGO composites were prepared by solution mixing approach, with dimethylformamide (DMF) being a mutual solvent. In a typical experiment, 1g of the as-prepared PANI-coated cellulose fibers were dispersed in 100 ml of DMF. Separately, rGO dispersions with different rGO loadings were prepared by dispersing a certain amount of rGO into 10 mL of DMF with the aid of ultrasonication for 2 h. CMF/PANI/rGO composites were then prepared by mixing rGO and CMF/PANI dispersions. The mixtures were sonicated for 30 min and stirred for 1 h at room temperature. After filtration, the obtained composites were dried in an air oven at 60 °C for 4 h and are encoded as CMFPG10 and CMFPG20 for 10 and 20 wt.% of rGO, respectively.

8.2.4. CNW/PANI/rGO composites preparation

CNW/PANI/rGO composites were prepared using the same procedure described above. The obtained composites were encoded as CNWPG10, CNWPG20 and CNWPG40 for 10, 20 and 40 wt.% of rGO, respectively.

8.2.5. Characterization methods

An X-ray diffractometer (D8 Advance A25, Bruker, Germany) was used to confirm the formation of PANI coating on CMF and CNW surfaces and verify rGO incorporation. Raman spectra were recorded with a DXR SmartRaman Spectrometer (Thermo Scientific, USA) equipped with 785 nm laser in order to determine the microstructure of the samples and study the chemical changes of the samples. The morphologies of the samples were evaluated by a scanning electron microscope (Quanta 250 FEG, FEI, USA) with an accelerating voltage of 15 kV, and a SEM (JSM-6360, JEOL, Japan) with an accelerating voltage of 15 kV for the CNW sample .

8.3. Results and discussion

8.3.1. Synthesis process

Solution mixing is the most direct and straightforward method for the preparation of graphene-based PANI composites and nanocomposites. During the process, cellulose/PANI and rGO are previously prepared, and then they are mixed under ultrasonication and/or stirring. Firstly, PANI was grown directly on cellulose fibers via a simple in situ polymerization in acidic medium to obtain cellulose/PANI conductive composite. The aniline monomer penetrates into the inner network of cellulose. Meanwhile, the abundant functional hydroxyl groups of cellulose interact with amine groups of aniline to form hydrogen bonds, ensuring the uniform distribution and polymerization of aniline on the surface of cellulose fibers [1]. The interaction between CMF or CNW and aniline monomer has a physical nature without chemical grafting involvement [6]. The in-situ polymerization of aniline was initiated by dropwisely adding 0.25M APS solution dissolved in 1M HCl at low temperature. The aniline monomer which was soaked on the surface of cellulose fibers acts as the seed template for the growth of PANI and led to the homogeneous deposition of polyaniline on the fibers network [1]. The resulting cellulose/PANI precipitate has an obvious dark green color, suggesting the successful incorporation of PANI in its emeraldine salt form on the cellulose scaffold. Finally, cellulose/PANI/rGO composites were prepared by solution mixing, with DMF being a mutual solvent.

The good dispersity of both cellulose/PANI and rGO depends on their compatibility with the mutual solvent [7].

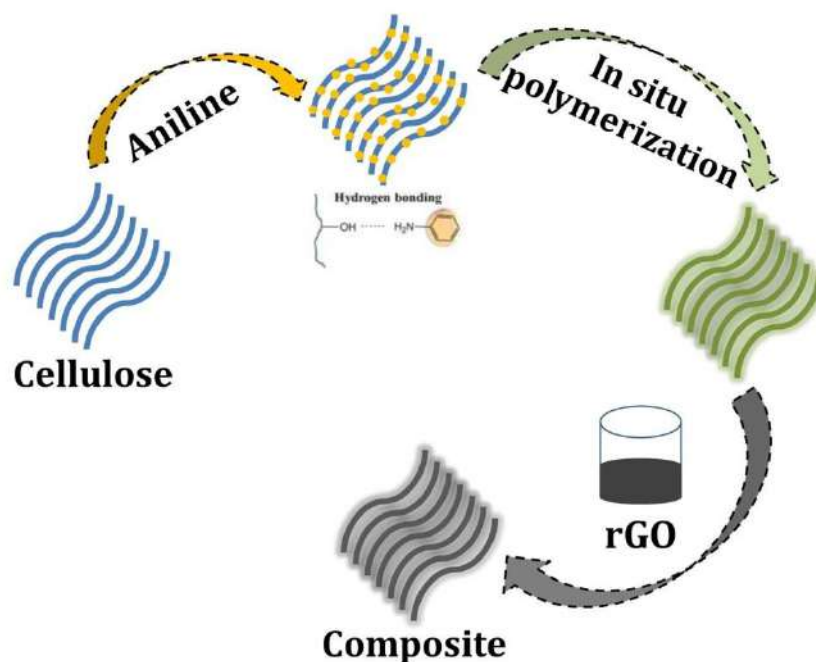


Figure 8.1: Representative schematic of the composites preparation process.

8.3.2. Structural and Morphological analysis

In order to achieve a better understanding on structural changes of the products obtained after each fabrication step, XRD studies on the cellulose fibers, PANI-coated fibers and cellulose/PANI/rGO composites have been conducted and their corresponding patterns are given in **Figure 8.2**.

In **Figure 8.2 (a)**, the CMF peaks at 15.14° , 16.25° , 22.75° and 34.39° are ascribed to the crystallographic planes of (1-10), (110), (200) and (004), respectively, which are characteristic of the typical cellulose I structure [8, 9]. XRD pattern of the CMF/PANI composite reveals that PANI was successfully coated on the surfaces of cellulose microfibrils. The characteristic cellulose peaks have been dramatically weakened due to the amorphous nature of the PANI coating, which partly hindered the crystalline structure of the microfibrils [10, 11]. The newly appeared peak broadening at $2\theta=25.24^\circ$ is assigned to the periodicity perpendicular to the PANI chain [12], other PANI peaks of (011) and (020) planes appear around 15° and 22° overlapping with weak CMF peaks [13]. CMFPGs composites show similar XRD patterns to CMF/PANI with a new weak reflection at 43.02° attributed to the (100) crystal plane of graphene [14], which indicates the incorporation of rGO in the composites.

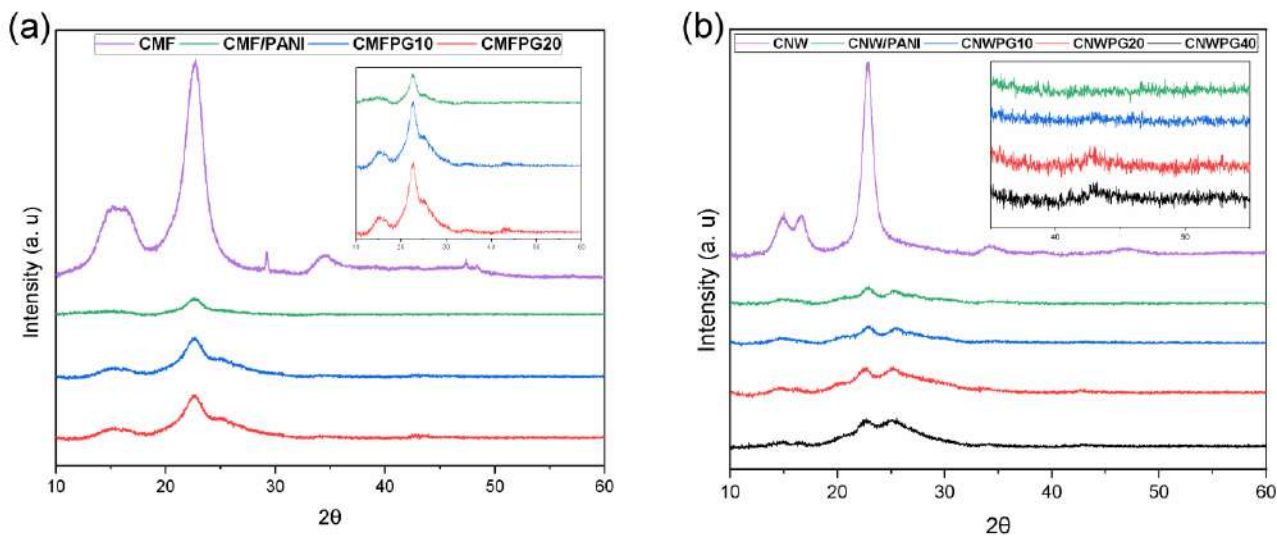


Figure 8.2: XRD data of (a) CMF, CMF/PANI and CMFPGs composites, (b) CNW, CNW/PANI and CNWPGs composites.

On the other hand, The four peaks of CNW pattern centered at 15.02° , 16.62° , 22.88° and 34.20° are related to the characteristic crystallographic planes of cellulose I, namely, (1-10), (110), (200) and (004), respectively [8, 9]. While the CNW/PANI composite exhibits three peaks located at 14.38° , 22.36° , and 25.10° , corresponding to (011), (020), and (200) planes of pure PANI in its emeraldine salt state [15], where the peak at $2\theta=22.36^\circ$ is caused by the layers of polymer chains alternating distance, and the peaks at $2\theta=14.38^\circ$ and 25.10° are attributed to the periodicity perpendicular and parallel to the polymer chain, respectively [12]. The presence of these peaks as well as the disappearance of cellulose-related peaks confirm the successful coating of conductive PANI on the surfaces of CNW. The XRD data of CNWPGs composites present crystalline peaks almost similar to those obtained from CNW/PANI. In addition, a new weak reflection at 42.8° ascribed the (100) crystal plane of graphene can be observed [14]. It indicates that rGO was successfully incorporated in the composites. Whilst, the peak attributed to graphene's (002) plane is overlapped with PANI peaks around $2\theta=25^\circ$ [15].

Obviously, the intensities of the graphene-related peaks of (002) and (100) planes increased by increasing rGO ratio in CMFPGs and CNWPGs composites, suggesting more agglomeration of graphene sheets [16]. The latter observation was further confirmed by electrochemical measurements.

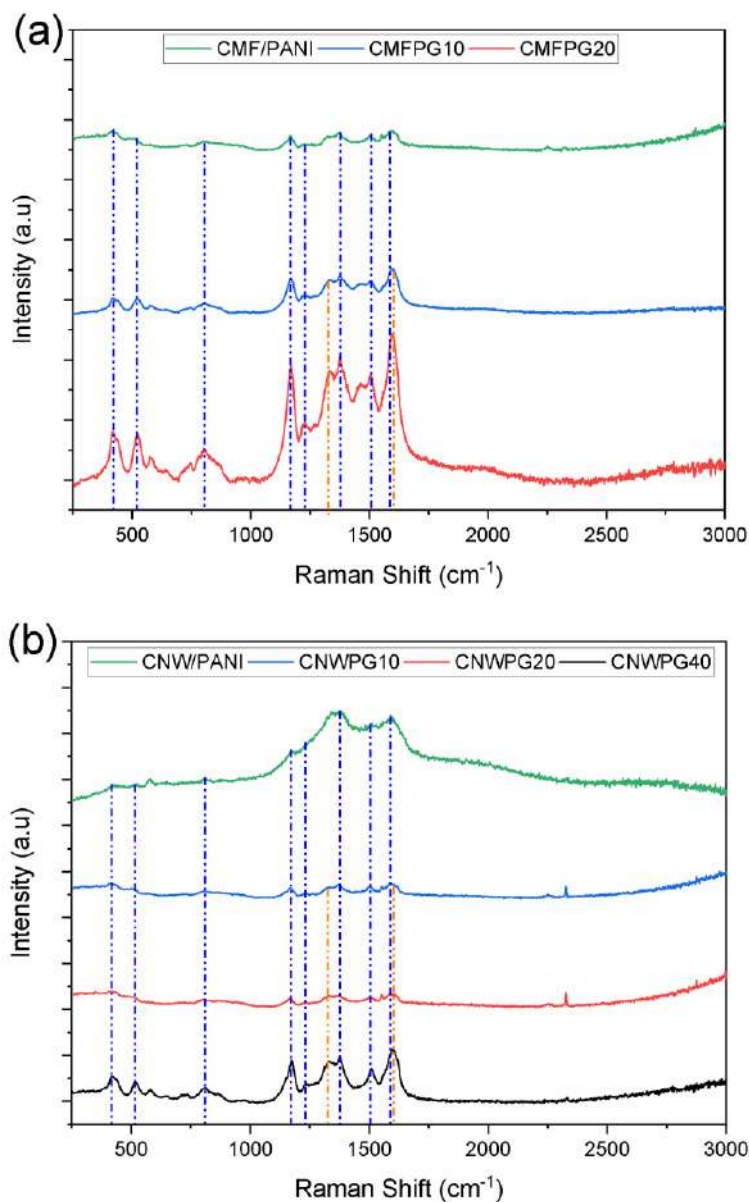


Figure 8.3: Raman spectra of (a) CMF, CMF/PANI and CMFPGs composites, (b) CNW, CNW/PANI and CNWPGs composites.

The Raman spectra of PANI-coated cellulose and cellulose/PANI/rGO composites are shown in **Figure 8.3** and the results are summarized in **Table 8.1**.

The bands around 420, 515 and 807 cm^{-1} correspond to the out-of-plane C–H wag of quinonoid ring, the out-of-plane C–N–C torsion and out-of-plane C–H bending in the quinonoid rings, respectively [18 ,17]. The bands around 1170 and 1226 cm^{-1} are attributed to the in-plane C–H

bendings of benzenoid and quinonoid rings, respectively [18, 19]. The band at $\sim 1376\text{ cm}^{-1}$ is assigned to the C-N^{+} stretching [19, 20]. The band at $\sim 1508\text{ cm}^{-1}$ corresponds to the $\text{C}=\text{C}$ stretching vibrations of quinonoid rings [21, 22]. Moreover, the bands at 1589 and 1592 cm^{-1} in CMF/PANI and CNW/PANI curves are attributed to the C-C stretching of the benzenoid rings [23, 17]. These results agree with the characteristic peaks of PANI as the cellulose-related bands cannot be distinguished. Apart from the characteristic peaks of PANI, the bands around ($1319\text{-}1330\text{ cm}^{-1}$) and ($1591\text{-}1598\text{ cm}^{-1}$) correspond to the characteristic bands D and G of graphene also appear in the Raman spectra of CMFPGs and CNWPGs, revealing the presence of PANI and rGO in the composites [18]. The intensities of the latter peaks increased by increasing rGO ratio in the composites, and the G band is significantly apparent in CMFPG20 and CNWPG40, suggesting more agglomeration of graphene sheets. These results are consistent with the XRD results.

Table 8.1: The main observed Raman bands and their assignments.

Wavenumber cm^{-1}	Assignment	Ref.
414-428	Out-of-plane C-H wag of quinonoid rings.	[17]
511-520	Out-of-plane C-N-C torsion.	[17]
800-812	Out-of-plane C-H bending in the quinonoid rings	[18, 17]
1167-1175	In-plane C-H bending deformation in the benzenoid rings.	[18, 19]
1226-1233	In-plane C-H bendings of quinonoid rings.	[19]
1319-1330	Breathing modes of rings or K-point phonons of A_{1g} symmetry.	[24]
1374-1379	C-N^{+} stretching vibration	[19, 20]
1505-1513	$\text{C}=\text{C}$ stretching vibrations of quinonoid rings.	[21, 22]
1589, 1592	C-C stretching of the benzenoid rings.	[17, 23]
1591-1598	In-plane bond-stretching motion of the pairs of C sp^2 atoms (the E_{2g} phonons).	[24]

SEM micrographs of CMF/PANI, CNW/PANI, CMFPGs, and CNWPGs composites are shown in **Figure 8.4**. **Figure 8.4 (a)** and **(d)** reveals that both CMF and CNW present a typical fibrous/whisker morphology as discussed previously in chapters 5 and 6. The micrographs of CMF/PANI and CNW/PANI composites in **Figures 8.4 (b)** and **(e)** verified that cellulose was fully covered with polyaniline, forming mechanically robust and conductive backbones. However, while the former composite retains the fibrous structure, the latter exhibits a compact sheet-like to granular shaped accumulation and the fibrous structure was no longer observed at the available magnification. The aggregation of the PANI-coated CMF and CNW was mainly due to the strong hydrogen bonding

between sequentially formed PANI layers on adjacent microfibers or whisker clusters, thus bounding them and reinforcing the composites structures [5, 25]. The densely packed structure leads to a continuous conducting pathway responsible for low resistance against electron transfer in the composites [26]. Moreover, the micrographs 8.4 (c) and (f) of CMFPG10 and CNWPG10, respectively, show that the composites maintained their previous morphologies even after the rGO incorporation, furthermore, the brighter edges in the inserted (f) offset are due to the stronger electron scattering property of rGO [27].

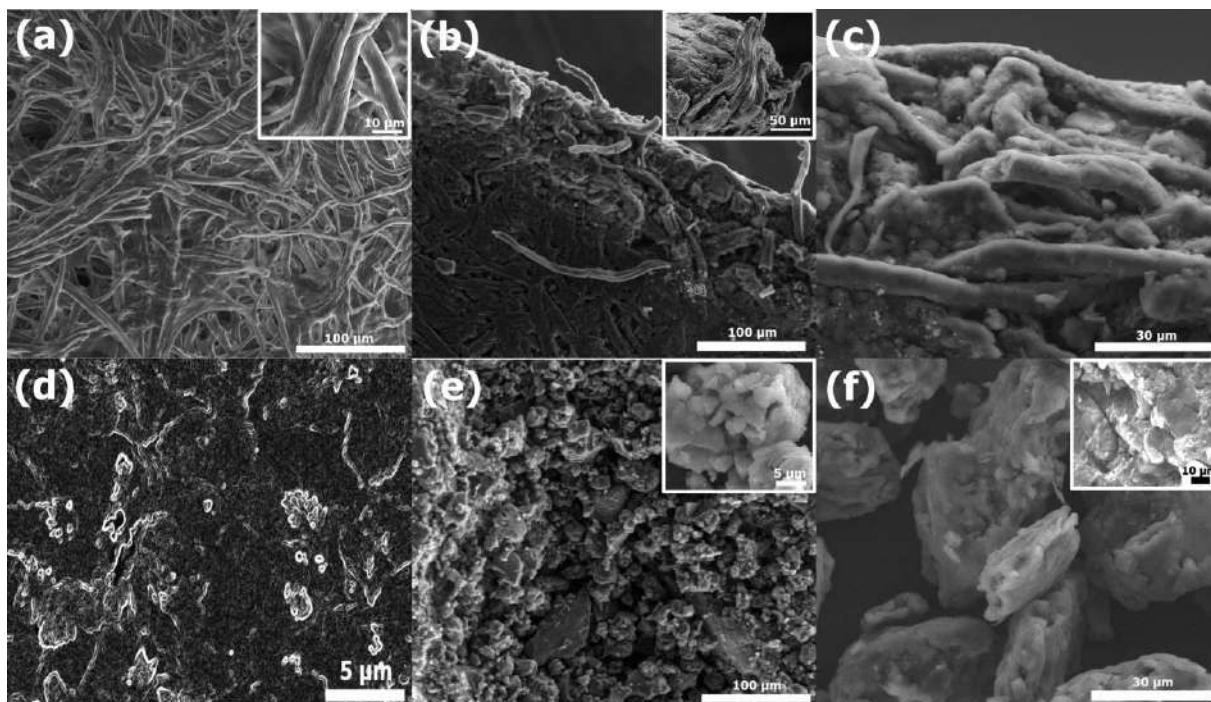


Figure 8.4: SEM micrographs of CMF (a), CMF/PANI (b), CMFPG10 (c), CNW (d), CNW/PANI (e), and CNWPG10 (f).

8.4. Conclusion

In this chapter, cellulose/PANI composites were prepared via in situ polymerization of aniline monomer on cellulose microfibers (CMF) and cellulose nanowhiskers (CNW), followed by hybridization of the as prepared composites with different ratios of rGO.

XRD and Raman data verified that PANI was successfully coated on the surfaces of CMF and CNW and indicated the incorporation of rGO in the composites. Moreover, the data suggested more agglomeration of graphene sheets by increasing rGO ratio in CMFPGs and CNWPGs composites. SEM

images revealed that the CMF/PANI composite retains the fibrous structure, while the CNW/PANI exhibits a compact sheet-like to granular shaped accumulation and the fibrous structure was no longer observed.

8.5. References

- [1]. Z. Zhou, Y. Yang, Y. Han, Q. Guo, *et al.* In situ doping enables the multifunctionalization of templately synthesized polyaniline@cellulose nanocomposites. *Carbohydrate Polymers*. **2017**. 177, 241-8.
- [2]. D. Müller, J. S. Mandelli, J. A. Marins, B. G. Soares, *et al.* Electrically conducting nanocomposites: preparation and properties of polyaniline (PANI)-coated bacterial cellulose nanofibers (BC). *Cellulose*. **2012**. 19(5), 1645-54.
- [3]. L. Wang, X. Lu, S. Lei, Y. Song. Graphene-based polyaniline nanocomposites: preparation, properties and applications. *Journal of Materials Chemistry A*. **2014**. 2(13), 4491-509.
- [4]. Z. Shi, S. Zang, F. Jiang, L. Huang, *et al.* In situ nano-assembly of bacterial cellulose-polyaniline composites. *RSC Advances*. **2012**. 2(3), 1040-6.
- [5]. Z.-l. Mo, Z.-l. Zhao, H. Chen, G.-p. Niu, *et al.* Heterogeneous preparation of cellulose-polyaniline conductive composites with cellulose activated by acids and its electrical properties. *Carbohydrate Polymers*. **2009**. 75(4), 660-4.
- [6]. S. Liu, T. Yu, Y. Wu, W. Li, *et al.* Evolution of cellulose into flexible conductive green electronics: a smart strategy to fabricate sustainable electrodes for supercapacitors. *RSC Advances*. **2014**. 4(64), 34134-43.
- [7]. X. Huang, X. Qi, F. Boey, H. Zhang. Graphene-based composites. *Chemical Society Reviews*. **2012**. 41(2), 666-86.
- [8]. A. D. French. Idealized powder diffraction patterns for cellulose polymorphs. *Cellulose*. **2014**. 21(2), 885-96.
- [9]. K. O. Reddy, C. U. Maheswari, M. S. Dhlamini, B. M. Mothudi, *et al.* Extraction and characterization of cellulose single fibers from native african napier grass. *Carbohydrate Polymers*. **2018**. 188, 85-91.
- [10]. R. Liu, L. Ma, S. Huang, J. Mei, *et al.* Large areal mass, flexible and freestanding polyaniline/bacterial cellulose/graphene film for high-performance supercapacitors. *RSC Advances*. **2016**. 6(109), 107426-32.
- [11]. M. Ramamoorthy, S. Rajiv. In-vitro release of fragrant l-carvone from electrospun poly(ϵ -caprolactone)/wheat cellulose scaffold. *Carbohydrate Polymers*. **2015**. 133, 328-36.
- [12]. D. Gui, C. Liu, F. Chen, J. Liu. Preparation of polyaniline/graphene oxide nanocomposite for the application of supercapacitor. *Applied Surface Science*. **2014**. 307(Supplement C), 172-7.
- [13]. J. A. Marins, B. G. Soares, K. Dahmouche, S. J. L. Ribeiro, *et al.* Structure and properties of conducting bacterial cellulose-polyaniline nanocomposites. *Cellulose*. **2011**. 18(5), 1285-94.
- [14]. Z. Sun, Q. Fu, H. Li, K. Li. PREPARATION AND ELECTROCHEMICAL CAPACITIVE BEHAVIOR OF GRAPHENE BY MICROWAVE ASSISTED THERMAL REDUCTION OF GRAPHITE OXIDE IN HYDRAZINE HYDRATE. *Nano*. **2014**. 09(06), 1450066.
- [15]. W. He, W. Zhang, Y. Li, X. Jing. A high concentration graphene dispersion stabilized by polyaniline nanofibers. *Synthetic Metals*. **2012**. 162(13), 1107-13.

- [16]. L. Tang, Z. Yang, F. Duan, M. Chen. Fabrication of graphene sheets/polyaniline nanofibers composite for enhanced supercapacitor properties. *Colloids and Surfaces A: Physicochemical and Engineering Aspects*. **2017**. 520, 184-92.
- [17]. J. Luo, W. Zhong, Y. Zou, C. Xiong, *et al.* Preparation of morphology-controllable polyaniline and polyaniline/graphene hydrogels for high performance binder-free supercapacitor electrodes. *Journal of Power Sources*. **2016**. 319, 73-81.
- [18]. N. Chen, Y. Ren, P. Kong, L. Tan, *et al.* In situ one-pot preparation of reduced graphene oxide/polyaniline composite for high-performance electrochemical capacitors. *Applied Surface Science*. **2017**. 392, 71-9.
- [19]. B. Ma, X. Zhou, H. Bao, X. Li, *et al.* Hierarchical composites of sulfonated graphene-supported vertically aligned polyaniline nanorods for high-performance supercapacitors. *Journal of Power Sources*. **2012**. 215, 36-42.
- [20]. S. Chinnathambi, G. J. W. Euverink. Polyaniline functionalized electrochemically reduced graphene oxide chemiresistive sensor to monitor the pH in real time during microbial fermentations. *Sensors and Actuators B: Chemical*. **2018**. 264, 38-44.
- [21]. B. Rajagopalan, S. H. Hur, J. S. Chung. Surfactant-treated graphene covered polyaniline nanowires for supercapacitor electrode. *Nanoscale Research Letters*. **2015**. 10(1), 183.
- [22]. T. Fan, S. Tong, W. Zeng, Q. Niu, *et al.* Self-assembling sulfonated graphene/polyaniline nanocomposite paper for high performance supercapacitor. *Synthetic Metals*. **2015**. 199, 79-86.
- [23]. A. Sayah, F. Habelhames, A. Bahloul, B. Nessark, *et al.* Electrochemical synthesis of polyaniline-exfoliated graphene composite films and their capacitance properties. *Journal of Electroanalytical Chemistry*. **2018**. 818, 26-34.
- [24]. T. K. Gupta, B. P. Singh, R. K. Tripathi, S. R. Dhakate, *et al.* Superior nano-mechanical properties of reduced graphene oxide reinforced polyurethane composites. *RSC Advances*. **2015**. 5(22), 16921-30.
- [25]. C. Long, D. Qi, T. Wei, J. Yan, *et al.* Nitrogen-Doped Carbon Networks for High Energy Density Supercapacitors Derived from Polyaniline Coated Bacterial Cellulose. *Advanced Functional Materials*. **2014**. 24(25), 3953-61.
- [26]. M. Mashkour, M. Rahimnejad, M. Mashkour. Bacterial cellulose-polyaniline nano-biocomposite: A porous media hydrogel bioanode enhancing the performance of microbial fuel cell. *Journal of Power Sources*. **2016**. 325, 322-8.
- [27]. W. Ouyang, J. Sun, J. Memon, C. Wang, *et al.* Scalable preparation of three-dimensional porous structures of reduced graphene oxide/cellulose composites and their application in supercapacitors. *Carbon*. **2013**. 62, 501-9.

9

Preparation of supercapacitor electrodes and their electrochemical characterization

9.1. Introduction

Supercapacitors, also known as ultracapacitors, are considered as one of the most promising candidates to meet sustainable development requirements in the energy sector, owing to their advantages such as high capacitance, fast charging/discharging rates, long cycle life, and low processing costs. A supercapacitor consists of two electrodes, an electrolyte, and a separator, where electrodes are immersed in the electrolyte. Electrode materials play a crucial role in the development of supercapacitors, thus significant research efforts have been devoted to the development of inexpensive and environmentally friendly electrode materials for supercapacitors [1].

The performance of supercapacitor electrodes can be characterized using a series of key parameters, including the specific capacitance, operating voltage, and equivalent series resistance. To accurately study these parameters, three fundamental electrochemical methods have been proposed and used among academia and industry, i.e., cyclic voltammetry (CV), galvanostatic charging/discharging (GCD) and electrochemical impedance spectroscopy (EIS) [2].

The measurements are typically conducted on a potentiostat/galvanostat, using either two or three electrode systems. The three-electrode electrochemical cell consists of a working electrode (WE), a counter electrode (CE), and a reference electrode (RE) in an electrolyte solution.

In the focus of probing for novel electrode materials, the previously prepared composites were tested as supercapacitor electrodes and their supercapacitive behavior was investigated using different electrochemical techniques.

9.2. Experimental details

9.2.1. Materials

Dimethylformamide and sulfuric acid were purchased from Sigma–Aldrich (Germany), Liquion solution (5 wt.% Nafion) was purchased from Ion Power (USA).

9.2.2. Preparation of supercapacitor electrodes

The working electrodes were prepared by drop-casting the nafion-impregnated samples onto a platinum electrode of 3.0 mm in diameter for CMF/PANI and CMFPGs composites, and on a glassy carbon (GC) electrode of 3.0 mm in diameter for CNW/PANI and CNWPGs composites. Typically, 15 mg of active material was dispersed in 1mL of DMF containing 10 μ L of 5% nafion solution using an agate mortar/pestle to get a homogeneous dispersion. This sample was then dropped onto the working electrode and dried in ambient conditions. The mass loadings of the samples were 0.8-1.6 mg cm⁻².

9.2.3. Electrochemical characterization techniques

Electrochemical measurements i.e., cyclic voltammetry (CV), galvanostatic charge discharge (GCD) and electrochemical impedance spectroscopy (EIS) were carried out in 1M H₂SO₄ aqueous electrolyte solution at room temperature with a conventional three-electrode cell system on a VoltaLab PGZ 301 (Radiometer Analytical, France) for CMF/PANI and CMFPGs composites, and an Autolab PGSTAT302N potentiostat/galvanostat (Metrohm, Netherlands) for CNW/PANI and CNWPGs composites. A platinum disc electrode is used as counter electrode and an SCE or an Ag/AgCl electrodes were used as reference electrodes. The specific capacitance (Cs) derived from the discharge curves was calculated as per the formula

$$Cs = \frac{I \times \Delta t}{m \times \Delta V} \quad (9.1)$$

wherein I is the discharge current (A), Δt is the discharge time (s), m is the loaded mass of the composite (g), and ΔV is the potential drop upon discharging (excluding the IR drop) (V).

9.3. Results and discussion

The supercapacitive behavior of cellulose/PANI composites was evaluated by cyclic voltammetry (CV), galvanostatic charge-discharge (GCD) and electrochemical impedance spectroscopy (EIS).

9.3.1. Cyclic voltammetry

Cyclic voltammetry (CV) is an ideal technique for probing the electrochemical behavior and characterizing the capacitive performance of electrode materials in supercapacitors [3, 4].

Figures 9.1 (a) and 9.2 (a) compare the CV curves of CMF/PANI with CMFPGs and CNW/PANI with CNWPGs composites electrodes, respectively, at scan rates of 50 mV s^{-1} and 100 mV s^{-1} , respectively.

The CV curves exhibit the pseudocapacitive behavior of the composites showing two couples of well-defined redox peaks, corresponding to the redox transition of PANI from a semiconducting state (leucoemeraldine form) to a conducting state (emeraldine form) as well as faradaic transformation of emeraldine/pernigraniline [5]. Obviously, CMFPGs and CNWPGs composites curves show significantly higher current densities and larger integrated CV areas (**Figures 9.1 (b) and 9.2 (b)**) as compared to CMF/PANI and CNW/PANI composites, respectively. Hence, suggesting an improved capacitive behavior after the incorporation of rGO. This enhanced electrocapacitive performance springs from the fact that graphene-hybrid composite electrodes integrate the high pseudocapacitance of PANI with the excellent electrical conductivity of graphene, as well as the improved surface area due to the fibrous feature of the cellulose fibers and whiskers [3, 6, 7]. Moreover, it is known that the pseudocapacitance of PANI comes mainly from the surface faradaic redox reactions, therefore, in comparison with PANI-coated CMF, PANI-coated CNW would provide a larger electrochemical active surface area, which is highly desirable to exploit the full advantages of PANI pseudocapacitance and rGO-based double-layer capacitance [7, 8]. Meanwhile, the high conductivity of graphene improves the conductivity of PANI, as the presence of graphene nanosheets provides a high contact interface between PANI and electrolyte [3, 9].

However, for both CMFPGs and CNWPGs, the highest current responses were observed for CMFPG10 and CNWPG10, and then the current densities significantly decreased as the rGO content increased in the composites. This phenomenon was explained by the agglomeration of graphene sheets

leading to a decrease in active surface area, and thereby resulting in relatively low capacitive behaviors, as reported elsewhere by Xie et al. for Co_3O_4 -rGO nanocomposites [8] and Yang et al. for rGO-NiO composites [10].

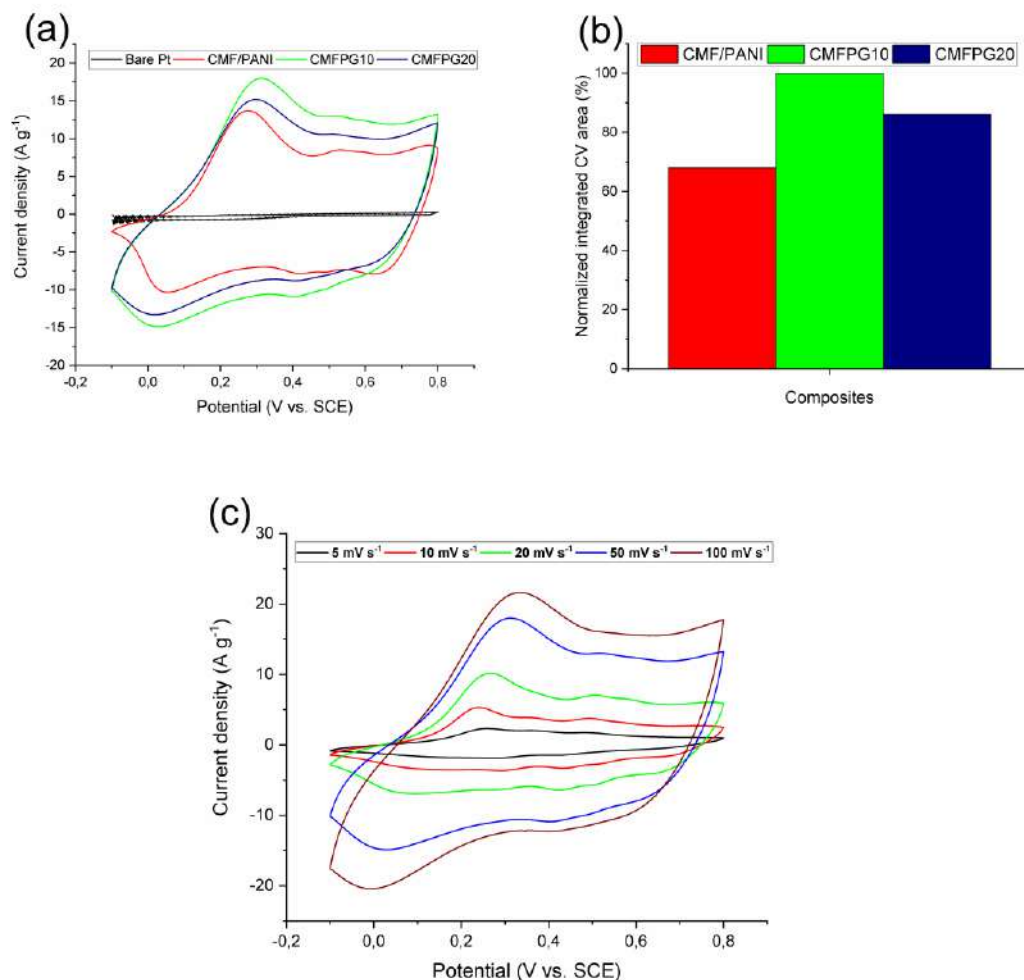


Figure 9.1: (a) CV curves of bare Pt, CMF/PANI, CMFPG10, and CMFPG20 at 50 mV s^{-1} . (b) Normalized integrated CV areas (%). (c) CV curves of CMFPG10 at different scan rates.

Figures 9.1 (c) and 9.2 (c) illustrate, respectively, the CV curves of CMFPG10 and CNWPG10 composite electrodes at different scan rates (5, 10, 20, 50 and 100 mV s^{-1}).

Obviously, while increasing the scan rate, the current responses increase, thus, reflecting good rate ability and fast response to redox reactions [11, 12]. Furthermore, a positive shift of anodic peaks and a negative shift of cathodic peaks can be observed, which is mainly due to the strengthened electric polarization and the possible kinetic irreversibility of electrolyte ions at the electrode surface during the

redox reaction at high scan rates [13]. In addition, the CV curves deviate from the ideal rectangular shape, indicating the dominance of PANI pseudocapacitance [14].

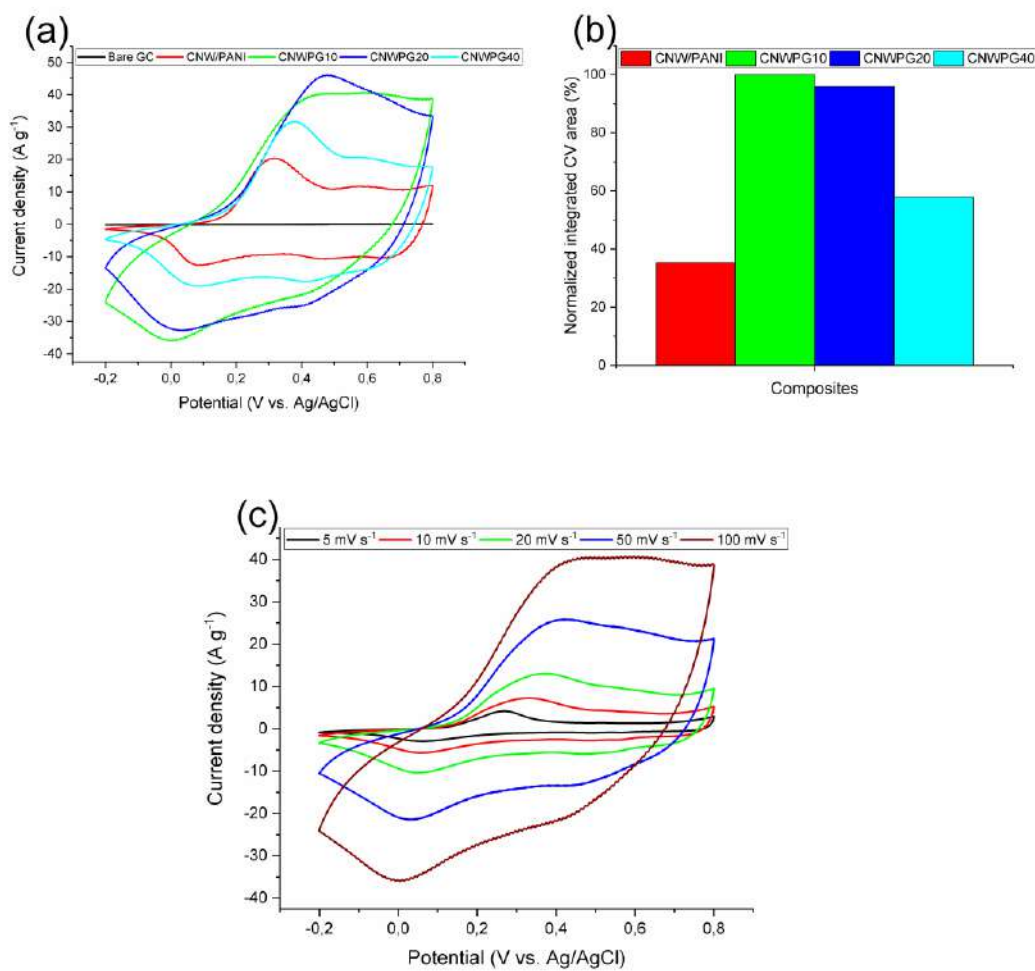


Figure 9.2: (a) CV curves of bare GC, CNW/PANI, CNWPG10, CNWPG20 and CNWPG40 at 100 mV s^{-1} . (b) Normalized integrated CV areas (%). (c) CV curves of CNWPG10 at different scan rates.

9.3.2. Galvanostatic charge/discharge

Figures 9.3 (a) and 9.4 (a) compare the galvanostatic charge/discharge (GCD) curves of CMF/PANI with CMFPGs and CNW/PANI with CNWPGs composites electrodes, respectively, at a current density of 1 A g^{-1} .

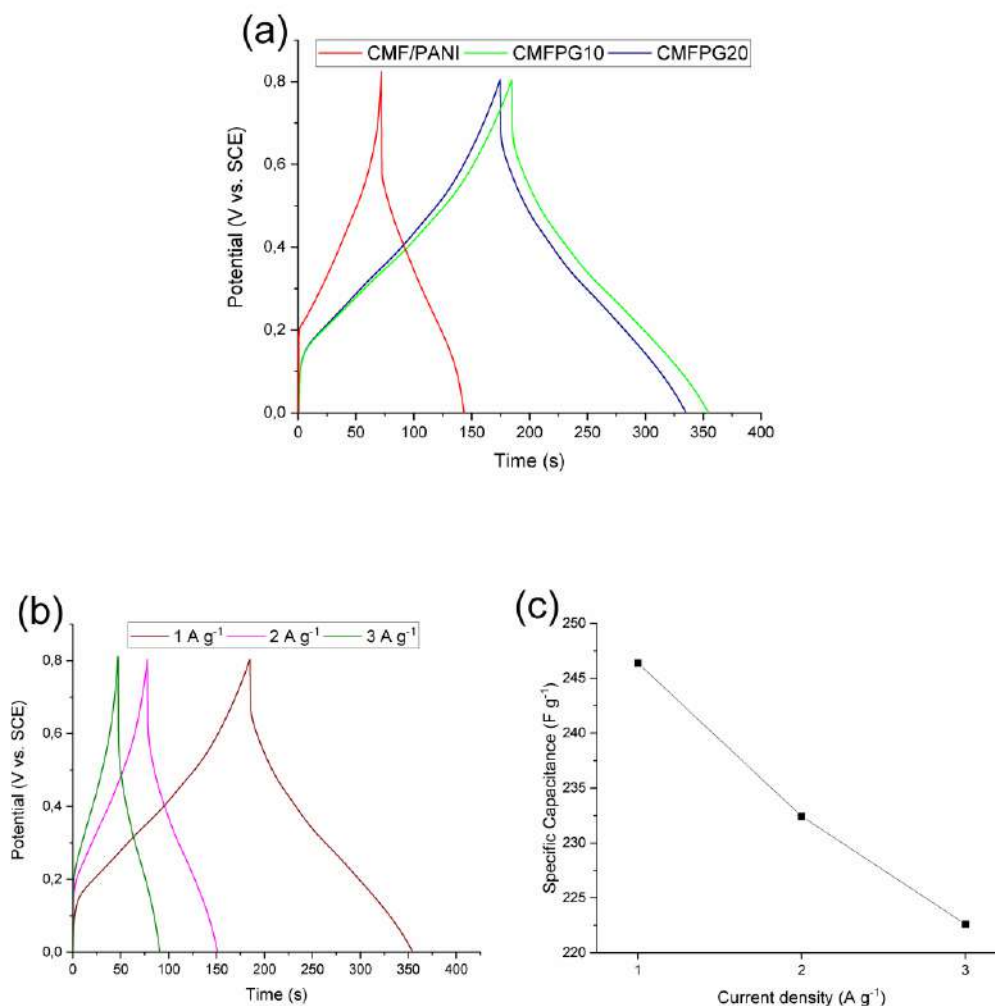


Figure 9.3: (a) GCD profiles of CMF/PANI, CMFPG10, and CMFPG20 at a current density of 1 A g⁻¹. (b) GCD profiles of CMFPG10 at different current densities. (c) Cs of CMFPG10 as a function of various current densities.

It is clearly visible that each prepared composite exhibits an almost symmetric charging and discharging curves, implying good reversible pseudocapacitance in the studied potential and current ranges [13]. Moreover, the calculated specific capacitances at 1 A g⁻¹ were Cs=122.61, 246.39, and 232.88 F g⁻¹ for CMF/PANI, CMFPG10 and CMFPG20, respectively, and Cs= 135.35, 465.32, 439.82, and 311.79 F g⁻¹ for CNW/PANI, CNWPG10, CNWPG20 and CNWPG40, respectively. A noticeable increase in specific capacitance was achieved by incorporating graphene in the composites. However, the Cs decreased significantly by further increasing the rGO content in the composites, which means that introducing higher contents of rGO into cellulose/PANI matrices can cause a serious

9. Preparation of supercapacitor electrodes and their electrochemical characterization

agglomeration of graphene sheets and thus would lead to a decrease of the surface area, resulting in less electrochemical utilization of PANI and graphene sheets [14, 15]. Besides, if the content of rGO is too much, the relatively low specific capacitance of restacked rGO itself will effectively lower the capacitance of the whole composite [15]. The latter observations are totally consistent with the CV results discussed previously.

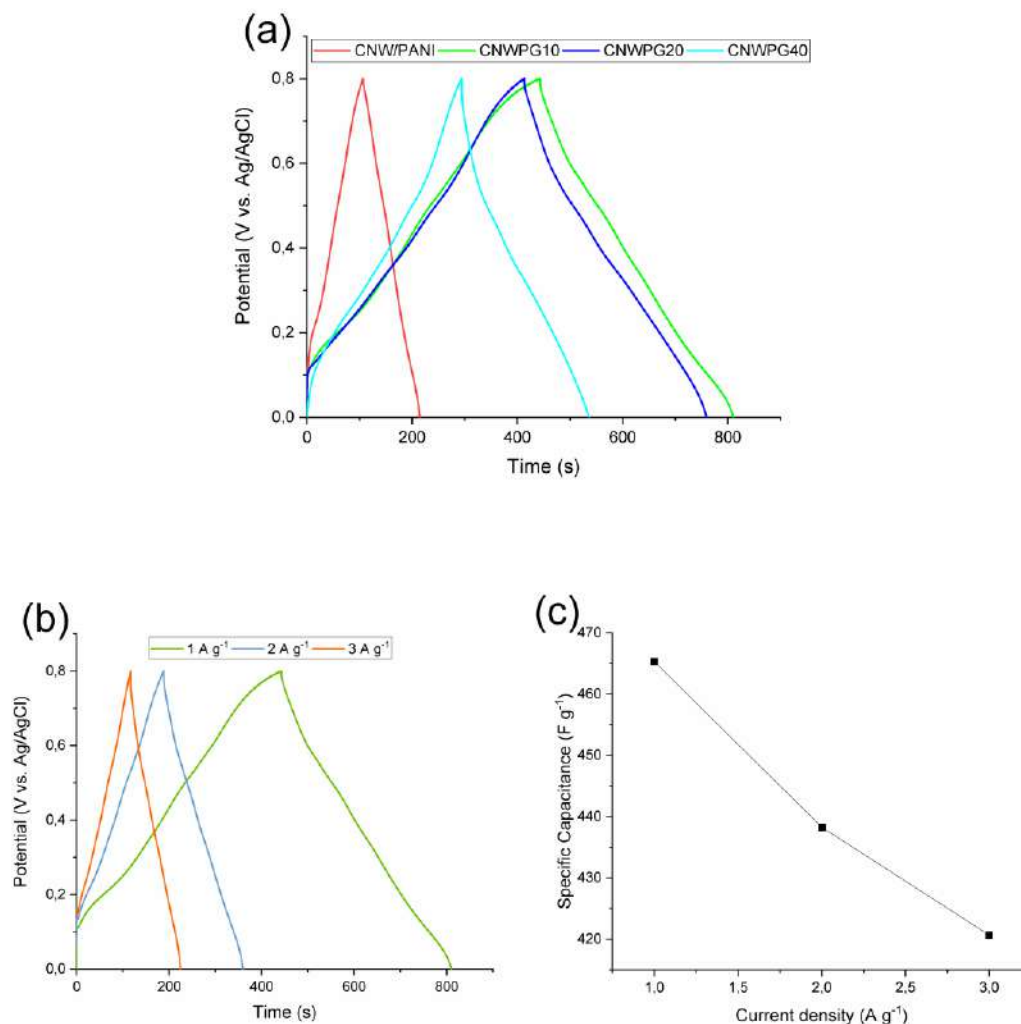


Figure 9.4: (a) GCD profiles of CNW/PANI, CNWPG10, CNWPG20 and CNWPG40 at a current density of 1 A g⁻¹. (b) GCD profiles of CNWPG10 at different current densities. (c) Cs of CNWPG10 as a function of various current densities.

It is pointed out that, the calculated specific capacitance of CMF/PANI is noticeably lower than that of CNW/PANI electrode, reflecting the fact that PANI-coated CNW would provide a larger electrochemical active surface area to maximize PANI utilization efficiency [7].

Figures 9.3 (b) and **9.4 (b)** depict the GCD curves of CMFPG10 and CNWPG10 composite electrodes, respectively. The measurements were performed within a potential range from 0 to 0.8 V and at current densities of 1, 2 and 3 A g⁻¹ in 1M H₂SO₄. In addition, the specific capacitances (Cs) are plotted in **Figures 9.3 (c)** and **9.4 (c)** as a function of various current densities for each sample.

For CMFPG10, the Cs values were 246.39, 232.44 and 222.62 F g⁻¹, at 1, 2 and 3 A g⁻¹, respectively. While Cs values of 465.32, 438.29 and 420.66 F g⁻¹, at 1, 2 and 3 A g⁻¹, respectively, were achieved for CNWPG10. The decrease in specific capacitance upon increasing the current density is attributed to the limited ion-diffusion rate and/or the increased IR drop at higher current densities [16].

Table 9.1 exhibits a comparison of the performance of PANI-based graphene composites in supercapacitor electrodes, which were prepared using different methods and then characterized using the conventional three-electrode cell system at a current density of 1 A g⁻¹. Obviously, the specific capacitances of the as-prepared CMFPG10 and CNWPG10 composite electrodes are comparable to or even better than a wide range of PANI-based graphene composite electrodes reported in recent years.

The remarkable Cs values are attributed to the good dispersion of PANI coating around cellulose microfibers and nanowhiskers as well as the presence of graphene nanosheets [17], this combination would effectively provide a larger electrolyte/electrode contact surface area for redox reactions and enhance the capacitive performance of the composites [3, 9, 17].

Table 9.1: Comparison of the performance of PANI-based graphene composites in supercapacitor electrodes at a current density of 1 A g⁻¹.

Composite	Preparation methods	Electrolyte	Specific capacitance (F g ⁻¹)	Ref.
Gr/PANI Nanofibers	In situ chemical polymerization	1M H ₂ SO ₄	210	[18]
PANI/rGO hybrid film	Self-assembly	1M H ₂ SO ₄	218.43	[19]
Graphene-wrapped PANI Nanofibers	Self-assembly	1M Et ₄ N ⁺ BF ₄ ⁻ /PC	236	[20]
CMF/PANI/rGO	Solution mixing	1M H ₂ SO ₄	246.39	This work
CFG/PANI	In situ chemical polymerization	1M H ₂ SO ₄	262.35	[21]
Gr@PANI nanoworms	Self-assembly	1M H ₂ SO ₄	309.8	[22]
PANI nanocones on pristine graphene	In situ chemical polymerization	1M H ₂ SO ₄	341	[11]
CNF/GNS/PANI film	Solution mixing + Vacuum filtration	1M H ₂ SO ₄	342.87	[23]
Amide Group-Connected Gr/PANI Nanofibers	Solution mixing	2M H ₂ SO ₄	361.9	[24]
CNF/GNS/PANI film	In situ chemical polymerization	1M H ₂ SO ₄	431	[25]
CNW/PANI/rGO	Solution mixing	1M H ₂ SO ₄	465.32	This work
PANI nanofibers/N-doped rGO hydrogels	Chemical polymerization + Hydrothermal process	1M H ₂ SO ₄	610	[26]
Graphene-wrapped PANI-HS	Self-assembly	1M H ₂ SO ₄	614	[27]
PANI nanorods on rGO sponges	Self-assembly	1M H ₂ SO ₄	662	[28]
Gr-PANI paper	In situ electropolymerization	1M H ₂ SO ₄	763	[29]

CFG: Carboxyl-functionalized graphene / Gr: Graphene / GNS: Graphene nanosheets / PC: Propylene carbonate / CNF: Cellulose nanofibers / PANI-HS: Polyaniline hollow spheres

9.3.3. Electrochemical impedance spectroscopy (EIS)

Electrochemical impedance spectroscopy (EIS) is a technique complementary to galvanostatic cycling measurements which provides more information on the electrochemical frequency behavior of the system. The EIS data were analyzed using Nyquist plots. A Nyquist plot shows the frequency response of the electrode/electrolyte system, it is a plot of the (-) imaginary component ($-Z''$) of the impedance against the real component (Z'). Each data point is at a different frequency with the lower left portion of the curve corresponding to the higher frequencies.

As revealed by CV and GCD results, the CNW/PANI and CNWPGs composite electrodes showed the best capacitive performance, therefore, they were further characterized using EIS measured at open circuit potential in aqueous solution 1M H₂SO₄. All measurements were plotted on a frequency band ranging between 100 KHz and 0.1 Hz, with an alternative current voltage of 10 mV. The results are depicted in **Figure 9.5**.

The common feature of the Nyquist plots is a depressed semicircle in the high frequency region, followed by a straight line in the low frequency region. The semicircle in the Nyquist plot results from the parallel combination of resistance and capacitance, it is related to the presence of electron transfer limiting step at the interface between electrode material and electrolyte [30, 31]. The diameter of the semicircle gradually decreases from CNW/PANI to CNWPGs composite indicating fewer obstructions in the electron transfer process due to the high conductivity of rGO sheets [30, 32]. The linear part, in the low frequency region, corresponds to the diffusion-controlled doping and undoping of ions, a consequence of the Warburg behavior [30, 33].

Furthermore, the equivalent circuit in the inset of **Figure 9.5** is used to fit the CNWPG10 Nyquist plot by ZView software V3.1 (Scribner Associates Inc.). The equivalent series resistance (denoted as R_s) is related to the intrinsic electronic/ionic conductivity of electrode substrate, active material, and electrolyte [34]. The R_s value is acquired from the x-intercept of the curve at high-frequency end and is estimated as 4.06 Ω . R_{CT} and R_{SEI} are associated with the resistance of charge-transfer and ions migration through the solid/electrolyte interface (SEI), respectively [34, 35]. W is the Warburg impedance contribution. CPE_1 and CPE_2 are constant phase elements used to replace the double-layer capacitance of the electrode/electrolyte interface and the pseudocapacitance of the electroactive material, respectively [36, 37]. In contrast to the ideal capacitor elements (C_{dl}), constant

phase elements (CPEs) reflect the interfacial irregularities associated with the electrode geometry such as porosity, and roughness of the electrode [32].

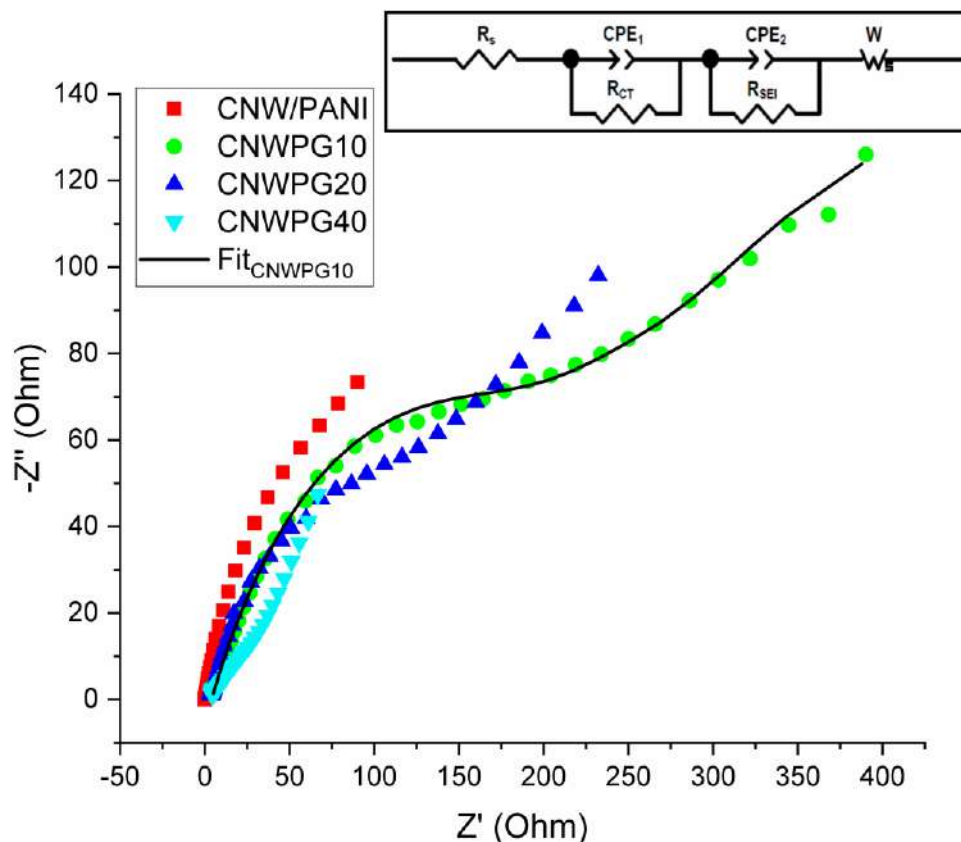


Figure 9.5: The impedance data of CNW/PANI and CNWPGs composite electrodes.

9.4. Conclusion

This chapter was framed within the arena of constant probing for novel supercapacitor electrode materials. The pre-prepared cellulose/PANI/rGO composites were applied as electrode materials, wherein, the active material was deposited on electrochemically inert current collectors and characterized using different electrochemical techniques.

CV data suggested that the capacitive behaviors of all composite electrodes are mainly dominated by pseudocapacitance rather than electric double-layer capacitance. GCD results revealed an almost symmetric charging and discharging curves, implying good reversible pseudocapacitance in the studied potential and current ranges. Furthermore, CNW/PANI composite electrode showed a specific capacitance noticeably higher than that of CMF/PANI. Moreover, the calculated specific capacitances

of CMFPG10 and CNWPG10 composite electrodes at a current density of 1 A/g were 246.39 and 465.32 F/g, respectively. The latter C_s value is comparable to or even better than a wide range of PANI-based graphene composite electrodes reported in recent years. This enhanced electrocapacitive performance springs from the fact that graphene-hybrid composite electrodes integrate the high pseudocapacitance of PANI with the excellent electrical conductivity of graphene, as well as the improved surface area due to the fibrous feature of the cellulose fibers and whiskers.

9.5. References

- [1]. Q. Meng, K. Cai, Y. Chen, L. Chen. Research progress on conducting polymer based supercapacitor electrode materials. *Nano Energy*. **2017**. 36, 268-85.
- [2]. S. Zhang, N. Pan. Supercapacitors Performance Evaluation. *Advanced Energy Materials*. **2015**. 5(6), 1401401-n/a.
- [3]. A. Sayah, F. Habelhames, A. Bahloul, B. Nessark, *et al.* Electrochemical synthesis of polyaniline-exfoliated graphene composite films and their capacitance properties. *Journal of Electroanalytical Chemistry*. **2018**. 818, 26-34.
- [4]. Y. Qu, C. Lu, Y. Su, D. Cui, *et al.* Hierarchical-graphene-coupled polyaniline aerogels for electrochemical energy storage. *Carbon*. **2018**. 127, 77-84.
- [5]. T. Fan, S. Tong, W. Zeng, Q. Niu, *et al.* Self-assembling sulfonated graphene/polyaniline nanocomposite paper for high performance supercapacitor. *Synthetic Metals*. **2015**. 199, 79-86.
- [6]. F. Wang, H.-J. Kim, S. Park, C.-D. Kee, *et al.* Bendable and flexible supercapacitor based on polypyrrole-coated bacterial cellulose core-shell composite network. *Composites Science and Technology*. **2016**. 128, 33-40.
- [7]. Z. Wang, P. Tammela, M. Strømme, L. Nyholm. Cellulose-based Supercapacitors: Material and Performance Considerations. *Advanced Energy Materials*. **2017**. 7(18), 1700130.
- [8]. L.-J. Xie, J.-F. Wu, C.-M. Chen, C.-M. Zhang, *et al.* A novel asymmetric supercapacitor with an activated carbon cathode and a reduced graphene oxide–cobalt oxide nanocomposite anode. *Journal of Power Sources*. **2013**. 242, 148-56.
- [9]. D.-W. Wang, F. Li, J. Zhao, W. Ren, *et al.* Fabrication of Graphene/Polyaniline Composite Paper via In Situ Anodic Electropolymerization for High-Performance Flexible Electrode. *ACS Nano*. **2009**. 3(7), 1745-52.
- [10]. Y.-Y. Yang, Z.-A. Hu, Z.-Y. Zhang, F.-H. Zhang, *et al.* Reduced graphene oxide–nickel oxide composites with high electrochemical capacitive performance. *Materials Chemistry and Physics*. **2012**. 133(1), 363-8.
- [11]. N. Song, W. Wang, Y. Wu, D. Xiao, *et al.* Fabrication of highly ordered polyaniline nanocone on pristine graphene for high-performance supercapacitor electrodes. *Journal of Physics and Chemistry of Solids*. **2018**. 115, 148-55.
- [12]. H. Mi, X. Zhang, S. Yang, X. Ye, *et al.* Polyaniline nanofibers as the electrode material for supercapacitors. *Materials Chemistry and Physics*. **2008**. 112(1), 127-31.
- [13]. F. S. Omar, A. Numan, N. Duraisamy, M. M. Ramly, *et al.* Binary composite of polyaniline/copper cobaltite for high performance asymmetric supercapacitor application. *Electrochimica Acta*. **2017**. 227(Supplement C), 41-8.

- [14]. J. Li, H. Xie, Y. Li, J. Liu, *et al.* Electrochemical properties of graphene nanosheets/polyaniline nanofibers composites as electrode for supercapacitors. *Journal of Power Sources*. **2011**. 196(24), 10775-81.
- [15]. P. Cao, L. Wang, Y. Xu, Y. Fu, *et al.* Facile hydrothermal synthesis of mesoporous nickel oxide/reduced graphene oxide composites for high performance electrochemical supercapacitor. *Electrochimica Acta*. **2015**. 157, 359-68.
- [16]. Y.-S. Wang, S.-M. Li, S.-T. Hsiao, W.-H. Liao, *et al.* Integration of tailored reduced graphene oxide nanosheets and electrospun polyamide-66 nanofabrics for a flexible supercapacitor with high-volume- and high-area-specific capacitance. *Carbon*. **2014**. 73(Supplement C), 87-98.
- [17]. H. Wang, E. Zhu, J. Yang, P. Zhou, *et al.* Bacterial Cellulose Nanofiber-Supported Polyaniline Nanocomposites with Flake-Shaped Morphology as Supercapacitor Electrodes. *The Journal of Physical Chemistry C*. **2012**. 116(24), 13013-9.
- [18]. K. Zhang, L. L. Zhang, X. S. Zhao, J. Wu. Graphene/Polyaniline Nanofiber Composites as Supercapacitor Electrodes. *Chemistry of Materials*. **2010**. 22(4), 1392-401.
- [19]. T. Lee, T. Yun, B. Park, B. Sharma, *et al.* Hybrid multilayer thin film supercapacitor of graphene nanosheets with polyaniline: importance of establishing intimate electronic contact through nanoscale blending. *Journal of Materials Chemistry*. **2012**. 22(39), 21092-9.
- [20]. S. Zhou, H. Zhang, Q. Zhao, X. Wang, *et al.* Graphene-wrapped polyaniline nanofibers as electrode materials for organic supercapacitors. *Carbon*. **2013**. 52, 440-50.
- [21]. Y. Liu, R. Deng, Z. Wang, H. Liu. Carboxyl-functionalized graphene oxide–polyaniline composite as a promising supercapacitor material. *Journal of Materials Chemistry*. **2012**. 22(27), 13619-24.
- [22]. Y. Luo, D. Kong, Y. Jia, J. Luo, *et al.* Self-assembled graphene@PANI nanoworm composites with enhanced supercapacitor performance. *RSC Advances*. **2013**. 3(17), 5851-9.
- [23]. Z. Chen, C. Wei, Y. Gong, J. Lv, *et al.* Electrochemical Properties of Cellulose Nanofiber/Graphene Nanosheet/Polyaniline Composite Film [J]. *International Journal of Electrochemical Science*. **2016**. 11(12), 9800-11.
- [24]. L. Jianhua, A. Junwei, Z. Yecheng, M. Yuxiao, *et al.* Preparation of an Amide Group-Connected Graphene–Polyaniline Nanofiber Hybrid and Its Application in Supercapacitors. *ACS Applied Materials & Interfaces*. **2012**. 4(6), 2870-6.
- [25]. Z. Chen, C. Wei, Y. Gong, J. Lv, *et al.* Preparation and Electrochemical Performances of Cellulose Nanofiber/Graphene Nanosheet/Polyaniline Composite Film via in-Situ Polymerization. *INTERNATIONAL JOURNAL OF ELECTROCHEMICAL SCIENCE*. **2017**. 12(7), 6662-75.
- [26]. J. Luo, W. Zhong, Y. Zou, C. Xiong, *et al.* Preparation of morphology-controllable polyaniline and polyaniline/graphene hydrogels for high performance binder-free supercapacitor electrodes. *Journal of Power Sources*. **2016**. 319, 73-81.
- [27]. W. Fan, C. Zhang, W. W. Tjiu, K. P. Pramoda, *et al.* Graphene-Wrapped Polyaniline Hollow Spheres As Novel Hybrid Electrode Materials for Supercapacitor Applications. *ACS Applied Materials & Interfaces*. **2013**. 5(8), 3382-91.
- [28]. K. Halab Shaeli Iessa, Y. Zhang, G. Zhang, F. Xiao, *et al.* Conductive porous sponge-like ionic liquid-graphene assembly decorated with nanosized polyaniline as active electrode material for supercapacitor. *Journal of Power Sources*. **2016**. 302, 92-7.
- [29]. H.-P. Cong, X.-C. Ren, P. Wang, S.-H. Yu. Flexible graphene–polyaniline composite paper for high-performance supercapacitor. *Energy & Environmental Science*. **2013**. 6(4), 1185-91.
- [30]. M. Ghasem Hosseini, E. Shahryari. A Novel High-Performance Supercapacitor based on Chitosan/Graphene Oxide-MWCNT/Polyaniline. *Journal of Colloid and Interface Science*. **2017**. 496, 371-81.

- [31]. P. Asen, S. Shahrokhian. A High Performance Supercapacitor Based on Graphene/Polypyrrole/Cu₂O–Cu(OH)₂ Ternary Nanocomposite Coated on Nickel Foam. *The Journal of Physical Chemistry C*. **2017**. 121(12), 6508-19.
- [32]. L. Tang, F. Duan, M. Chen. Green synthesis of silver nanoparticles embedded in polyaniline nanofibers via vitamin C for supercapacitor applications. *Journal of Materials Science: Materials in Electronics*. **2017**. 28(11), 7769-77.
- [33]. D. Ghosh, S. Giri, A. Mandal, C. K. Das. Supercapacitor based on H⁺ and Ni²⁺ co-doped polyaniline–MWCNTs nanocomposite: synthesis and electrochemical characterization. *RSC Advances*. **2013**. 3(29), 11676-85.
- [34]. M.-S. Wu, C. Wang, J.-J. Jow. Self-assembly of one-dimensional nitrogen-doped hollow carbon nanoparticle chains derived from zinc hexacyanoferrate coordination polymer for lithium-ion capacitors. *Electrochimica Acta*. **2016**. 222, 856-61.
- [35]. Y. Wang, M. Liu, X. Zhao, D. Cao, *et al.* Insights into heterogeneous catalysis of peroxydisulfate activation by boron-doped ordered mesoporous carbon. *Carbon*. **2018**. 135, 238-47.
- [36]. B. Zhu, Z. Deng, W. Yang, H. Wang, *et al.* Pyrolyzed polyaniline and graphene nano sheet composite with improved rate and cycle performance for lithium storage. *Carbon*. **2015**. 92, 354-61.
- [37]. B. D. Boruah, A. Misra. Polyethylenimine mediated reduced graphene oxide based flexible paper for supercapacitor. *Energy Storage Materials*. **2016**. 5, 103-10.

10

Conclusions & prospects

Cellulosic fiber-reinforced polymeric composites are finding more and more applications in various fields ranging from construction industry to packaging, energy devices and automotive industry. In this context, cellulose/conductive polymers/graphene composites offer a unique combination of environmental benefits and enhanced performance for energy storage applications, including supercapacitors.

After doing a comprehensive literature review on cellulose fibers, graphene, supercapacitors, their electrode materials and characterization techniques, a sequence of steps were adopted and culminated in synthesizing conductive PANI-coated cellulose fibers and nanowhiskers hybridized with different ratios of reduced graphene oxide (rGO) for supercapacitors electrode applications.

Firstly, highly crystalline cellulose microfibrils (CMF) were successfully extracted from *Retama raetam* local plant with a yield of 52.1% by following a stepwise totally chlorine-free procedure including dewaxing, alkali, and bleaching treatments. The extracted CMF, which have a diameter of ~ 6-7 μm , were highly crystalline native cellulose I, with a crystallinity of 77.8% and a crystallite size of 3.62 nm. Moreover, TGA/DTG data shows a maximum decomposition peak at 311°C and a high char yield. These findings proved that *R. raetam* is a candidate renewable source for the production of cellulose fibers and should stimulate further research on their applications, particularly, as bio-fillers for polymer matrices.

In addition, cellulose nanowhiskers (CNW) were prepared by acid hydrolysis method from pure cotton fibers. The results revealed a 12% increase in cellulose crystallinity with significant

morphological differences in shape and size and no modification in cellulose type as compared to raw cotton fibers.

Next, reduced graphene oxide (rGO) was synthesized by a modified Hummers method involving sonication-assisted oxidation of graphite with potassium permanganate in a concentrated sulfuric acid solution while sonicating for specific periods of time followed by reduction with ascorbic acid as a non-toxic reducing agent. The results proved the synthesis of few-layer graphene and suggested the presence of residual oxygen-containing functional groups (OFGs), which had withstood the reduction process of GO.

The fabrication of cellulose/polyaniline (PANI)/rGO composites was achieved by a straightforward procedure, which involves, (I) preparation of CMF/PANI and CNW/PANI composites via in situ oxidative polymerization of aniline monomer on cellulose microfibers (CMF) and cellulose nanowhiskers (CNW), respectively, using hydrochloric acid as a dopant and ammonium persulphate (APS) as an initiator/oxidant, (II) hybridization of the as-prepared composites with different ratios of rGO, namely, 10, 20, and 40 wt.%. The characterization data verified that PANI was successfully coated on the surfaces of CMF and CNW and indicated the incorporation of rGO in the composites with more agglomeration of graphene sheets observed by increasing rGO ratio in the final composites. Furthermore, SEM micrographs revealed that the CMF/PANI composite retains the fibrous structure, while the CNW/PANI exhibited a compact sheet-like to granular shaped accumulation.


Further, in the research trend of investigating novel materials for supercapacitor electrodes, the pre-prepared composites were then tested as electrode materials, wherein they were deposited on platinum or glassy carbon substrates and characterized using different electrochemical techniques. Cyclic voltammetry (CV) and galvanostatic charge/discharge (GCD) data revealed that the capacitive behaviors of all composite electrodes are mainly dominated by pseudocapacitance with good reversibility in the 0-0.8 V potential range. Furthermore, CNW-based composites showed, generally, specific capacitances (Cs) significantly higher than that of CMF-based ones. Cs values as high as 465.32 and 246.39 F/g were achieved, respectively, for the former and the latter by the incorporation of rGO in 10 wt.%. The achieved Cs value of CNWPG10 composite electrode is comparable to or even better than a wide range of PANI-based graphene composite electrodes reported in recent years. This improved electrocapacitive performance springs from the fact that graphene-hybrid composite electrodes integrate the high pseudocapacitance of PANI with the excellent electrical conductivity of

graphene, as well as the improved surface area due to the fibrous feature of the cellulose fibers and whiskers.

As a prospective research career, this domain is still open for extensive study and investigation on:

- I- The effect of PANI to cellulose ratio on mechanical, morphological, and electrochemical properties of cellulose/PANI and cellulose/PANI/rGO composites.
- II- The comparison between electrochemical performances of PANI, cellulose/PANI and cellulose/PANI/rGO electrodes (taking only the mass of the active material into account).
- III- The effect of graphene and composites preparation methods on the electrochemical performances of the final electrodes.
- IV- Fabrication and characterization of fully packaged flexible supercapacitors based on the results achieved in the current thesis as a step towards research valorization.

Extraction and characterization of cellulose microfibrils from *Retama raetam* stems

Abdelkader Khenblouche^{1*} , Djamel Bechki¹, Messaoud Gouamid², Khaled Charradi³, Ladjel Segni⁴, Mohamed Hadjadj⁵ and Slimane Boughali¹

¹Laboratory of New and Renewable Energy in Arid Zones – LENREZA, University of Ouargla, Ouargla, Algeria

²Department of Chemistry, Faculty of Mathematics & Material Sciences, University of Ouargla, Ouargla, Algeria

³Laboratory of Nanomaterials and Systems for Renewable Energies – LaNSER, Research and Technology Center of Energy, Techno-park Borj-Cedria, Hammam-Lif, Tunis, Tunisia

⁴Laboratory of Process Engineering, Faculty of Applied Sciences, University of Ouargla, Ouargla, Algeria

⁵Laboratory of Valorization and Promotion of Saharian Resources – VPRS, University of Ouargla, Ouargla, Algeria

*khenblouche89@gmail.com

Abstract

Cellulose is the most abundant renewable resource in nature, it has various industrial applications due to its promising properties. *Retama raetam* is a wild plant belonging to the Fabaceae family, largely abundant in arid area which makes it a good candidate for industrial utilization. In the present study, highly crystalline cellulose microfibrils (77.8% CrI) were extracted from *Retama Raetam* stems as a novel renewable source. The samples underwent a dewaxing process, then the microfibrils were extracted using 7 wt% sodium hydroxide followed by a bleaching treatment. The extracted cellulose microfibrils were characterized by Scanning electron microscopy, Fourier transform infrared spectroscopy, X-ray Diffraction and thermo-gravimetric analysis.

Keywords: cellulose, microfibrils, *Retama raetam*, extraction, characterization.

How to cite: Khenblouche, A., Bechki, D., Gouamid, M., Charradi, K., Segni, L., Hadjadj, M., & Boughali, S. (2019). Extraction and characterization of cellulose microfibrils from *Retama raetam* stems. *Polímeros: Ciência e Tecnologia*, 29(1), e2019011. <https://doi.org/10.1590/0104-1428.05218>

1. Introduction

Over the last few decades, The use of natural fibers instead of synthetic fibers as reinforcement materials for polymer composites has gained considerable attention because of their unique characteristics, such as renewability, biodegradability, processing flexibility, low density, high specific strength and low-cost^[1,2]. In addition, natural fibers have applications in various fields such as bioenergy industries, automobiles, paper manufacturing and textile owing to their properties and broad availability^[1,3]. As a result, nowadays, the subject of many researchers worldwide focuses on the need to find alternative fiber sources^[4]. Among all natural fibers, cellulose has attracted much interest as it is the most abundant renewable resource in nature and the degradation of cellulosic biomass is an important part of the biosphere's carbon cycle^[5]. Its existence as the common material of plant cell walls was first investigated by Braconnot in 1819^[6] and Payen in 1838^[7]. It is a polydispersed linear polymer with a microfibrillar structure composed of poly-β (1→4)-D-glucose units with a syndiotactic configuration^[8,9], found in the cell walls as a network of microfibrils embedded in a non-cellulosic matrix^[10]. Several plants are rich in cellulose, i.e. cotton,

wood, bamboo, hemp, flax, and jute ...etc^[11]. In addition, cellulose fibers have been extracted from several sources such as; milkweed stems^[12], hop stems^[13], rice husk^[14], *Cissus quadrangularis* root^[15], *dichrostachys cinerea* bark^[1] and many more. Although several sources of natural fibers were investigated in detail, the isolation of cellulose fibers from *R. Raetam* has not been reported yet.

Retama raetam, locally known as R'tem, is a wild plant of the Fabaceae family. It is common to North and East Mediterranean regions^[16]. It is largely abundant in arid area; this abundance makes it a good candidate for industrial utilization. Moreover, the *Retama* species contributes to the bio-fertilization of poor grounds because of their aptitude to associate with fixing nitrogen bacteria *Rhizobia*^[17]. Therefore, the genus of the *Retama* is included in a re-vegetation program for degraded areas in semi-arid Mediterranean environments^[18].

In this research, Natural micro-sized cellulose fibers were extracted from *R. Raetam* stems using alkali and bleaching treatments, the resultant cellulose microfibrils were characterized using FTIR, SEM, XRD and TGA.

2. Materials and Methods

2.1 Materials

Stems of *R. raetam* subject of this study were collected in Ouargla, Algeria, in 2015. Acetone, Ethanol, Sodium hydroxide & Hydrogen peroxide were purchased from Sigma-Aldrich and were used without further purification.

2.2 Preparation of samples

Adult stems were cleaned with water and air dried, broken to the size of about 1 cm long and 1 mm width, grinded into powder with a Retsch SM100 Comfort cutting mill (Retsch GmbH, Haan, Germany), and sieved using a sieve size of 0.25 mm.

2.3 Microfibers extraction

The extraction of cellulose microfibers was performed using classical chemical treatments with adaptations in dewaxing, alkali and bleaching treatment processes. The totally chlorine-free extraction procedure can be described as follows:

2.3.1 Dewaxing

About 20g of powdered stems were first dewaxed in a Soxhlet reflux with a 2:1 (v/v) mixture of Acetone/Ethanol at 63 °C for 7 h, the main purpose of this step is to remove off waxes and extractives, the sample was then placed in a Buckner funnel and vacuum dried at room temperature for 3 h to remove traces of residual solvents.

2.3.2 Alkali treatment

The alkali treatment was performed to purify the cellulose by removing lignin and hemicellulose from *R. Raetam* fibers. The extractive-free sample was treated with an alkali solution (7 wt% NaOH) with a solvent to solid ratio of 10:1 at 80 °C for 3 h under mechanical stirring. This treatment was performed twice, after each treatment the solid was filtered and washed with distilled water until neutral pH.

2.3.3 Bleaching

A subsequent bleaching treatment was carried out to remove residual lignin and whiten the microfibers. The sample was immersed in a hydrogen peroxide solution (11%, v/v), the pH was adjusted to 11 using 7 wt% NaOH, the system was vigorously stirred for 3 h at 45 °C. For a more effective discoloration, the bleaching process was performed twice under the same conditions, after each treatment, the microfibers were filtered and washed with distilled water.

2.4 Fourier transform infrared spectroscopy

To analyze the chemical changes of the samples and investigate functional groups in the extracted cellulose we used Fourier Transmission Infra-Red Spectroscopy. The FTIR spectra were recorded on a Cary 660 FTIR Spectrometer (Agilent Technologies, USA) in a wavelength range of 4000–600 cm^{-1} with a resolution of 4 cm^{-1} .

2.5 X-ray Diffraction (XRD) analysis

The crystallinity of cellulose microfibers was investigated by X-ray diffraction (XRD) analysis, using a powder X-ray diffractometer (D8 Advance A25 Bruker AXS GmbH., Germany) with Cu K α radiation (1.5406 Å) at 40 kV and 25 mA, in the range of $2\theta = 5\text{--}60^\circ$ at a scanning rate of 0.02° s^{-1} . The crystallinity index (CrI) was calculated according to Segal equation^[19]:

$$CrI = 100 \times (I_{200} - I_{am}) / I_{200} \quad (1)$$

where I_{200} is the diffraction intensity at $2\theta = 22\text{--}23^\circ$; and I_{AM} is the minimum diffraction intensity at $2\theta = 18\text{--}20^\circ$.

The crystallite size was calculated as per the Scherrer equation^[20]

$$L_{h,k,l} = (0.94 \times \lambda) / (\beta \times \cos \theta) \quad (2)$$

where λ is X-rays wavelength; β is the full width at half maximum in radians; and θ is the Bragg angle.

2.6 Morphological structure

A scanning electron microscope (SEM) (Quanta 250 FEG, FEI, USA) with an accelerating voltage of 15 kV was used to investigate the microstructure and the surface morphology of the obtained cellulose microfibers.

2.7 Thermogravimetric Analysis (TGA)

In order to study the thermal stability of the extracted cellulose microfibers, thermogravimetric analysis (TGA) was performed using a Mettler Toledo TGA/DSC 3+ instrument. The scan was carried out from 25 to 600 °C at a heating rate of 10 °C/min and under nitrogen atmosphere.

3. Results and Discussion

3.1 Extraction method and cellulose yield

A stepwise totally chlorine-free procedure for the isolation of cellulose microfibers from *retama raetam* was proposed in this paper based on that adopted by Sun et al.^[21]

Table 1. Comparison of the crystallinity index of cellulose microfibers from various sources.

Source	Crystallinity index (CrI)	Reference
Coconut palm leaf sheath	47.7%	Uma Maheswari et al. ^[22]
Sugarcane bagasse	50%	Jonjankiat et al. ^[23]
Agave fibers	64.4%	Reddy et al. ^[24]
Mengkuang leaves	69.5%	Sheltami et al. ^[5]
Soy hulls	69.6%	Alemdar and Sain ^[25]
Commercial microcrystalline cellulose	73.91%	Kale et al. ^[20]
Sisal fibers	75% \pm 1	Morán et al. ^[26]
Wheat straw	77.8%	Alemdar and Sain ^[25]
Retama Raetam	77.8%	This work
Hibiscus sabdariffa	78.95%	Sonia and Priya Dasan ^[27]
Palmyra palm Fruits	81.9%	Reddy et al. ^[28]

with modifications. These modifications involve increasing sodium hydroxide and hydrogen peroxide concentrations as well as improving treatment time and/or temperature to enhance non-cellulosic components removal. Therefore, the isolation of *R. Raetam* cellulose microfibrils was successfully achieved without any additional harsh acid treatments (Table 1), which makes the suggested extraction process not only eco-friendly and cost-saving, but also yielding cellulose microfibrils of higher crystallinity and smaller diameters as further confirmed by XRD and SEM results.

Cellulose microfibrils yield was gravimetrically determined (calculated as the percentage of the extracted cellulose microfibrils over the initial raw sample weight) and was found to be 52.1%. This yield value is higher than that reported in literature for cellulose microfibrils extracted

from *Hibiscus sabdariffa* fibers (38.6%)^[27] and comparable to yield values of 52, 52 and 55% for cellulose microfibrils extracted from Coconut palm leaf sheath^[22], African Napier grass^[29] and Palmyra palm fruits^[28], respectively.

3.2 FT-IR spectroscopic analysis

Infrared spectroscopy is currently one of the most important analytical techniques available to scientists^[30]. It presents a relatively easy method of obtaining direct information on chemical changes that occur during chemical treatments^[31]. Furthermore, FT-IR analysis was conducted to investigate the presence of different functional groups in the isolated samples. Figure 1. shows the IR spectra of (a) untreated sample, (b) alkali treated sample and (c) bleached cellulose microfibrils. As summarized in Table 2,

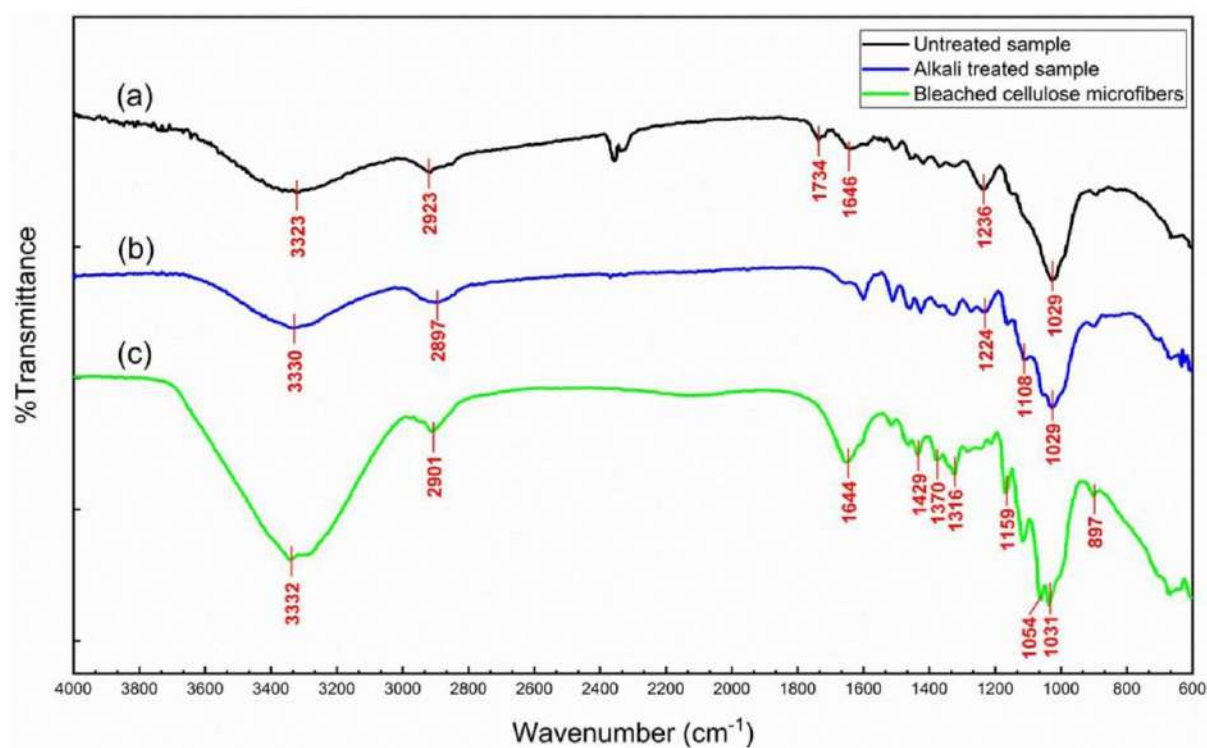


Figure 1. FT-IR spectra of (a) untreated sample, (b) alkali treated sample and (c) bleached cellulose microfibrils.

Table 2. The main observed IR bands and their assignments.

Spectra	Wavenumber (cm ⁻¹)	Assignment	Ref.
(a), (b), (c)	876-897	C-O-C stretching at the b-(1→4)-glycosidic linkages	Oh et al. ^[32]
(a), (b), (c)	1029-1031	C-O-C pyranose ring skeletal vibration	Sun et al. ^[33]
(b), (c)	1051-1054	C-O-C pyranose ring skeletal vibration	Sun et al. ^[33]
(a), (b), (c)	1144-1159	C-O-C stretching at the b-(1→4)-glycosidic linkages	Oh et al. ^[32]
(a), (b)	1224-1236	-COO vibration of acetyl groups / C-O stretching of the aryl group	Reddy et al. ^[28]
(a), (b), (c)	1316-1327	C-C and C-O skeletal vibrations	Gao et al. ^[34]
(a), (b), (c)	1370-1374	O-H bending	Gao et al. ^[34]
(a), (b), (c)	1417-1429	CH ₂ bending	Gao et al. ^[34]
(a), (b), (c)	1644-1646	OH bending of the absorbed water	Alcimdard and Sain ^[25]
(a)	1734	C=O stretching	Sain and Panthapulakka ^[35]
(a), (b), (c)	2896-2922	C-H stretching	Kondo and Sawatari ^[36]
(a), (b), (c)	3323-3332	H-bonded OH groups stretching	Kondo and Sawatari ^[36]

the cellulose spectrum is similar to those reported in literature for cellulose fibers^[37].

The band at 3332 cm^{-1} relates to the stretching of H-bonded OH groups, and the one at 2901 cm^{-1} to the C–H stretching^[36], we observe that the band around 3332 cm^{-1} is narrower and has a higher intensity for cellulose, which demonstrated that the extracted cellulose contained more –OH groups than in untreated sample^[10]. The band at 1644 cm^{-1} is associated with –OH bending of the absorbed water^[25]. Typical bands assigned to cellulose at 1159 cm^{-1} and 897 cm^{-1} are due to C–O–C stretching at the b-(1→4)-glycosidic linkages^[32]. The presence of these peaks showed the increase in the percentage of cellulosic components after the removal of non-cellulosic materials by chemical treatments^[38]. The absorption peak at $\sim 1734\text{ cm}^{-1}$ on the spectrum of the untreated sample (a) is attributed to the C=O stretching of the acetyl and uronic ester groups of polysaccharides^[9,35], it is also related to the p-coumeric acids of lignin and/or hemicellulose^[25], the absence of this peak after successive chemical treatments indicates the removal of most of lignin and hemicelluloses from the microfibrils. Another indicator of lignin and hemicellulose removal during the chemical treatments is the significant decrease in the intensity of the peak around 1236 cm^{-1} which is related to the –COO vibration of acetyl groups in hemicellulose and/or the C–O stretching of the aryl group in lignin^[28]. Noticeable peaks on spectrum (c) at 1429 cm^{-1} relates to the CH_2 bending and at 1370 cm^{-1} to the O–H bending. The absorbance at $\sim 1316\text{ cm}^{-1}$ is attributed to the C–C and C–O skeletal vibrations^[34]. The C–O–C pyranose ring skeletal vibration occurs in 1054 cm^{-1} and 1031 cm^{-1} ^[33].

3.3 X-ray Diffraction measurements

Figure 2 exhibits the XRD data of the extracted cellulose microfibrils. The cellulose amorphous phase is characterized by the low diffracted intensity at a 2θ value of 19.12° , whilst the peaks at 15.14° , 16.25° , 22.75° and 34.39° are attributable to the crystallographic planes of (1-10), (110), (200) and (004), respectively, which are characteristic of the typical cellulose I structure^[29,39]. The crystallinity index (CrI) of the bleached microfibrils was determined using Segal equation and was found to be 77.8%. Obviously, as illustrated in Table 1, this CrI value is higher than the value of 73.91% reported by Kale et al. for commercial microcrystalline cellulose from wood pulp^[20]. Moreover, it is higher than the CrI values reported in the literature for cellulose microfibrils isolated using different methods from various sources such as Sugarcane bagasse (50%)^[23], Agave fibers (64.4%)^[24], mengkuang leaves (69.5%)^[3] and Soy hulls (69.6%)^[25].

Furthermore, the crystallite size ($L_{h,k,l}$) which was found to be $3.62\text{ }\mu\text{m}$ is comparable to the reported sizes of cellulose crystallites (4 to 7 nm generally)^[40]. However, the calculated $L_{h,k,l}$ value is much lower than that reported for hydrolyzed commercial microcrystalline cellulose (10.32 nm). The higher CrI and the lower $L_{h,k,l}$ values suggest that the adopted stepwise chlorine-free extraction treatments were effective in removing most of amorphous domains leading to break the bundles of cellulose fibers to form smaller cellulose crystallites^[41,42].

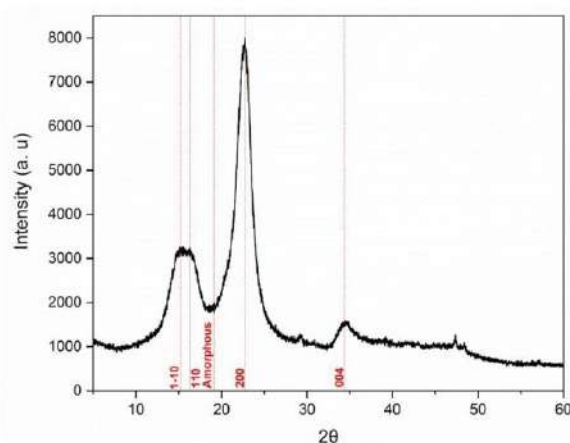


Figure 2. XRD diffractogram of the extracted R. Raetam cellulose microfibrils.

3.4 Morphological properties of chemically purified cellulose microfibrils

Figure 3 shows SEM micrographs of the chemical-purified cellulose microfibrils. After they had been subjected to alkaline solution treatment and bleaching, the cellulose microfibrils were separated into individual micro-sized fibers. These micro-sized cellulose fibers were reported to be composed of strong hydrogen bonding nanofibers^[43]. The diameter of the microfibrils is about 6–7 μm but the exact determination of their length is difficult.

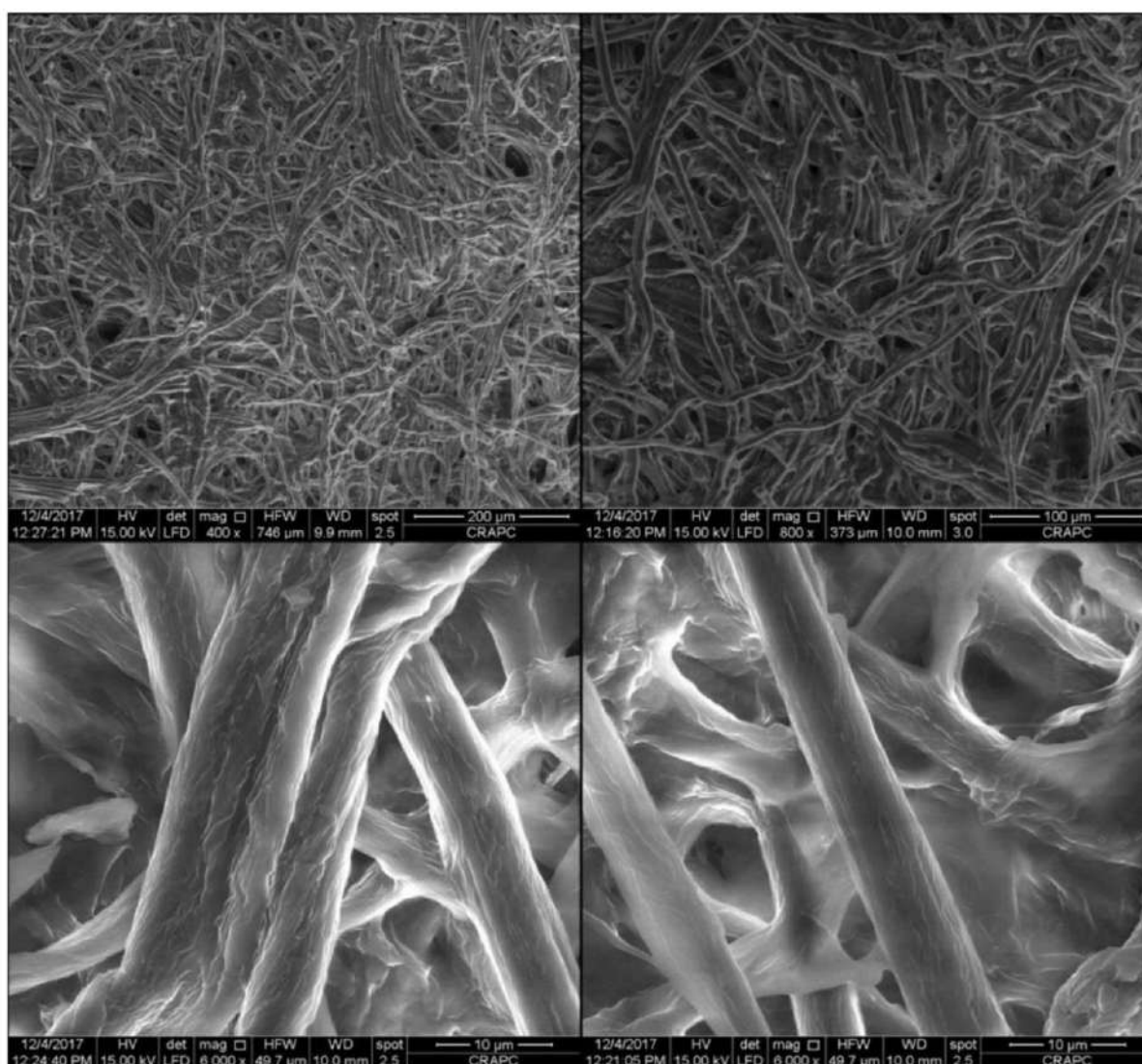
As Table 3. demonstrates, the extracted R. Raetam cellulose microfibrils are smaller in diameter as compared to those isolated by different extraction methods from various sources such as sisal fibers, agave fibers, coconut palm leaf sheath, soy hull and wheat straw^[22,24–26]. Moreover, they are comparable to cotton and sugarcane bagasse microfibrils extracted by sulfuric and nitric acid hydrolysis, respectively^[23,44]. This morphology and smaller diameter would enable R. Raetam cellulose microfibrils to be used for various applications ranging from reinforcing agents in biodegradable composites, to gel forming food and cosmetic additives^[24,45].

3.5 Thermal stability

Investigating thermal properties of cellulose microfibrils is a key factor for their applicability as reinforcing fillers in biocomposites^[38]. Figure 4a and 4b shows, respectively, the thermogravimetric analysis (TGA), and the derivative thermogram (DTG) curves for both the raw and bleached samples. TGA curves show an initial weight loss below 155°C , this initial drop (4.6% for raw sample and 6.5% for cellulose microfibrils) was due to the evaporation of moisture bounded on the surface of the samples, chemisorbed water bounded inside the samples and/or the compounds of low molecular weight such as extractives presented in the raw sample^[38,46], the presence of the absorbed water was affirmed previously through the FT-IR results. The main broader cellulose thermal degradation (50.84%) occurs over 179°C and involves synchronous multi-processes such as dehydration, depolymerization and decomposition

Table 3. Comparison of the diameters of cellulose microfibrils extracted from various sources by different extraction methods.

Source	Extraction method	diameter (μm)	Ref.
Sisal fibers	Alkali, peroxide and HNO_3/HAc treatments	12.8-31	Morán et al. ^[26]
Coconut palm leaf sheath	Chlorination, alkali and HNO_3/HAc treatments	10-15	Uma Maheswari et al. ^[22]
Soy hull	Alkali treatment and HCl Acid hydrolysis	10-15	Alemdar and Sain ^[25]
Wheat straw	Alkali treatment and HCl Acid hydrolysis	10-15	Alemdar and Sain ^[25]
Agave fibers	Chlorination, alkali and HNO_3/HAc treatments	8-14	Reddy et al. ^[24]
Hibiscus sabdariffa	Steam explosion and oxalic acid hydrolysis	10.04	Sonia and Priya Dasan ^[27]
Sisal fibers	Chlorination and alkali treatments	7-11.2	Morán et al. ^[26]
Cotton	Sulfuric acid hydrolysis	5-10	Chatterjee et al. ^[44]
Sugarcane bagasse	Nitric acid hydrolysis	5-10	Jonjankiat et al. ^[23]
Palmyra palm fruit	Chlorination, alkali and HNO_3/HAc treatments	4-11	Reddy et al. ^[28]
Napier grass fibers	Chlorination, alkali and HNO_3/HAc treatments	8.3	Reddy et al. ^[29]
Retama Raetam Stems	Alkali and alkaline peroxide treatments	6-7	This work
Jatropha Curcus L seed shell	Chlorination, alkali and HNO_3/HAc treatments	0.23-1.04	Puttaswamy et al. ^[45]

**Figure 3.** SEM images of the extracted *R. Raetam* cellulose microfibrils.

of glycosidic units^[47]. The raw sample showed separated pyrolysis processes within a wider temperature range, including thermal depolymerization of hemicellulose up to 273 °C, decomposition of cellulose up to 348 °C, and

the degradation of lignin up to 536 °C in addition to its simultaneous decomposition with other degradation stages due to its complex structure^[46]. DTG curves exhibited maximum decomposition rates at $\text{DTG}_{\text{max}} = 294$ °C and

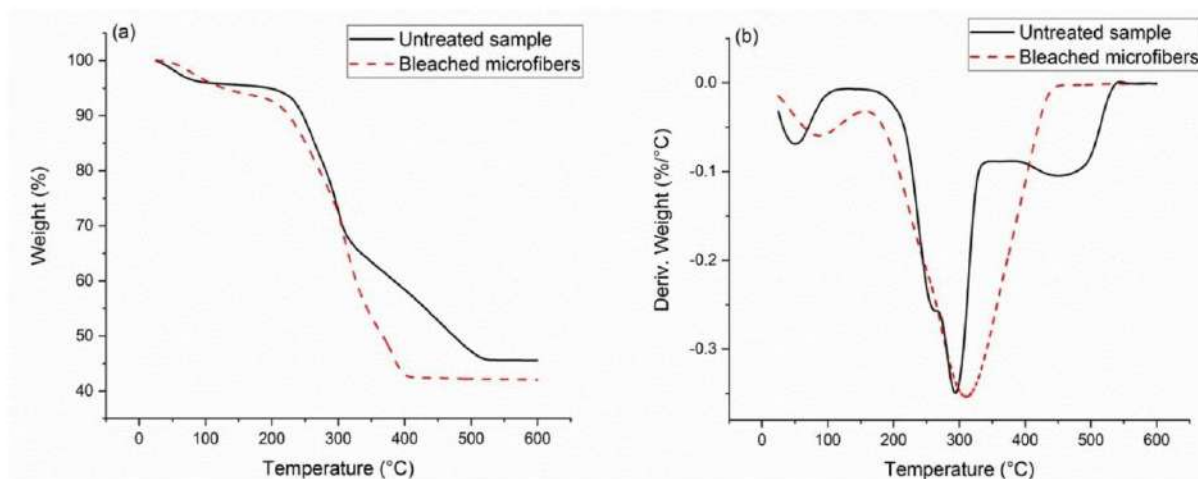


Figure 4. TGA (a) and DTG (b) curves of the untreated sample and the bleached cellulose microfibrers.

Table 4. DTGmax and char yields of cellulose microfibrers from different sources.

Samples	T _{max} (°C)	Char (%)	Reference
Date seeds cellulose microfibrers	300	11	Nabili et al. ^[48]
Bamboo cellulose microfibrers	328	13	Chen et al. ^[49]
Rice hulls microcrystalline cellulose	283	23	Adel et al. ^[50]
bean hulls microcrystalline cellulose	281	25	Adel et al. ^[50]
Onion skin cellulose microfibrers	333	26	Reddy and Rhim ^[51]
Retama Raetam cellulose microfibrers	311	42	This work
Cotton silver microcrystalline cellulose	340	57	Das et al. ^[52]
Jute microcrystalline cellulose	280	61	Das et al. ^[52]

311 °C for the raw and bleached samples, respectively. A shoulder can be clearly observed at 261 °C on the left side of the main peak of the raw sample DTG curve, which was due to initial decomposition of hemicellulose and non-cellulosic components^[47], while the broadening at 245 °C on the microfibrers DTG curve, could be an indicator of a broad distribution of molecular mass from cellulose or a residual content of hemicellulose which withstood the extracting procedures^[26]. Finally, the formation of a charred residue took place (46% for raw sample and 42% for cellulose microfibrers). The higher charred residue of the raw sample is due to the fact that the non-cellulosic components could induce higher char formation^[38]. However, R. Raetam cellulose microfibrers presented relatively high char yield when compared to literature (Table 4), indicating higher non-volatile carbonaceous material generated on pyrolysis^[53] and could indicate also a good thermal stability of the extracted cellulose microfibrers^[20,54].

4. Conclusion

The main goal of this work was to investigate the viability of Retama Raetam as a novel, renewable and low-cost source of cellulose microfibrers. The successful isolation of cellulose microfibrers was achieved with a yield of 52.1% by stepwise chemical treatments. The FTIR results revealed that the chemical treatments removed most of lignin and

hemicellulose from the sample. The extracted cellulose microfibrers were highly crystalline native cellulose I, with a crystallinity of 77.8% and a crystallite size of 3.62 μm. The diameter of the micro-sized fibers was about 6-7 μm. TGA/DTG curves show a maximum decomposition peak at 311 °C and a high char yield. These findings proved that R. Raetam is a candidate renewable source for the production of cellulose microfibrers and should stimulate further research on the use of these fibers for various applications such as cellulose nanocrystals preparation, reinforcement agent in green biocomposites and bio-fillers for polymer matrices.

5. References

- Baskaran, P., Kathiresan, M., Sentharamaikkannan, P., & Saravanakumar, S. (2018). Characterization of new natural cellulosic fiber from the bark of dichrostachys cinerea. *Journal of Natural Fibers*, 15(1), 62-68. <http://dx.doi.org/10.1080/15440478.2017.1304314>.
- Mohammed, L., Ansari, M. N. M., Pua, G., Jawaid, M., & Islam, M. S. (2015). A review on natural fiber reinforced polymer composite and its applications. *International Journal of Polymer Science*, 15. <http://dx.doi.org/10.1155/2015/243947>.
- Sheltami, R. M., Abdullah, I., Ahmad, I., Dufresne, A., & Kargarzadeh, H. (2012). Extraction of cellulose nanocrystals from mengkuang leaves (*Pandanus tectorius*). *Carbohydrate Polymers*, 88(2), 772-779. <http://dx.doi.org/10.1016/j.carbpol.2012.01.062>.
- Zain, N. F. M., Yusop, S. M., & Ahmad, I. (2014). Preparation and characterization of cellulose and nanocellulose from pomelo

- (*Citrus grandis*) albedo. *Journal of Nutrition & Food Sciences*, 5(1), 334. <http://dx.doi.org/10.4172/2155-9600.1000334>.
5. Zhao, L., Pang, Q., Xie, J., Pei, J., Wang, F., & Fan, S. (2013). Enzymatic properties of *Thermoanaerobacterium thermosaccharolyticum* β -glucosidase fused to Clostridium cellulovorans cellulose binding domain and its application in hydrolysis of microcrystalline cellulose. *BMC Biotechnology*, 13(1), 101. <http://dx.doi.org/10.1186/1472-6750-13-101>. PMID:24228818.
 6. Braconnot, H. (1819). Sur la conversion du corps ligneux en gomme, en sucre, et en un acide d'une nature particulière, par le moyen de l'acide sulfurique; conversion de la même substance ligneuse en ulmine par la potasse. *Annales de Chimie et de Physique*, 12, 172-195.
 7. Payen, A. (1838). Mémoire sur la composition du tissu propre des plantes et du ligneux. *The C++ Report*, 7, 1052-1056.
 8. Naduparambath, S., Jinitha, T., Shaniba, V., Sreejith, M., Balan, A. K., & Purushothaman, E. (2018). Isolation and characterisation of cellulose nanocrystals from sago seed shells. *Carbohydrate Polymers*, 180, 13-20. <http://dx.doi.org/10.1016/j.carbpol.2017.09.088>. PMID:29103489.
 9. Vestena, M., Gross, I. P., Muller, C. M. O., & Pires, A. T. N. (2016). Isolation of whiskers from natural sources and their dispersed in a non-aqueous medium. *Polimeros*, 26(4), 327-335. <http://dx.doi.org/10.1590/0104-1428.2367>.
 10. Penjumras, P., Rahman, R. B. A., Talib, R. A., & Abdan, K. (2014). Extraction and characterization of cellulose from durian rind. *Agriculture and Agricultural Science Procedia*, 2, 237-243. <http://dx.doi.org/10.1016/j.aaspro.2014.11.034>.
 11. Li, M., Wang, L., Li, D., Cheng, Y.-L., & Adhikari, B. (2014). Preparation and characterization of cellulose nanofibers from de-pectinated sugar beet pulp. *Carbohydrate Polymers*, 102, 136-143. <http://dx.doi.org/10.1016/j.carbpol.2013.11.021>. PMID:24507265.
 12. Reddy, N., & Yang, Y. (2009). Extraction and characterization of natural cellulose fibers from common milkweed stems. *Polymer Engineering and Science*, 49(11), 2212-2217. <http://dx.doi.org/10.1002/pen.21469>.
 13. Reddy, N., & Yang, Y. (2009). Properties of natural cellulose fibers from hop stems. *Carbohydrate Polymers*, 77(4), 898-902. <http://dx.doi.org/10.1016/j.carbpol.2009.03.013>.
 14. Johar, N., Ahmad, I., & Dufresne, A. (2012). Extraction, preparation and characterization of cellulose fibres and nanocrystals from rice husk. *Industrial Crops and Products*, 37(1), 93-99. <http://dx.doi.org/10.1016/j.indcrop.2011.12.016>.
 15. Indran, S., Edwin Raj, R., & Sreenivasan, V. S. (2014). Characterization of new natural cellulosic fiber from *Cissus quadrangularis* root. *Carbohydrate Polymers*, 110, 423-429. <http://dx.doi.org/10.1016/j.carbpol.2014.04.051>. PMID:24906775.
 16. Kacem, I., Majdoub, H., & Roudesli, S. (2008). Physicochemical properties of pectin from *retama raetam* obtained using sequential extraction. *Journal of Applied Sciences*, 8(9), 1713-1719. <http://dx.doi.org/10.3923/jas.2008.1713.1719>.
 17. Bokhari-Taieb Brahimi, H., Faugeron, C., Hachem, K., Kaid-Harche, M., & Gloaguen, V. (2015). Investigation of parietal polysaccharides from *Retama raetam* roots. *African Journal of Biotechnology*, 14(29), 2327-2334. <http://dx.doi.org/10.5897/AJB2015.14754>.
 18. Mechergui, K., Mahmoudi, H., Khouja, M. L., & Jaouadi, W. (2017). Factors influencing seed germination of the pastoral plant *Retama raetam* subsp. *bovei* (Fabaceae): interactive effects of fruit morphology, salinity, and osmotic stress. *Biologija*, 63(2), 134-151. <http://dx.doi.org/10.6001/biologija.v63i2.3525>.
 19. Segal, L., Creely, J., Martin, A. Jr, & Conrad, C. (1959). An empirical method for estimating the degree of crystallinity of native cellulose using the X-ray diffractometer. *Textile Research Journal*, 29(10), 786-794. <http://dx.doi.org/10.1177/004051755902901003>.
 20. Kale, R. D., Bansal, P. S., & Gorade, V. G. (2018). Extraction of microcrystalline cellulose from cotton sliver and its comparison with commercial microcrystalline cellulose. *Journal of Polymers and the Environment*, 26(1), 355-364. <http://dx.doi.org/10.1007/s10924-017-0936-2>.
 21. Sun, X.-F., Sun, R.-C., Su, Y., & Sun, J.-X. (2004). Comparative study of crude and purified cellulose from wheat straw. *Journal of Agricultural and Food Chemistry*, 52(4), 839-847. <http://dx.doi.org/10.1021/jf0349230>. PMID:14969539.
 22. Uma Maheswari, C., Obi Reddy, K., Muzenda, E., Guduri, B. R., & Varada Rajulu, A. (2012). Extraction and characterization of cellulose microfibrils from agricultural residue – *Cocos nucifera* L. *Biomass and Bioenergy*, 46, 555-563. <http://dx.doi.org/10.1016/j.biombioe.2012.06.039>.
 23. Jonjankiat, S., Wittaya, T., & Sridach, W. (2011). Improvement of poly (vinyl alcohol) adhesives with cellulose microfibre from sugarcane bagasse. *Iranian Polymer Journal*, 20(4), 305-317.
 24. Reddy, K. O., Zhang, J., Zhang, J., & Rajulu, A. V. (2014). Preparation and properties of self-reinforced cellulose composite films from Agave microfibrils using an ionic liquid. *Carbohydrate Polymers*, 114, 537-545. <http://dx.doi.org/10.1016/j.carbpol.2014.08.054>. PMID:25263924.
 25. Alemdar, A., & Sain, M. (2008). Isolation and characterization of nanofibers from agricultural residues–Wheat straw and soy hulls. *Bioresource Technology*, 99(6), 1664-1671. <http://dx.doi.org/10.1016/j.biortech.2007.04.029>. PMID:17566731.
 26. Morán, J. I., Alvarez, V. A., Cyras, V. P., & Vázquez, A. (2008). Extraction of cellulose and preparation of nanocellulose from sisal fibers. *Cellulose*, 15(1), 149-159. <http://dx.doi.org/10.1007/s10570-007-9145-9>.
 27. Sonia, A., & Priya Dasan, K. (2013). Chemical, morphology and thermal evaluation of cellulose microfibrils obtained from *Hibiscus sabdariffa*. *Carbohydrate Polymers*, 92(1), 668-674. <http://dx.doi.org/10.1016/j.carbpol.2012.09.015>. PMID:23218352.
 28. Reddy, K. O., Maheswari, C. U., Dhlamini, M. S., & Kommula, V. P. (2016). Exploration on the characteristics of cellulose microfibrils from Palmyra palm fruits. *International Journal of Polymer Analysis and Characterization*, 21(4), 286-295. <http://dx.doi.org/10.1080/1023666X.2016.1147799>.
 29. Reddy, K. O., Maheswari, C. U., Dhlamini, M. S., Mothudi, B. M., Kommula, V. P., Zhang, J., Zhang, J., & Rajulu, A. V. (2018). Extraction and characterization of cellulose single fibers from native african napier grass. *Carbohydrate Polymers*, 188, 85-91. <http://dx.doi.org/10.1016/j.carbpol.2018.01.110>. PMID:29525176.
 30. Fan, M., Dai, D., & Huang, B. (2012). *Fourier transform infrared spectroscopy for natural fibres*. In S. M. Salih (Ed.), *Fourier transform-materials analysis* (pp. 45-68). Rijeka: InTech. <http://dx.doi.org/10.5772/35482>.
 31. Maryana, R., Ma'rifatun, D., Wheni, A., Satriyo, K., & Rizal, W. A. (2014). Alkaline pretreatment on sugarcane bagasse for bioethanol production. *Energy Procedia*, 47, 250-254. <http://dx.doi.org/10.1016/j.egypro.2014.01.221>.
 32. Oh, S. Y., Yoo, D. I., Shin, Y., Kim, H. C., Kim, H. Y., Chung, Y. S., Park, W. H., & Youk, J. H. (2005). Crystalline structure analysis of cellulose treated with sodium hydroxide and carbon dioxide by means of X-ray diffraction and FTIR spectroscopy. *Carbohydrate Research*, 340(15), 2376-2391. <http://dx.doi.org/10.1016/j.carres.2005.08.007>. PMID:16153620.
 33. Sun, J. X., Sun, X. F., Zhao, H., & Sun, R. C. (2004). Isolation and characterization of cellulose from sugarcane bagasse. *Polymer Degradation & Stability*, 84(2), 331-339. <http://dx.doi.org/10.1016/j.polymdegradstab.2004.02.008>.

34. Gao, X., Chen, K.-L., Zhang, H., Peng, L.-C., & Liu, Q.-X. (2014). Isolation and characterization of cellulose obtained from bagasse pith by oxygen-containing agents. *BioResources*, 9(3), 4094-4107. <http://dx.doi.org/10.15376/biores.9.3.4094-4107>.
35. Sain, M., & Panthapulakkal, S. (2006). Bioprocess preparation of wheat straw fibers and their characterization. *Industrial Crops and Products*, 23(1), 1-8. <http://dx.doi.org/10.1016/j.indcrop.2005.01.006>.
36. Kondo, T., & Sawatari, C. (1996). A Fourier transform infra-red spectroscopic analysis of the character of hydrogen bonds in amorphous cellulose. *Polymer*, 37(3), 393-399. [http://dx.doi.org/10.1016/0032-3861\(96\)82908-9](http://dx.doi.org/10.1016/0032-3861(96)82908-9).
37. Kondo, T. (1997). The assignment of IR absorption bands due to free hydroxyl groups in cellulose. *Cellulose*, 4(4), 281-292. <http://dx.doi.org/10.1023/A:1018448109214>.
38. Flauzino, W. P., No., Silvério, H. A., Dantas, N. O., & Pasquini, D. (2013). Extraction and characterization of cellulose nanocrystals from agro-industrial residue-soy hulls. *Industrial Crops and Products*, 42, 480-488. <http://dx.doi.org/10.1016/j.indcrop.2012.06.041>.
39. French, A. D. (2014). Idealized powder diffraction patterns for cellulose polymorphs. *Cellulose*, 21(2), 885-896. <http://dx.doi.org/10.1007/s10570-013-0030-4>.
40. Park, S., Baker, J. O., Himmel, M. E., Parilla, P. A., & Johnson, D. K. (2010). Cellulose crystallinity index: measurement techniques and their impact on interpreting cellulase performance. *Biotechnology for Biofuels*, 3(1), 10. <http://dx.doi.org/10.1186/1754-6834-3-10>. PMID:20497524.
41. Wang, Y., Zhao, Y., & Deng, Y. (2008). Effect of enzymatic treatment on cotton fiber dissolution in NaOH/urea solution at cold temperature. *Carbohydrate Polymers*, 72(1), 178-184. <http://dx.doi.org/10.1016/j.carbpol.2007.08.003>.
42. Rhim, J.-W., Reddy, J. P., & Luo, X. (2015). Isolation of cellulose nanocrystals from onion skin and their utilization for the preparation of agar-based bio-nanocomposites films. *Cellulose*, 22(1), 407-420. <http://dx.doi.org/10.1007/s10570-014-0517-7>.
43. Abe, K., & Yano, H. (2009). Comparison of the characteristics of cellulose microfibril aggregates of wood, rice straw and potato tuber. *Cellulose*, 16(6), 1017-1023. <http://dx.doi.org/10.1007/s10570-009-9334-9>.
44. Chatterjee, A., Kiran Kumar, G., Dharma Sagar, B., Sravanti, K., Ramakrishna, K., & Rajesh, C. (2018). Pure and copper doped cellulose microfibers-a case study. *Materials Research Express*, 5(10), 105302. <http://dx.doi.org/10.1088/2053-1591/aad9d4>.
45. Puttaswamy, M., Srinikethan, G., & Shetty, K. V. (2017). Biocomposite composed of PVA reinforced with cellulose microfibers isolated from biofuel industrial dissipate: *Jatropha Curcus L.* seed shell. *Journal of Environmental Chemical Engineering*, 5(2), 1990-1997. <http://dx.doi.org/10.1016/j.jece.2017.04.004>.
46. C S, J. C., George, N., & Narayanankutty, S. K. (2016). Isolation and characterization of cellulose nanofibrils from arecanut husk fibre. *Carbohydrate Polymers*, 142, 158-166. <http://dx.doi.org/10.1016/j.carbpol.2016.01.015>. PMID:26917386.
47. Kasiri, N., & Fathi, M. (2018). Production of cellulose nanocrystals from pistachio shells and their application for stabilizing Pickering emulsions. *International Journal of Biological Macromolecules*, 106, 1023-1031. <http://dx.doi.org/10.1016/j.ijbiomac.2017.08.112>. PMID:28842201.
48. Nabili, A., Fattoum, A., Brochier-Salon, M.-C., Bras, J., & Elaloui, E. (2017). Synthesis of cellulose triacetate-I from microfibrillated date seeds cellulose (*Phoenix dactylifera L.*). *Iranian Polymer Journal*, 26(2), 137-147. <http://dx.doi.org/10.1007/s13726-017-0505-5>.
49. Chen, W., Yu, H., Liu, Y., Hai, Y., Zhang, M., & Chen, P. (2011). Isolation and characterization of cellulose nanofibers from four plant cellulose fibers using a chemical-ultrasonic process. *Cellulose*, 18(2), 433-442. <http://dx.doi.org/10.1007/s10570-011-9497-z>.
50. Adel, A. M., Abd El-Wahab, Z. H., Ibrahim, A. A., & Al-Shemy, M. T. (2011). Characterization of microcrystalline cellulose prepared from lignocellulosic materials. Part II: physicochemical properties. *Carbohydrate Polymers*, 83(2), 676-687. <http://dx.doi.org/10.1016/j.carbpol.2010.08.039>.
51. Reddy, J. P., & Rhim, J.-W. (2018). Extraction and characterization of cellulose microfibers from agricultural wastes of onion and garlic. *Journal of Natural Fibers*, 15(4), 465-473. <http://dx.doi.org/10.1080/15440478.2014.945227>.
52. Das, K., Ray, D., Bandyopadhyay, N. R., & Sengupta, S. (2010). Study of the properties of microcrystalline cellulose particles from different renewable resources by XRD, FTIR, nanoindentation, TGA and SEM. *Journal of Polymers and the Environment*, 18(3), 355-363. <http://dx.doi.org/10.1007/s10924-010-0167-2>.
53. Azubuike, C. P., & Okhamafe, A. O. (2012). Physicochemical, spectroscopic and thermal properties of microcrystalline cellulose derived from corn cobs. *International Journal of Recycling of Organic Waste in Agriculture*, 1(1), 9. <http://dx.doi.org/10.1186/2251-7715-1-9>.
54. Das, K., Ray, D., Bandyopadhyay, N. R., Ghosh, T., Mohanty, A. K., & Misra, M. (2009). A study of the mechanical, thermal and morphological properties of microcrystalline cellulose particles prepared from cotton slivers using different acid concentrations. *Cellulose*, 16(5), 783-793. <http://dx.doi.org/10.1007/s10570-009-9280-6>.

Received: Aug. 03, 2018

Revised: Sept. 21, 2018

Accepted: Oct. 23, 2018